Title
Light Absorbers and Catalysts for Solar to Fuel Conversion

Author
Kornienko, Nikolay

Publication Date
2016

Peer reviewed|Thesis/dissertation

Light Absorbers and Catalysts for Solar to Fuel Conversion

By

Nikolay I Kornienko

A dissertation submitted in satisfaction of the requirements for the degree of

Doctor of Philosophy

In

Chemistry

in the

Graduate Division

of the

University of California, Berkeley

Committee in charge:

Professor Peidong Yang, Chair

Professor Gabor Somorjai

Professor Junqiao Wu

Professor Tanja Cuk

Spring 2016

Abstract

Light Absorbers and Electrocatalysts for Solar to Fuel Conversion

by

Nikolay I Kornienko

Doctor of Philosophy in Chemistry

University of California, Berkeley

Professor Peidong Yang, Chair

Increasing fossil fuel consumption and the resulting consequences to the environment has propelled research into means of utilizing alternative, clean energy sources. Solar power is among the most promising of renewable energy sources but must be converted into an energy dense medium such as chemical bonds to render it useful for transport and energy storage. Photoelectrochemistry (PEC), the splitting of water into oxygen and hydrogen fuel or reducing CO_2 to hydrocarbon fuels *via* sunlight is a promising approach towards this goal.

Photoelectrochemical systems are comprised of several components, including light absorbers and catalysts. These parts must all synergistically function in a working device. Therefore, the continual development of each component is crucial for the overall goal. For PEC systems to be practical for large scale use, the must be efficient, stable, and composed of cost effective components. To this end, my work focused on the development of light absorbing and catalyst components of PEC solar to fuel converting systems.

In the direction of light absorbers, I focused of utilizing Indium Phosphide (InP) nanowires (NWs) as photocathodes. I first developed synthetic techniques for InP NW solution phase and vapor phase growth. Next, I developed light absorbing photocathodes from my InP NWs towards PEC water splitting cells.

I studied cobalt sulfide (CoSx) as an earth abundant catalyst for the reductive hydrogen evolution half reaction. Using *in situ* spectroscopic techniques, I elucidated the active structure of this catalyst and offered clues to its high activity.

In addition to hydrogen evolution catalysts, I established a new generation of earth abundant catalysts for CO_2 reduction to CO fuel/chemical feedstock. I first worked with molecularly tunable homogeneous catalysts that exhibited high selectivity for CO_2 reduction in non-aqueous media. Next, in order to retain molecular tunability while achieving stability and efficiency in aqueous solvents, I aimed to heterogenize a class of molecular porphyrin catalysts into a 3D mesoscopic porous catalytic structure in the form of a metal-organic framework (MOF).To do so, I initially developed a growth for thin film MOFs that were embedded with catalytic groups in their linkers.[6] Next, I utilized these thin film MOFs grown on conductive substrates and functionalized with cobalt porphyrin units as 3D porous CO_2 reduction catalysts. This new class of catalyst exhibited high efficiency, selectivity, and stability in neutral pH aqueous electrolytes.

Finally, as a last chapter of my work, I explored hybrid inorganic/biological CO_2 reduction pathways. Specifically, I used time-resolved spectroscopic and biochemical techniques to investigate charge transfer pathways from light absorber to CO_2-derived acetate in acetogenic self-sensitized bacteria.

Table of Contents:

* Denotes equal contribution

Δ Publication central to dissertation

[1] "2-D Array Photonic Crystal Sensing Motif", J. Zhang, L. Wang, J. Luo, A. Tikhonov, **N. Kornienko**, and S.A. Asher, *J. Am. Chem. Soc.*, 133, 9152 (2011).

[2] "Reflectivity Enhanced Two-Dimensional Dielectric Particle Array Monolayer Diffraction", A. Tikhonov, **N. Kornienko**, J. Zhang, L. Wang and S.A. Asher, *J. Nanophoton.*, 6, 063509 (2012).

Δ [3]"Visible Photoredox Catalysis: Selective Reduction of Carbon Dioxide to Carbon Monoxide by a Nickel N-Heterocyclic Carbene Isoquinoline Complex", V Thoi*, **N. Kornienko***, C Margarit, P. Yang and C. Chang, *J. Am. Chem. Soc.*, 135, 14413 (2013).

Δ [4] "Mesoscopic Constructs of Ordered and Oriented Metal-Organic Frameworks on Plasmonic Silver Nanocrystals" Y. Zhao*, **N. Kornienko***, Z. Liu,C. Zhu, S. Asahina, T. Kuo, W. Bao, C. Xie, O. Terasaki, P. Yang, O. Yaghi, *J. Am. Chem. Soc.*, 137, 2199, 2015

Δ [5] "Solution Phase Synthesis of Indium Gallium Phosphide Alloy Nanowires" **N. Kornienko**, D. Whitmore, Y. Yu, S. Leone and P. Yang, *ACS Nano*, 9, 3951 (2015)

Δ [6] "Operando Spectroscopic Analysis of an Amorphous Cobalt Sulfide Electrocatalyst" **N. Kornienko**, J. Resasco, N. Becknell, C. Jiang, Y. Liu, K. Nie, X. Sun, J. Guo, S. Leone, P. Yang, *J. Am. Chem. Soc.*, 137, 7448 (2015)

[7] "Covalent Organic Frameworks Comprising Cobalt Porphyrins for Catalytic CO_2 Reduction in Water" S. Lin*, C. Dierks*, Y. Zhang*, **N. Kornienko**, E. Nichols, Y. Zhao, A. Paris, D. Kim, P. Yang, O. Yaghi, C. Chang, *Science*, 349, 1208 (2015)

Δ [8] "Metal-Organic Frameworks for Electrocatalytic Reduction of Carbon Dioxide" **N. Kornienko***, Y. Zhao*, C. Kley, C. Zhu, D. Kim, S. Lin, C. Chang, O. Yaghi, P. Yang, *J. Am. Chem. Soc.*, 137, 14129 (2015)

[9] “Atomically Thin Two-Dimensional Organic-Inorganic Hybrid Perovskites” L. Duo, A. Wong, Y. Yu, M. Lai, **N. Kornienko**, S. Eaton, A. Fu, C. Bishak, J. Ma, T. Ding, N. Ginsberg, L. Wang, A. Alivisatos, P. Yang, *Science,* 349, 6255 (2015)

[10] “Atomic Level Structure of P_3Ni Nanoframe Electrocatalysts by In-Situ X-Ray Absorption Spectroscopy” N. Becknell, Y. Kang, C. Chen, J. Resasco, **N. Kornienko**, J. Guo, N. Markovic, G. Somorjai, V. Stamenkovic, P. Yang, *J. Am. Chem. Soc.* 37, 15817 (2015)

[11] “Low-Temperature Solution-Phase Growth of Silicon and Silicon Containing Alloys” J. Sun, F. Cui, C. Kiseilowski, Y. Yu, **N. Kornienko**, P. Yang, *J. Phys. Chem. C. In Press - Online DOI:* 10.1021/acs.jpcc.5b08289

[12] “TiO_2/$BiVO_4$ Nanowire Heterostructure Photoanodes Based on Type II Band Allignment” J. Resasco, H. Zhang, **N. Kornienko**, N. Becknell, H. Lee, A. Briseno, J. Guo, P. Yang *ACS Central Science*, 2, 80 (2016)

[13] “Single Nanowire Photoelectrochemistry” Y. Su*, C. Liu*, S. Brittman, J. Tang, A. Fu, **N. Kornienko**, Q. Kong, P. Yang *Nat. Nanotechnol. In Press*

[14] “Growth and Photoelectrochemical Energy Conversion of Wurtzite Indium Phosphide Nanowire Arrays” **N. Kornienko**, N. Gibson, H. Zhang, S. Eaton, Y. Yu, S. Aloni, P. Yang *ACS Nano, In Press*

[15] “Anisotropic Phase Segregation and Migration of Pt in Nanocrystals En Route to Nanoframe Catalysts” Z. Niu, B. Becknell, Y. Yu, D. Kim, C. Chen, **N. Kornienko**, G. Somorjai, P. Yang, *Nat. Mater. Accepted*

[16] “Synthesis and Composition Tunable Cesium Lead Halide Nanowires through Anion-Exchange Reactions” D. Zhang, Y. Yang, Y. Bekenstein, Y. Yu, N. Gibson, A. Wong, S. Eaton, **N. Kornienko**, Q. Kong, M. Lai, Y. Bekenstein, A. P. Alivisatos, S. R. Leone, P. Yang, *Submitted*

[17] “Atomic Resolution Imaging of Halide Perovskites” Y. Yu, D. Zhang, C. Kisielowski, L. Dou, **N. Kornienko**, Y. Bekenstein, A. P. Alivisatos, P. Yang, *In Preparation*

[Δ] [18] “Spectroscopic Elucidation of Picosecond Energy Transfer Pathways in Hybrid Inorganic-Biological Organisms for Solar-to-Chemical Production ” **N. Kornienko***, K. Sakimoto*, D. Herlihy, S. Nguyen, A. P. Alivisatos, C. B. Harris, A. Schwartzberg, P. Yang *In Preparation*

2. Introduction

In the last few decades, a growing population combined with an increase in per capita energy consumption has begun to deplete the finite fossil fuel sources currently used for power generation[1]. The rapid depletion of fossil fuels and inherent harmful environmental effects resulting from their usage is the impetus behind many recent efforts to develop alternative ways to supply energy for mankind. Deemed the terawatt challenge, the search for alternative, environmentally friendly technologies for solar energy conversion to provide the 20 terawatts needed to sustain society's current usage is of highest urgency and one of the main challenges that society is currently facing[2,3].

In contrast to fossil fuels such as coal and oil, alternative sustainable sources such as wind, hydroelectric and solar power provide clean energy without the risk of depletion. In particular, sunlight is among the most promising and abundant of these alternative energy sources - the total amount of sunlight falling on earth's surface, integrated over a year, equates to 23,000 terawatts[4]. Efficiently harvesting a fraction of this total energy would be more than enough to sustainably supply our growing society. Having realized this, significant research and development has been applied to this area. Despite many decades' worth of work and significant progress being made in solar energy conversion, the fraction of society's energy that results from the sun currently amounts to less than 1%. Increasing this fraction will require collaborative efforts in the areas of policy, engineering, and fundamental scientific research. Regarding the area of science and engineering, improvements in cost and efficiency are essential to make solar energy a truly viable alternative to fossil fuels.

Currently, photovoltaic (PV) cells are the main form of solar energy conversion, in which electric power is generated upon the solar illumination of a semiconductor or organic light absorbing material. While this is the currently most developed method to harness the sun's power, it has several drawbacks that render it incapable of being the sole source of solar power generation. These drawbacks include the fact that electric power can only be generated when a photovoltaic cell is under illumination and that society's peak energy demand is in the evening hours, when no sunlight is available. Hence, developing methods for solar energy harnessing and storage is of paramount importance and an energy storage media in the form of fuels highly desirable to be readily integrated into current infrastructures.

As complimentary approach to photovoltaics, photoelectrochemistry (PEC) employs solar energy to drive chemical reactions for storing this energy in the form of chemical bonds[5]. Inspired by natural photosynthesis, in which plants use sunlight to convert carbon dioxide into sugars, PEC cells convert water or carbon dioxide into hydrogen or hydrocarbon fuels as an energy dense storage media. This process accomplishes both solar energy absorption and conversion in a single step. The resulting products can be directly used as nighttime energy sources, transportation fuels, or as chemical feedstocks that are compatible with existing infrastructures. Illustrated in figure 2.1, large scale implementation of PEC energy conversion can help create a closed carbon cycle, in which CO_2 emissions from vehicles and factories are converted back into hydrocarbon fuels. To carry out these reactions, the semiconductor light absorbers must generate sufficient voltage to efficiently drive the process as well as possess the proper band alignments to make the reaction thermodynamically feasible. Furthermore, for this process to be practical on a large scale, the materials must be earth abundant, have a catalytic

turnover frequency (TOF) matching the incident solar photon flux and be stable in their operating reaction media.

The splitting of water into hydrogen and oxygen was first studied as a model system to understand this process because of the simplicity of the reaction. The mechanism for both of the half reactions of hydrogen evolution and oxygen evolution is now well understood and solar to hydrogen efficiencies are steadily increasing.[6-9]. However, challenges of stability and cost efficiency still need to be overcome and efficiencies need to be further improved. While hydrogen is useful as a transportation fuel and chemical feedstock, additional desirable hydrocarbon fuels such as methanol can be generated from the reduction of carbon dioxide. Liquid hydrocarbons can be readily integrated into the current infrastructure and do not possess the additional inherent challenge of gaseous storage. Carbon dioxide reduction, however, implicates additional challenges that must be addressed in order to achieve similar efficiencies as water splitting[10]. These challenges include the limited solubility of carbon dioxide in water, lack of catalytic selectivity for a single reaction product, and the need for a high energy input to drive the kinetically slower, multi-electron process. Moreover, carbon dioxide is a highly inert molecule and the formation of multiple bonds to create complex molecules generally necessitates much more energy than is thermodynamically required[11]. Ideally, CO_2 reduction runs at room temperature and atmospheric pressure employing visible solar light.

In the subsequent sections, I will illustrate my efforts towards the development of functional PEC systems. Such systems can be viewed as modular, multi-component devices, where each component can be improvised and re-integrated into a fully functional device. Within this context, my work has focused on next-generation light absorber and catalyst design, synthesis, investigation and utilization.

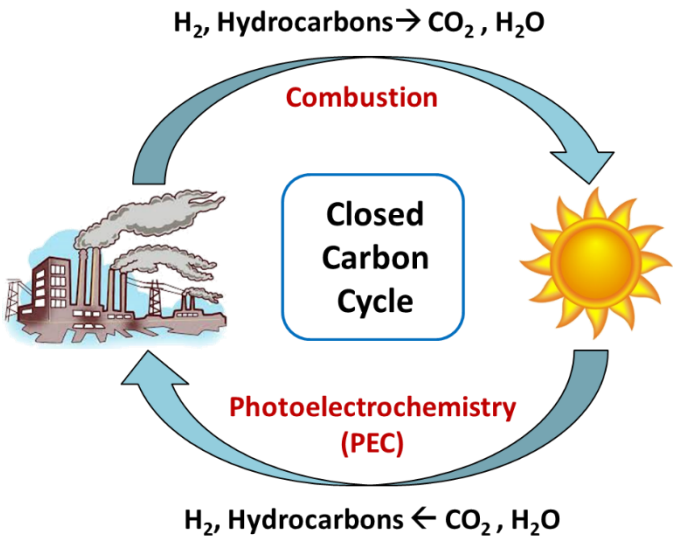

Figure 2.1. Photoelectrochemistry is a promising solution to generate fuels from renewable energy.

3. InGaP Nanowire Solution Phase Synthesis and Photocathode Development

3.0 Preface

In this section, we focused on developing a solution phase growth for 1-dimensional nanostructures with the eventual goal being their implementation into scalable and low cost photocathodes. We chose III-V materials such as InP, InGaP, and GaP because they had appropriate band alignment and band gap energies to potentially be highly functional yet cost effective alternatives to single crystal wafers.

3.1 Introduction

III-V semiconductors are well suited for a number of optoelectronic applications because of their typically high carrier mobilities and direct band gaps.[12] Among them, pseudo-binary alloys of III-V's feature structural and electronic properties such as band gap, index of refraction and lattice constant that can be directly modified through the tuning of their composition.[13,14] Due to this unique control, III-V alloys find special uses in biomedical imaging,[15] light emitting diodes,[16] lasers,[17] heterojunction bipolar transistors[18] and high performance multi-junction photovoltaic cells.[19]

Indium gallium phosphide ($In_xGa_{1-x}P$) is a pseudo-binary III-V alloy of an indirect band gap semiconductor, gallium phosphide (GaP), and a direct band gap semiconductor, indium phosphide (InP). This alloy possesses a tunable band gap that ranges from 1.35 to 2.26 electron volts (eV), which is direct for the composition range of $1 \geq x \geq 0.2\text{-}0.3$.[20-22] The band gap range of 1.35-2.26 eV is particularly attractive for use in solar energy conversion and lighting applications because this range encompasses the majority of the visible light spectrum.[9] The ability to synthesize $In_xGa_{1-x}P$ in the nanowire (NW) morphology with tunable structural and electronic properties can pave a route towards potential applications in miniaturized optoelectronic devices, tunable NW lasers, and high surface area photocatalysts. However, there are several drawbacks that impede large-scale implementation of this material: bulk $In_xGa_{1-x}P$, thin films, or nanostructures are typically synthesized through liquid phase epitaxy (LPE), metal-organic chemical vapor deposition (MOCVD) or molecular beam epitaxy (MBE) techniques, which are coupled with several inherent limitations, including low material yield and expensive growth processes.[23] Furthermore, a common requirement for lattice matched substrates such as Gallium Arsenide (GaAs) or Germanium (Ge) limits the composition range of the resulting materials to compositions that can grow epitaxially on these substrates.

In this work, we present a scalable, low temperature solution phase synthesis for $In_xGa_{1-x}P$ NWs with full compositional, and therefore, structural and electronic tunability. In the recent literature, InP and GaP NWs were synthesized in the solution phase through a variety of techniques, including electrodeposition,[24] synthesis in aqueous solvents,[25] supercritical fluids,[26] and organic solvents.[27-34] Moreover, $Al_xGa_{1-x}As$ alloy NWs[35] and various II-VI NW alloys and heterostructures[36-38] have also been synthesized in the solution phase. $In_xGa_{1-x}P$ quantum dots have been synthesized through the thermal decomposition of precursors in an organic solvent.[39] $In_xGa_{1-x}P$ NWs, however, have only been synthesized through vapor phase CVD and MBE methods.[40-44] In light of the previous synthesis and applications of GaP, InP and $In_xGa_{1-x}P$ NWs, we aimed at developing a solution phase synthesis of $In_xGa_{1-x}P$ NWs featuring (I) composition control, (II) low temperature growth, (III) scalability, and (IV) no requirement for lattice

matched substrates. In the following sections, we show that a pre-seeded solution-liquid-solid (SLS) synthesis can be used to controllably grow $In_xGa_{1-x}P$ NWs across the entire composition range of x=0 to x=1. Through systematic structural and optical measurements, we demonstrate structural and electronic tunability of $In_xGa_{1-x}P$ NWs and provide insight into both the disordered alloy crystal structure and the direct to indirect band gap transition. InP NWs are next chosen to as a photocathode materials and utilized in solar to fuel hydrogen generation.

3.2 Results and Discussion

We synthesized $In_xGa_{1-x}P$ NWs with a one pot, self-seeded SLS synthesis (Figure 3.1A) in a nitrogen environment using standard schlenk line techniques. In this process, a liquid metal seed in solution serves as both the growth catalyst and group III precursor source. Trimethylindium (TMIn) and triethylgallium (TEGa) precursors were injected into a room-temperature, non-coordinating squalane solvent and the solution was stirred until homogeneous. Next, the reaction mixture was lowered into a 280^0C molten salt bath and heated for 60 minutes to fully decompose the metal precursors and generate homogeneous indium-gallium alloy growth seeds. The In/Ga seed solution was next removed from the molten salt and allowed to cool to room temperature. After cooling, tris(trimethylsilyl)phosphine (TMSP) phosphorus precursor was then injected into the reactor, which was subsequently lowered into the same 280°C molten salt bath and heated for an additional 60 minutes. The solution changed color from grey to black upon the growth of the $In_xGa_{1-x}P$ NWs. After thorough cleaning of the NWs through multiple centrifugation steps, a hydrochloric acid etch removed the metal seeds. Because TMIn and TEGa decompose at different rates under our reaction conditions, forming the In/Ga growth seeds in a separate step was necessary to obtain homogeneous $In_xGa_{1-x}P$ NWs. A mixture of separate InP and GaP NWs instead of alloys resulted when TMIn, TEGa, and TMSP precursors were mixed and heated in a single step.

Following the synthesis, we characterized the morphology and composition of the NWs with electron microscopy. The size and shape of the synthesized NWs was first studied with scanning electron microscopy (SEM). Figure 3.1B shows a typical SEM image of $In_xGa_{1-x}P$ NWs with a composition of x=0.50. Transmission electron microscopy (TEM) in figure 3.1C-H offers a closer look at the NWs and illustrates the morphology of several batches of NWs with different compositions. The diameters of the NWs typically varied between 70 nm and 150 nm and their lengths between 1000 nm and 2500 nm. The composition of the NWs was controlled by the TMIn:TEGa ratio of the precursor and the diameter of the NWs was controlled by the precursor concentration.

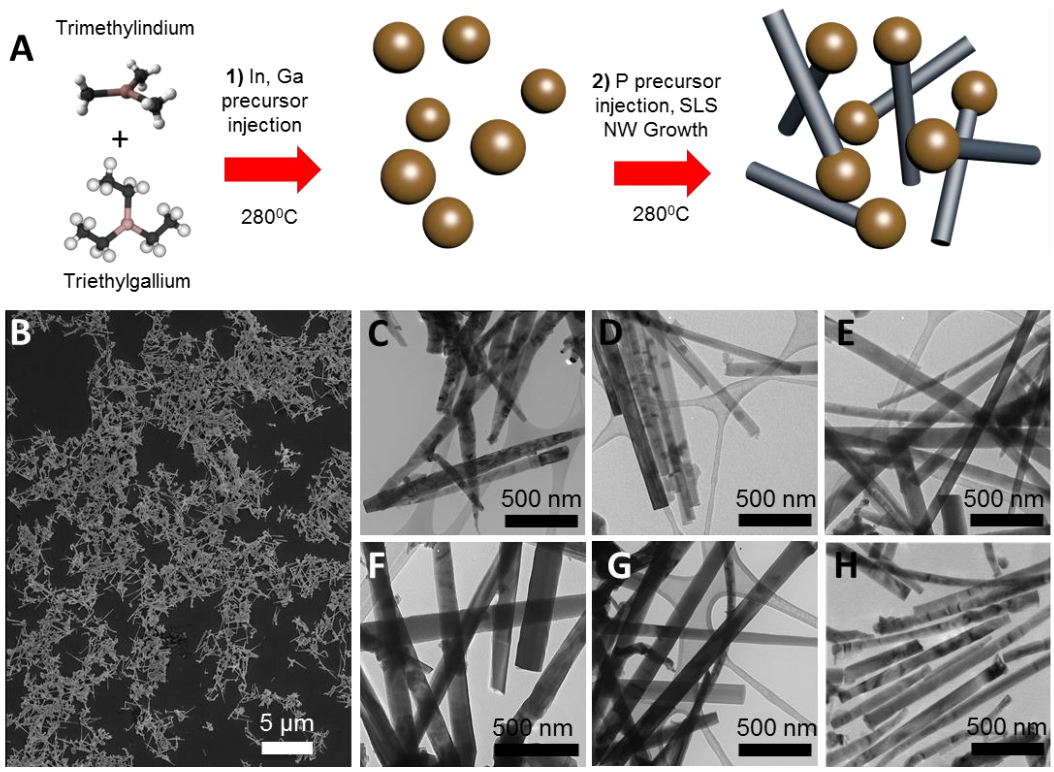

Figure 3.1. Synthetic scheme (A) of the $In_xGa_{1-x}P$ nanowire growth. SEM (B) of $In_xGa_{1-x}P$ NWs with x=0.50 drop cast on a silicon substrate. TEM images of NWs (C-H) with composition x=0, 0.21, 0.41, 0.66, 0.84, and 1.0, respectively.

To assess the chemical composition and element distribution of the resulting NWs, scanning transmission electron microscopy energy dispersive X-ray spectroscopy (STEM-EDS) analysis was utilized. Figure 3.2A shows a typical EDS spectrum taken from $In_xGa_{1-x}P$ NWs, with x=0.21, with Ga, In, and P peaks labeled, indicating the presence of both In and Ga in the NWs, with EDS mapping in the inset illustrating the corresponding elements distributed throughout the NWs. EDS mapping of an individual wire and growth seed (Figure 3.2B), reveals that the $In_xGa_{1-x}P$ NW was more Ga-rich than the growth seed, which was observed for every batch of alloy NWs. The tendency of $In_xGa_{1-x}P$ to grow as a more Ga rich composition relative to the starting material is commonly observed and is explained by a lower formation enthalpy for the GaP relative to InP.[45-48] However, the NW body was uniform in composition: the lack of abrupt compositional variation is first evidenced in a lack of contrast in Z-contrast high angle annular dark field scanning transmission electron microscopy (HAADF-STEM) in Figure 3.2C and D. Furthermore, a typical elemental line scan (Figure 3.2E) indicates that the composition of the NW generally remains uniform along the growth direction. However, with the techniques used, we cannot rule out fluctuations in composition of several nanometers or less.

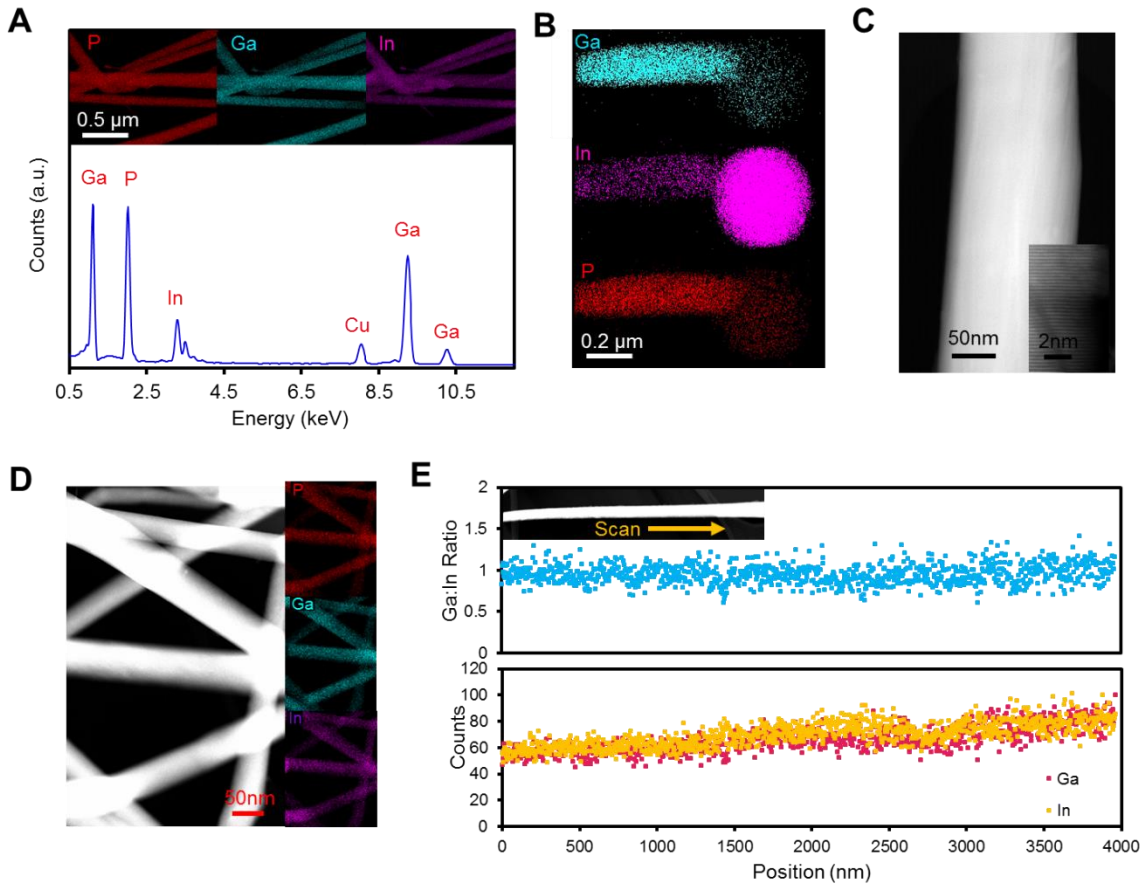

Figure 3.2. Electron microscopy analysis of $In_xGa_{1-x}P$ NWs. A typical EDS spectrum (A) featuring prominent In, Ga, and P peaks and their corresponding elemental maps in the inset. EDS map of a NW and growth seed (B) reveals an In rich seed relative to the NW composition. Z-contrast HAADF-STEM of $In_xGa_{1-x}P$ NWs (C, D) with x=0.66 and x=.50 features no abrupt contrast changes that would be indicative of sharp compositional fluctuations. A line scan along the length of the NW (E) shows no significant variations in the In/Ga elemental ratio though the possibility compositional fluctuations of a few nanometers cannot be excluded.

We proceeded to study the structural properties, including crystal phase, growth direction, and presence or lack of long range ordering of the $In_xGa_{1-x}P$ through both microscopic and macroscopic methods. X-ray diffraction measurements were first taken to determine the crystal structure of the NWs, and indicate that the $In_xGa_{1-x}P$ NWs consist of a single phase Zincblende structure across the entire composition range. There are several reports of Wurtzite InP[49,50] and GaP[51] NWs grown in the vapor phase at high temperatures and large V/III precursor ratios. The formation of the Wurtzite phase in these situations is believed to occur either in a regime of high growth temperature and precursor supersaturation in the catalyst where nucleation of the Wurtzite phase is thermodynamically preferred or for very thin NWs (with diameters typically less than 20 nm) where the relatively lower surface energy of Wurtzite stabilizes this crystal phase.[52-54] However, our solution phase synthesis meets neither of these conditions and only the Zincblende phase is observed.

The lattice constant expansion of the $In_xGa_{1-x}P$ NWs from 5.45 Å to 5.88 Å with increasing indium composition, x, is measured at an ensemble level through shifting of the (111) peak to lower 2θ values, indicating larger distances between the corresponding crystal planes (Figure 3.3A). The full width half max (FWHM) of the (111) diffraction peak, determined by instrument resolution, particle size, and crystal structure homogeneity, varies from 0.47 deg. for InP and 0.58 deg. for GaP up to a maximum 0.72 deg. for $In_xGa_{1-x}P$ with x=0.66. Considering that the size of our NWs is similar across the composition range and too large to significantly broaden the XRD peaks, our data is indicative of minor lattice constant fluctuations and a disordered crystal lattice in the $In_xGa_{1-x}P$ NWs. Asymmetries in the diffraction peaks may be due to the presence of dislocations, lattice strain, or fluctuations in composition within individual nanowires or within the batch.[43,55] The lattice constant of the NWs determined from the XRD measurements shifts linearly with NW composition in accordance with Vegard's law (Figure 3.3B), which predicts such a linear relation in an ensemble measurement of a random mixture where small structural fluctuations are averaged out.[56] The lack of significant deviations from Vegard's law or multiple (111) peaks in the XRD spectra indicates the absence of significant phase segregation in the $In_xGa_{1-x}P$ NWs.

Macroscopic XRD structural measurements were accompanied by complementary transmission electron microscopy (TEM) analysis on a microscopic level. Electron diffraction measurements of NWs viewed perpendicular to the [011] planes indicate that all NWs across the composition range grow along the <111>B thermodynamically preferred direction (Figure 3.4).[57,58] At high temperatures and slow growth rates, where precursor atoms can feely migrate on the surface during growth, $In_xGa_{1-x}P$ has a tendency to exhibit long range ordering and superlattice formation. In this type of long range ordering, typically called Cu-Pt ordering, (111) planes alternate between In rich and Ga rich composition, resulting in a superlattice, which is thought to be driven by surface reconstruction.[30,59-62] Initial evidence for a lack of long range ordering in the $In_xGa_{1-x}P$ NWs in this work comes from the absence of super spots in the electron diffraction images, which have previously been used to demonstrate ordering in $In_xGa_{1-x}P$ thin films.[59,62] Alternating In rich and Ga rich planes would have also shown up as contrast lines perpendicular to the growth direction in the HAADF-STEM image of the NWs.[62]

The $In_xGa_{1-x}P$ lattice constant expansion with increasing indium composition is directly measured through high resolution TEM (HRTEM) analysis (Figure 3.3C). Determined from the distance between (111) reciprocal lattice points in the Fourier transform of the HRTEM images, the lattice constant increases from ~5.4 Å to ~5.9 Å, when the indium composition increases from x=0 to x=1. The complete structural tunability demonstrated from the self-seeded solution phase growth method developed in this work overcomes limitations with commonly associated with MBE or LPE epitaxial growth, in which only a narrow $In_xGa_{1-x}P$ composition range can be synthesized.

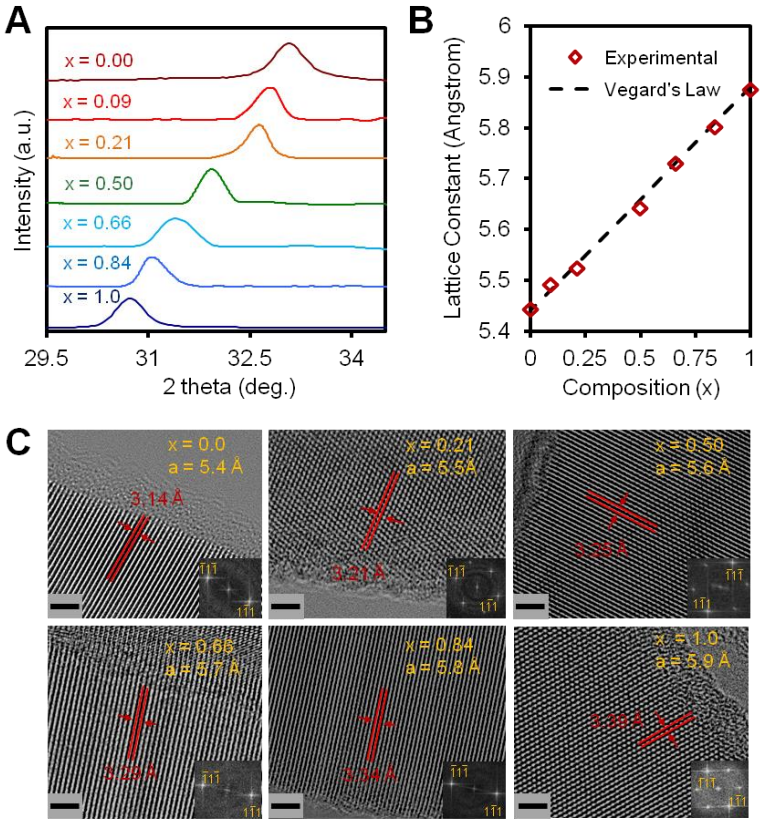

Figure 3.3. Powder XRD spectra (A) exhibit a shift in the (111) diffraction peak to larger 2 theta values with increasing Ga content, indicative of a lattice constant decrease. This lattice constant decrease is linear with composition, in accordance with Vegard's law (B). The lattice constant is additionally measured on single nanowires through analysis of HRTEM images (C), in which the FFT points corresponding to the (111) planes perpendicular to the growth direction were used for analysis.

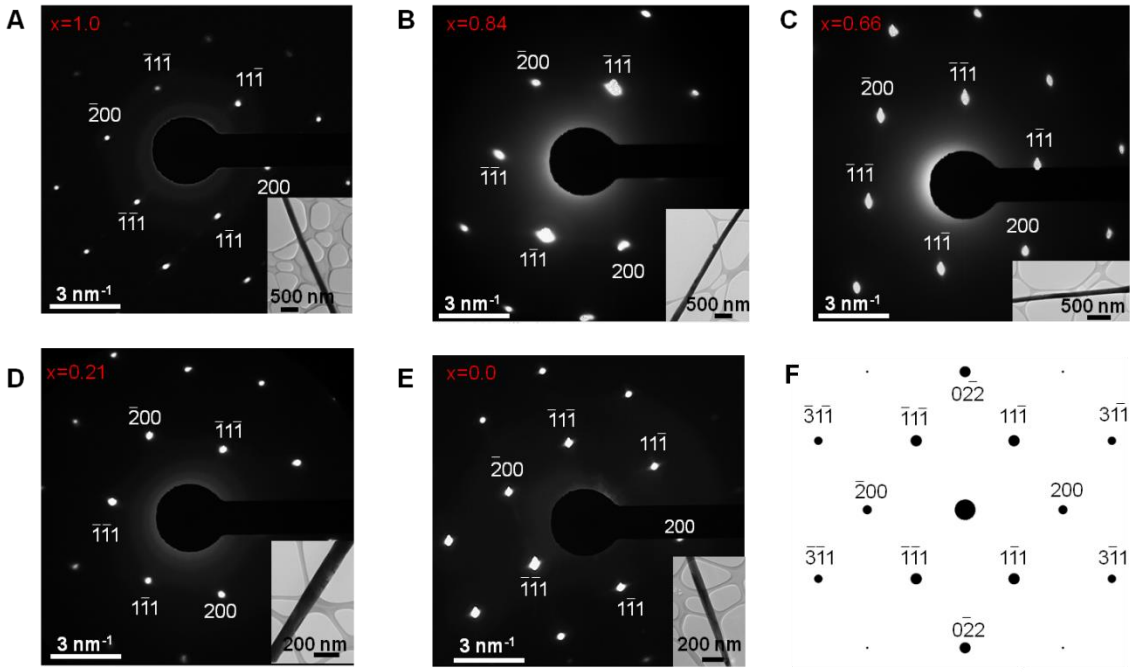

Figure 3.4. Electron diffraction of InP, $In_xGa_{1-x}P$ and GaP NWs rotated perpendicular to the [011] planes with composition indicated (A-E) reveals that the NWs grow in the [111]direction Simulated electron diffraction pattern (F) for zincblende InP viewed perpendicular to the [011] planes matches the experimental data. A simple structural model (G) shows several low Miller index planes of the zincblende crystal structure.

Additional insight into compositional homogeneity and crystal structure was acquired with Raman spectroscopy, a technique that has been applied to $In_xGa_{1-x}P$ alloys to study the presence (or lack of) long-range order and elemental composition.[63-68] We first measured the Raman spectra of InP and GaP NWs and compared to the corresponding bulk materials. The Raman spectrum of the NWs matches that of the bulk and exhibits two phonon modes: one transverse optical (TO) and one longitudinal optical (LO) mode. Next, we acquired Raman spectra and studied the corresponding modes for $In_xGa_{1-x}P$ across the composition range of $0 \leq x \leq 1$ (Figure 3.5A) and noted three main phenomena: I) The TO mode frequency linearly increases from 305 cm^{-1} to 367 cm^{-1} with decreasing indium composition (Figure 3.5B) while the LO mode frequency has a relatively large shift at x=0.6 but still varies continually from x=1 to x=0. This type of dispersion for the TO and LO modes has previously been reported in $In_xGa_{1-x}P$ as well as other alloys and was attributed to a one mode behavior in which the phonon mode frequency continually shifts from the frequency of one pure material to another.[68,69] If the $In_xGa_{1-x}P$ alloys were composed of individual InP and GaP domains rather than a true alloy, then separate, distinct TO and LO modes would be expected, rather than a shift in frequency with composition. II) The phonon modes for the $In_xGa_{1-x}P$ NWs are broadened compared to modes for InP and GaP, increasing in FWHM from 12 cm^{-1} up to 20 cm^{-1} for x=0.41. This peak broadening has previously been attributed to a high degree of disorder in the material, suggesting the lack of long range ordering and superlattice formation in the NWs.[67] III) In studies of $In_xGa_{1-x}P$ with a

high degree of long range ordering and superlattice formation, an additional, sharp phonon mode at 351-354 cm^{-1} appeared and was attributed to a longitudinal optical phonon due to the <111> long range ordered superlattice in $In_xGa_{1-x}P$.[70-72] The lack of this feature in our spectra is consistent with our electron microscopy evidence for a disordered $In_xGa_{1-x}P$ crystal lattice.

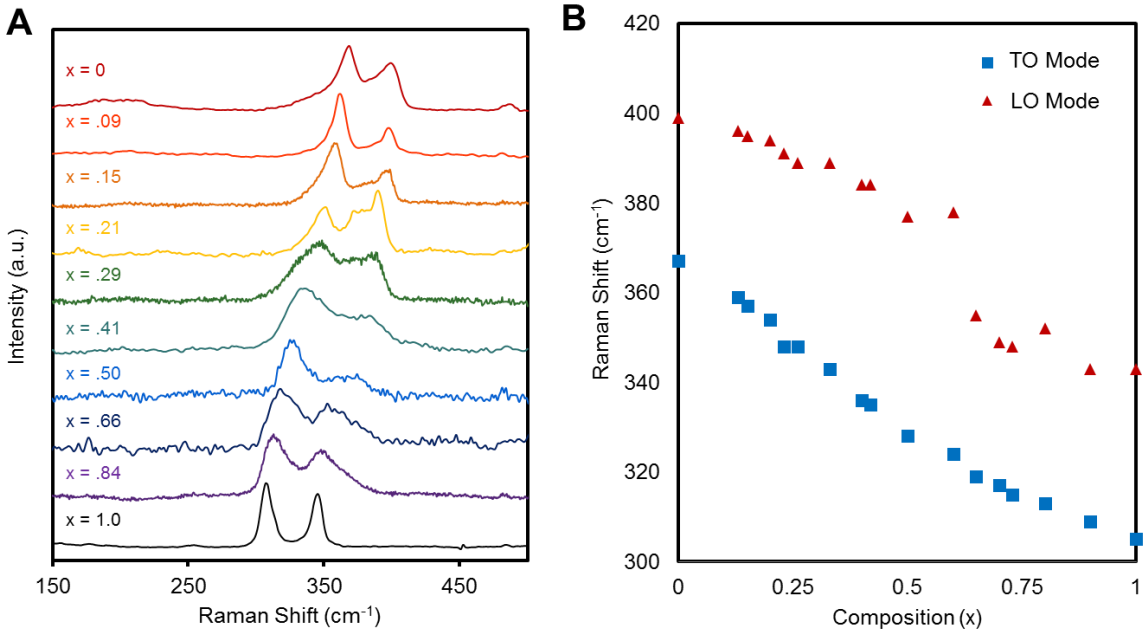

Figure 3.5. The evolution of the Raman spectrum of $In_xGa_{1-x}P$ NWs (A) shows a broadening of the phonon modes relative to InP and GaP, indicative of a disordered crystal structure. The $In_xGa_{1-x}P$ NW Raman spectra show a one mode behavior (B), in which the frequency of the LO and TO phonon modes varies continuously with composition.

Following the structural and Raman analysis, we focused on characterizing the optical and electronic properties of the $In_xGa_{1-x}P$ NWs. Of particular interest is the transition from an indirect to a direct band gap material, which is thought to occur at approximately x=0.25 in the bulk.[42] To measure the evolution of the band gap with composition and to pinpoint this direct to indirect transition in our material, systematic band gap measurements were employed on both a macroscopic and microscopic level. First, the band gap was measured through the band edge photoluminescence (PL) of the In_xGa_{1-x} NWs with various compositions (Figure 3.6A). The PL peak wavelength decreases from the near infrared (NIR) to the visible range with decreasing indium composition, and strong PL emission at wavelengths as low as 580 nm can be detected for NWs with composition x=0.21. The diameter of the NWs is well above the ~11 nm Bohr exciton radius of InP and GaP so quantum confinement effects are not expected in our system and variations in PL emission wavelength are due to variations in NW composition.[29] Within the same batch of NWs, the PL peak energy varied slightly between individual wires, approximately ±25 nm, indicative of small compositional variations within each batch.

Time-resolved photoluminescence (TRPL) spectra are plotted in figure 3.6B for nanowires with compositions x=0.21, 0.41, and 0.84. The PL decay kinetics are fit to a bi-exponential decay function with short component lifetimes of 0.034±0.0006, 0.026±0.0003, and 0.16±0.004 nanoseconds and long component lifetimes of 0.78±0.008, 0.96±0.01, and 1.51±0.02 nanoseconds for NWs with compositions x=0.21, 0.41, and 0.84, respectively. A bi-exponential fit with a slow component of 0.5-2.0 nanoseconds is typical for radiative band to band recombination in a direct band gap semiconductor, and the measured lifetimes are consistent with those previously reported for direct band gap $In_xGa_{1-x}P$ of 1-3 nanoseconds.[73,74] This provides additional evidence that the luminescence observed is from a band to band radiative recombination as opposed to processes such as defect emission or indirect band gap emission, which have radiative lifetimes on the order of tens of nanoseconds to microseconds.[51,75] The control of PL emission from visible to NIR energy range is expected to have applications toward tunable $In_xGa_{1-x}P$ based LEDs and NW lasers.

The band gap of the NWs was next recorded with UV-Vis-NIR absorption measurements using an integrating sphere setup. Figure 3.6C shows the absorption spectra of thin NW films deposited onto transparent glass substrates, where the absorption edge blueshifts with decreasing indium composition, x, and increasing band gap, from the NIR to the visible energy range. Samples with a composition of $x \geq .21$ featured a sharp increase in absorption at the band edge, consistent with the typical absorption profile of a direct band gap material. In contrast, the samples with $x<0.21$ have indirect band gaps and feature slowly increasing absorption, and only a sharp absorption increase at higher energies where their direct band gap lies.

Microscopic band gap measurements were next employed through monochromatic, low loss, electron energy loss spectroscopy (EELS). A unique advantage of EELS is the ability to obtain the electronic structure of materials with a very high spatial resolution, rendering this technique uniquely suitable for single NW studies.[76] In these measurements, inelastically scattered electrons are measured and the band gap is typically determined by the position of the energy onset of the electron loss peak in the low loss region (0-10 eV). Because such a measurement will be affected by parameters like material thickness, and instrument configuration, all parameters were kept consistent across the measurements. After measurement, the band gap was extracted from the raw data through a commonly used power law fit peak subtraction method.[77] Processed EELS data from wires with varying composition is plotted in figure 3.6D, with GaP and InP NWs serving as internal standards to verify our measurement and method of band gap determination. Our low loss EELS data shows the band-edge electron energy loss peak onset shifts from 1.35 eV for InP wires to 2.30 eV for GaP wires, with $In_xGa_{1-x}P$ alloys having band gaps intermediate between the two, which is consistent with our PL and absorption data. Because different EELS processing methods can yield varying results, an alternate method to extract the band gap was used and gave similar results.

In addition to band gap quantification, low loss EELS measurements can reveal the nature of inter band transitions (direct *vs.* indirect) and are used in this work as a complementary technique to determine the direct to indirect band crossover. The slope of the EELS onset peak for inter band transitions is determined by the valence and conduction band joint density of states (JDOS).[77] For direct band gap semiconductors, the JDOS, and consequently the EELS signal intensity at energies greater than the band gap (E_g), increases as $(E-E_g)^{1/2}$; The EELS onset for InP NWs is fit using this direct band gap function. For indirect band gaps materials, the EELS signal is proportional to the JDOS of indirect band gap semiconductors, which follows a $(E-E_g)^{3/2}$ relation, and the EELS data for GaP NWs is fit using the $(E-E_g)^{3/2}$ function. $In_xGa_{1-x}P$ alloy EELS

data was next analyzed, and the direct to indirect transition is observed through the EELS onset changing from an $E^{3/2}$ to an $E^{1/2}$ shape at compositions of x=0.21. At this composition, there are contributions to the signal from both direct and indirect transitions, resulting in a seemingly linear intensity increase and an imperfect fit using either model. However, when x is continually increased, the slope of the EELS peak resembles more than the $E^{1/2}$ relation as the direct band gap becomes the primary transition.

The comprehensive band gap measurements from PL, absorption and EELS measurements are plotted as a function of composition in figure 3.6E along with the calculated band gap using literature values. PL measurements correlating with individual NW composition were also acquired and follow a similar trend. For $In_xGa_{1-x}P$, the band gap changes from direct to indirect at x~0.21, when the lowest energy point in the conduction band changes from the Γ valley (direct) to the X valley (indirect).[42] The transition from direct to indirect band gap can also be pinpointed through the analysis of the volume-normalized PL intensity as a function of PL energy.[20,78,79] The band gap energy value is not linear with composition but bowed due to microscopic fluctuations in local strain, core potentials, and other nearest neighbor effects that lead to a deviation from a perfectly periodic potential felt by electrons.[80] As a result, the band gap, $E_\Gamma(X)$, as a function of composition, X, of an alloy of materials A and B follows the relation: $E_\Gamma(X) = E_\Gamma{}^A(X) + E_\Gamma{}^B(1-X) - cX(1-X)$ where c is the bowing parameter and $E_\Gamma{}^A$ and $E_\Gamma{}^B$ are the band gaps for materials A and B. For $In_xGa_{1-x}P$, the bowing parameters of 0.65 and 0.2, taken from previous literature reports, were used to calculate the Γ (direct) and X (indirect) band gaps, respectively.[81] Our experimental data from PL, absorption, and EELS follows these calculated values. The correspondence between predicted and experimental band gap energies is a promising demonstration of controllable electronic tunability that is offered through this solution phase $In_xGa_{1-x}P$ NW synthesis.

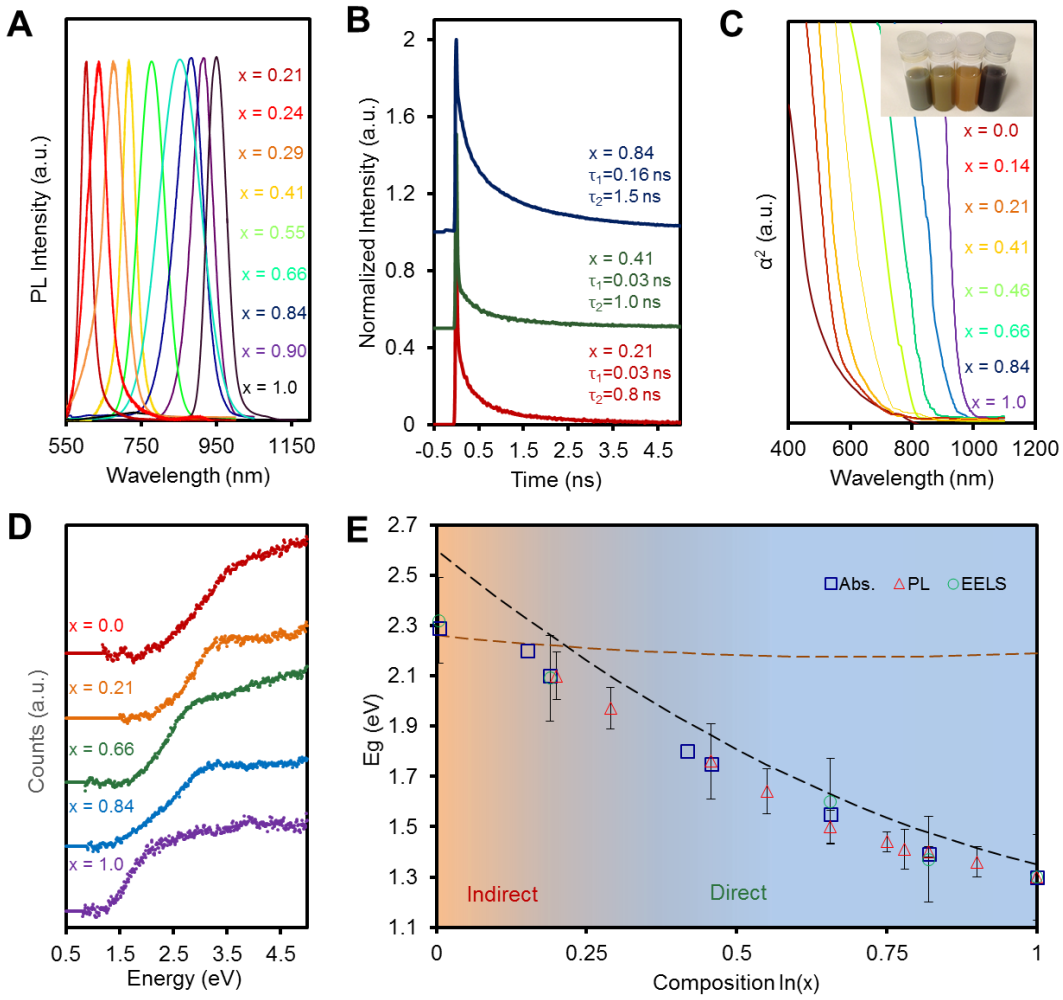

Figure 3.6. Band gap measurements of $In_xGa_{1-x}P$ NWs. PL spectra (A) illustrate an increase in band gap as the PL peak position blueshifts with decreasing indium composition. Time-resolved PL spectra (B) show that NWs with x>0.2 have lifetimes in line with those previously measured for direct band gap $In_xGa_{1-x}P$. UV-Vis absorption spectra (C) also show a blueshift with decreasing indium composition. The inset shows NWs with compositions x = 0, 0.14, 0.21, and x=0.41 dispersed in acetone. EELS spectra (D) of NWs show an increase in onset energy with increasing gallium composition. Comprehensive band gap *vs*. $In_xGa_{1-x}P$ composition (E) and the direct to indirect transition.

To demonstrate proof of principle PEC applications of the solution phase synthesized NWs, we developed photocathodes using InP as the light absorbing component. Indium Phosphide (InP) is an attractive material to use as a photocathode for the hydrogen evolution reaction (HER) because its direct band gap of 1.35 eV is well matched to the solar spectrum and the conduction band edge is located at a sufficiently high potential energy to thermodynamically drive the reduction of protons to hydrogen. This material has been utilized previously as a highly efficient photocathode for the HER but many of these studies relied on single crystal wafers,

which require a large amount material and an expensive growth process. Reduction of total material usage can be achieved through using a thin film of high surface area nanowire film and would have the additional benefits of light trapping effects and increased reactive site density.

We synthesized p-type InP NWs by the inclusion of a zinc precursor, diethylzinc (DEZ) into the precursor mixture. Optimized NWs contained 0.74% Zn as measured by inductively coupled plasma atomic emission spectroscopy (ICP-AES). To obtain more quantitative information about the electrical properties of the Zn doped NW's, field effect transistors (FET's) were fabricated on a series of NW's with 0.74% Zn loading amount using Pt or Ni/Au contacts (figure 3.7 A,B). The Zn doped NW's showed p-type behavior and measured carrier mobility of up to 87.2 $cm^2/V*S$. However, this is the lower boundary for the actual mobility because the NWs were not long enough to conduct 4 point measurements to exclude the effects of contact resistance. The highest measured mobility of these low temperature solution phase synthesized nanowires is two to five times lower than that of VLS grown NW's at higher temperatures. The resulting carrier concentrations of $3*10^{17}/cm^2$ and $9*10^{17}/cm^2$ from devices using Ni/Au and Pt contacts, respectively, is consistent with the value estimated from open circuit photovoltage measurements and is lower than the 0.74% measured by ICP-AES. This is further evidence the active dopants in the NWs result from a small fraction of the actual Zn in the lattice.

To utilize the InP NW's in PEC solar-to-fuel conversion, InP NW cathodes were assembled onto conductive ITO substrates through the Langmuir-Blodgett (LB) technique to maximize the NW-substrate contact (figure 3.7C). To reduce kinetic limitations at the NW-electrolyte interface, the NWs were loaded with photo-deposited platinum nanoparticles serving as model HER co-catalysts.

Following catalyst loading and LB assembly, the PEC properties of the NW electrodes were measured in a pH 5.2 acetate buffered electrolyte solution (figure 3.7 D). The poor fill factor indicates a large amount of series resistance through the circuit. He main points in resistance are likely the NW-solution interface, the NW material, and the NW-substrate interface. However, the photocurrent onset potential of ~0.6-0.7 v vs. RHE is relatively high. This is promising when aiming to combine this material with a photoanode for unassisted water splitting in a tandem configuration. Furthermore, the NW electrodes displayed exceptional stability in slightly acidic solutions, showing no signs of decomposition even after 10 hours of operation. While offering an alternative to single crystal wafers, the electrodes processed from solution phase grown InP NWs suffer mainly from low photocurrent. Strategies to improve upon this include the growth of InP directly off of a conductive substrate and will serve as the next step in this line of research.

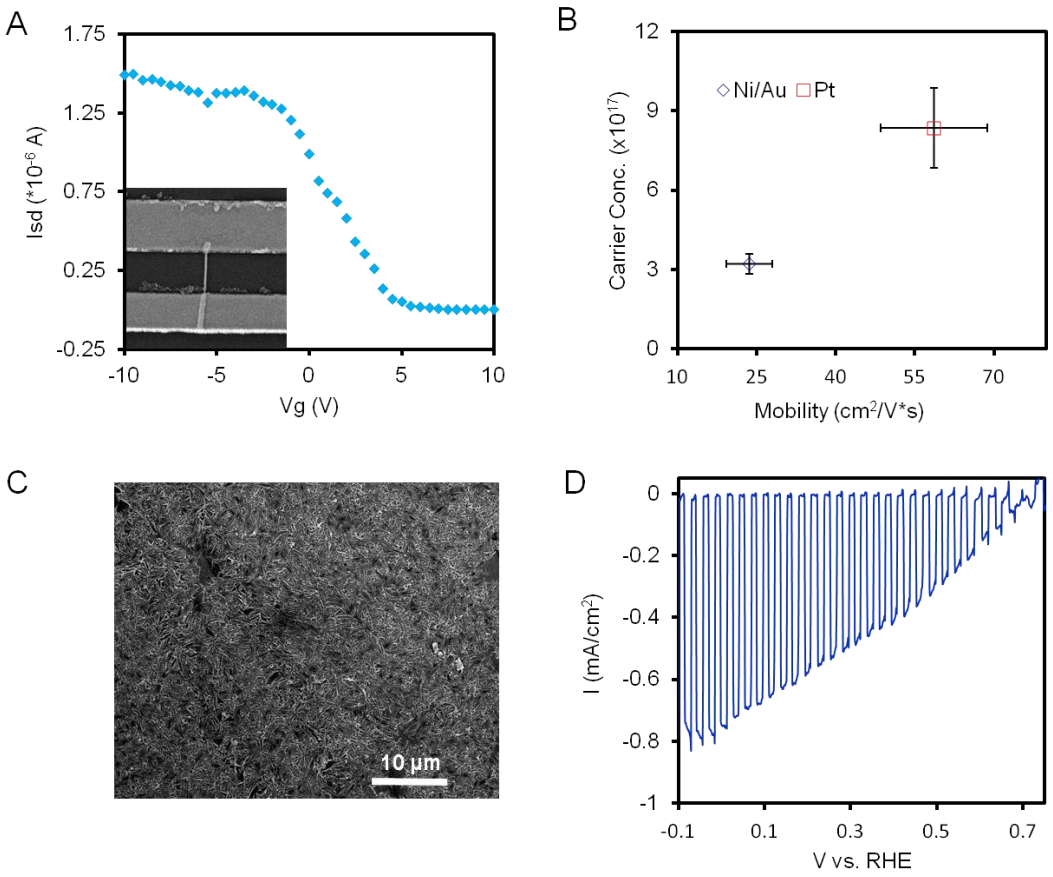

Figure 3.7: InP NW electrical properties were measured by fabricating field effect transistors (A). The inset shows the working device. Carrier concentration and mobility of the NWs were determined to be 3-9*10^{17}/cm^3 and 36-70 cm^2/V*s, respectively. InP NW photocathodes were fabricated by assembling InP NWs on a conductive ITO surface (C). Current-voltage characteristics of the NW photocathodes (D) show promise for further development of this material.

3.3 Concluding Remarks

In conclusion, we have developed a novel synthetic approach to obtain fully tunable $In_xGa_{1-x}P$ NWs *via* a pre-seeded solution phase synthesis. Using complementary macroscopic and microscopic measurements, we have demonstrated access to every composition across the $0 \leq x \leq 1$ range. XRD and TEM measurements demonstrate a tunable lattice constant while electron diffraction and Raman spectroscopic measurements indicate that the $In_xGa_{1-x}P$ NWs are likely a disordered alloy and do not feature significant long range ordering or superlattice formation. The band gap tunability and change from direct to indirect band gap was measured through PL, optical absorption, and EELS measurements. While this work focuses on $In_xGa_{1-x}P$, our synthetic

method can potentially be applied to other alloy systems with precursors compatible with the synthetic conditions, opening up an new avenue to access and utilize III-V, II-VI and other alloys *via* a low temperature scalable synthesis. InP NWs were next implemented as photocathode materials whose performance shows promise for the further development of this material.

Parts of this section were published in: “Solution Phase Synthesis of Indium Gallium Phosphide Alloy Nanowires” **N. Kornienko**, D. Whitmore, Y. Yu, S. Leone and P. Yang, *ACS Nano*, 9, 3951 (2015)

4. InP Vapor Phase Synthesis and Photocathode Development

4.0 Preface

In this section we aimed to develop highly efficient photocathodes from vapor phase NWs. The overall goal of this was to develop a functional alternative to silicon, which is commonly used but limited in its photo voltage. We choose InP as a target material because it has previously displayed high photovoltages in PEC half cells. We pursued a growth directly on conductive substrates to maximize electrical connectivity and therefore efficiency.

4.1 Introduction

Increasing fossil fuel consumption and the resulting environmental damage have propelled many efforts in clean energy research. Solar power is among the most promising of such clean and renewable energy sources. However, due to the intermittent nature of sunlight and the temporal mismatch between solar energy flux and peak power consumption, a method for capturing and transforming sunlight into an energy dense storage medium must be realized. To this end, photoelectrochemistry (PEC) offers a potential avenue of doing so by using solar power to split water into oxygen and hydrogen, which can subsequently be used as an energy storage medium, fuel source, or chemical feedstock.[5]

One promising strategy towards PEC solar fuel generation is the utilization of a Z-scheme method.[82-91] This is a biomimetic approach that simulates photosynthetic systems consisting of a tandem, dual absorber configuration (figure 4.1A). The primary advantages of using two separate light absorbers to carry out the reduction and oxidation reactions include 1) each light absorber is required to possess appropriate band edge positions only for the relevant hydrogen evolution reaction (HER) or oxygen evolution reaction (OER), 2) each light absorber needs to be stable only under the reducing or oxidizing conditions that it operates, 3) the voltage required to split water (practically ~1.7 V) can be provided by the combination of the two light absorbers and 4) the band gaps for the light absorbers can be selected to efficiently take advantage of separate parts of the solar spectrum, thus enabling a higher solar to fuel efficiency compared to using only a single light absorber.[92,93]

A multi-component Z-scheme PEC cell can be treated as a modular system in which each building block (light absorber, catalyst, electrolyte, membrane) can be individually modified, optimized and subsequently re-integrated to improve the device as a whole. One can estimate the efficiency of an integrated PEC system from the crossover of overlaid current-voltage (I-V) curves of the individual light absorber/catalyst components.[94] As illustrated in figure 4.1B, the efficiency of conventional PEC systems typically suffers from a lack of photovoltage from commonly used photocathodes as well as from insufficient photocurrent from typical photoanodes. Within this context, the present work focuses on the development of an improved light absorbing photocathode constituent. Indium phosphide (InP) is a promising candidate to replace commonly used silicon because it has a relatively narrow bandgap (1.35-1.42 eV) that can take advantage of a large portion of the incident solar spectrum and has been shown to exhibit exceptionally high voltages in PEC half cells.[95-98] The typically high carrier mobility and low surface recombination velocity of this material are beneficial for efficient charge separation and catalysis.[99,100] Furthermore, only a small amount of InP is necessary to fully absorb incident

solar radiation because of its direct band gap. Utilizing InP in the NW morphology offers the additional benefits of a high surface area for increased catalyst loading and decreased reflection of incident photons through light trapping effects.[101,102] Moreover, the growth of InP NW arrays on silicon substrates as opposed to the commonly used InP substrates can make InP NW-based photocathodes more practical for scale up by minimizing cost and material consumption.

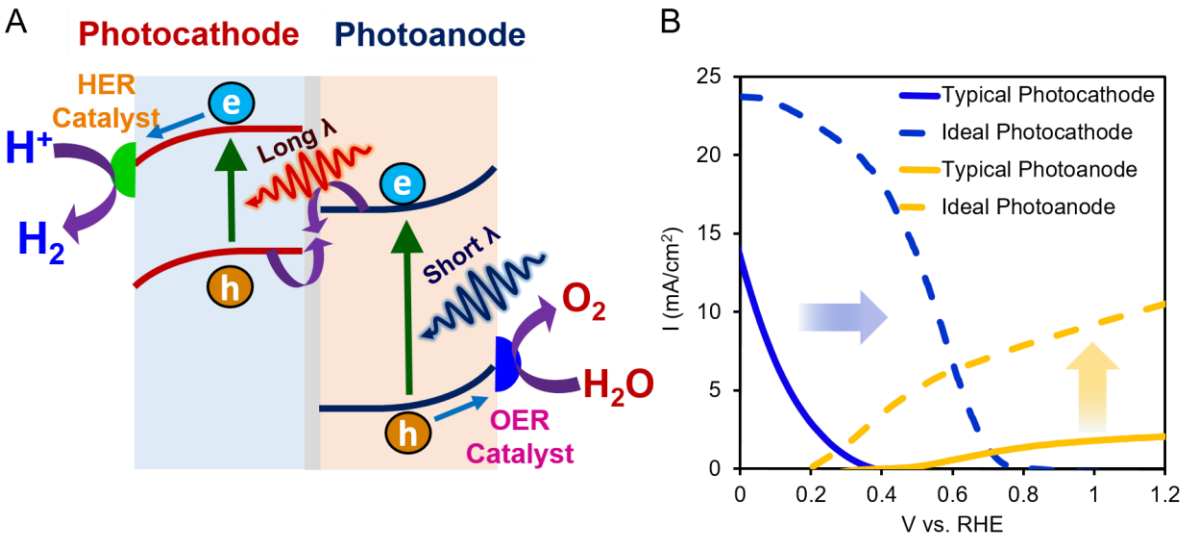

Figure 4.1. A modular Z-scheme PEC system is illustrated (A) in which individual light absorber and catalyst components can be systematically improved before re-integrating into the overall system. Typical PEC integrated systems' performance suffer from insufficient photocathode voltage and photoanode current (B).

In the following sections, we detail a study on the growth of InP NWs on silicon substrates. Following synthetic and structural analysis, we tune the InP NW electronic character by incorporating Zinc (Zn) as a p-type dopant and proceed to study the material's optical and electrochemical properties. We next photodeposit platinum (Pt) HER catalysts onto the NWs and utilize our InP photocathodes in both PEC half cells and in integrated water splitting systems with a bismuth vanadate ($BiVO_4$) photoanode.

4.2 Nanowire Growth

Indium phosphide has been previously synthesized using a variety of different methods, including solution phase synthesis,[103-107] phosphorization of indium films,[108,109] chemical vapor transport (CVT),[110,111] laser ablation,[112] and chemical vapor deposition (CVD).[113-125] In this work we pursued the CVD method since its growth parameters can be precisely fine-tuned and it offers a path to directly grow InP NWs on a conductive substrate. Degenerately doped, p-type, <111> Si was chosen as a cost effective conductive growth substrate. The silicon carrier concentration would minimize substrate PEC contribution and facilitate the InP majority carrier transport through the PEC circuit. Though an ~8% lattice mismatch exists between InP and Si, InP NWs have been previously grown with success on <111> Si substrates.[114,117,126] In this particular project design, we aimed to obtain InP NWs that were long enough to absorb the

majority of above band gap radiation and wide enough to support a full built in interfacial electric field with moderate doping concentrations.

With these design principles in mind, we developed a self-catalyzed growth of InP NWs on <111> Si substrates with a metal-organic CVD (MOCVD) process incorporating trimethylindium (TMIn) and *tert*-butylphosphine (TBP) as indium and phosphorus precursors, respectively (figure 4.2A). Detailed growth parameters are included in the experimental section. We did not observe an indium metal catalyst at the tip of the NW but rather a clean end-facet or a polycrystalline tip. The catalyst tip was likely either fully consumed during the growth or soon after the TMIn flow was turned off. Time-dependent growth analysis (figure 4.2B,C) with 10 standard cubic centimeters per minute (SCCM) TMIn and 500 SCCM TBP precursor flows revealed that the growth begins with small needle-like structures that continually grow in the vertical and radial directions linearly with time to generate larger, faceted NWs. By varying the growth time, the dimensions of the NWs can be tuned to span two orders of magnitude in both the vertical and radial dimensions. Seeking to obtain a further understanding of the NW growth and to demonstrate an additional layer of synthetic tunability, we varied the TBP/TMIn ratio. While keeping the TBP flow constant at 500 SCCM, we modified the TMIn flow and discovered that the primary effect of this was the modulation of the NW aspect ratio. Representative NWs from 20 min. growth times utilizing TMIn flow rates of 3-30 SCCM are depicted in figure 4.2D. The base diameter remained unchanged while the vertical growth rate increased with TMIn flow until nearly leveling out at rates of 15 SCCM (figure 4.2E). This indicates that the TMIn component was crucial for lateral growth. A TMIn flow is likely necessary to maintain a constant liquid indium catalyst at the growing NW tip and the presence of this catalyst accelerates the vertical growth rate. The constant base diameter over the entire experimental TMIn flow range points to TMIn not being the limiting factor for the sidewall growth rate under these conditions.

Next, while holding the TMIn flow constant at 15 SCCM, we decreased the TBP flow from 500 to 50 SCCM (Figure 4.1F, right to left). Here we discovered unusually shaped NWs that had a wide base yet terminated with a very thin (~20 nm) end section. While the TMIn was crucial for lateral growth, under these synthetic conditions, TBP flow dictates radial growth dynamics with sidewall growth initially occurring near the base of the NW. These experiments together support a dual growth mechanism, consisting of self-catalyzed lateral growth in conjunction with uncatalyzed epitaxial sidewall growth. In a TBP-deficient regime, radial sidewall growth proceeds by beginning at the base of the NWs and is outpaced by the lateral growth. A similar phenomenon was observed with InGaAs nanostructures in which a lower tert-butylarsine precursor flow resulted in asymmetric structures with a wide base and a thin needle-like tip.[127] Here the authors attributed this to a result of increased group III adatom diffusion lengths under low group V precursor flows and, as a result, faster vertical growth rates. It should be noted that the growth of InP NWs presented here is not confined to <111> silicon substrates; InP NWs were also grown on <100> silicon, gallium nitride, and molybdenum substrates.

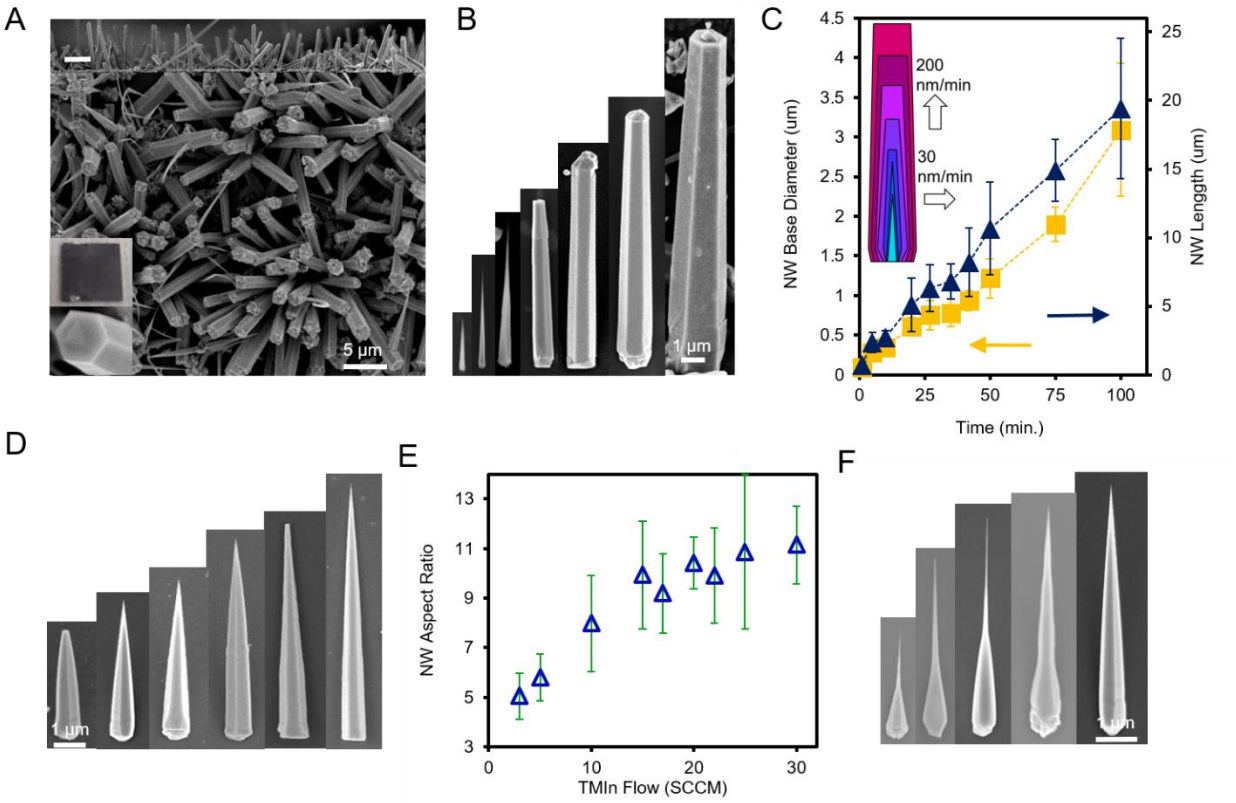

Figure 4. 2. A growth for InP NW arrays was developed (A). The insets depict a typical faceted NW tip and a 1x1 cm Si chip with an InP array. The NW length and diameter both increase linearly with growth time (B,C). Representative InP NW's under varied TMIn precursor flow from 3 to 20 SCCM (left to right) (D,E) indicate that the TMIn component is critical for the NW vertical growth rate while the diameter remains consistent. In contrast, modifying the TBP flow from 50 to 500 SCCM (left to right) changes the radial side wall growth kinetics of the InP NWs (F).

4.3 Structural Characterization

We next utilized microscopic characterization methods to determine the crystallographic phase of the InP NWs. High resolution transmission electron microscopy (HRTEM) images (figure 4.3 A,B) taken perpendicular to the [-12-10] and [1-100] zone axes reveal that the InP NWs grow in the wurtzite (WZ) phase with a <0002> growth direction. Electron diffraction images (figure 4.3 C-E) from the InP NWs aligned to the [-12-10], [1-100] and [0002] axes indicate that the hexagonal NWs have facets perpendicular to the {1-100} axes and edges perpendicular to the {1-210} axes. From the comprehensive crystallographic measurements, a structural model is derived (figure 4.3F). X-ray diffraction (XRD) was utilized as a macroscopic structural measurement. The WZ phase is the primary contribution to the XRD spectrum though a zincblende (ZB) component is also present. This is likely from a layer of InP ZB particles on the substrate that grow in conjunction with the NWs as well as from the NW tips, which occasionally terminate with a polycrystalline ZB layer.

InP adopts the ZB phase in the bulk but the WZ phase is commonly observed in InP nanostructures. This can be rationalized by the high surface to volume ratio of nanostructures; ZB is the thermodynamically preferred phase in the bulk but WZ has a lower surface energy due to a smaller density of surface dangling bonds.[118,128] Hence, InP NWs with diameters less than 25 nm typically adopt the WZ phase. Because the growth of our NWs initiates with thin needle-like seeds and proceeds to grow in an epitaxial fashion, the WZ phase is not unexpected. Beyond the initial stages of growth, the NW's are likely trapped in a metastable regime in which the WZ is no longer the lowest energy phase but a large energy input would be required to transform the crystal to the ZB phase.

An additional parameter that affects the resulting crystallographic phase of InP NWs is the V/III precursor ratio, with higher ratios leading to the WZ phase.[50,52,129-131] This phenomenon has previously been exploited to gain precise crystallographic control of III-V NWs and even grow periodically twinned NWs.[122] In these cases, the preferred formation of the WZ phase was attributed to effects of varied growth kinetics, catalyst supersaturation, surface energies, and precursor mass transport limitations. Often times, high V/III precursor ratios lead to the WZ phase; our resulting NWs are grown with a typical V/III ratio of ~1000, thus the WZ phase is expected.

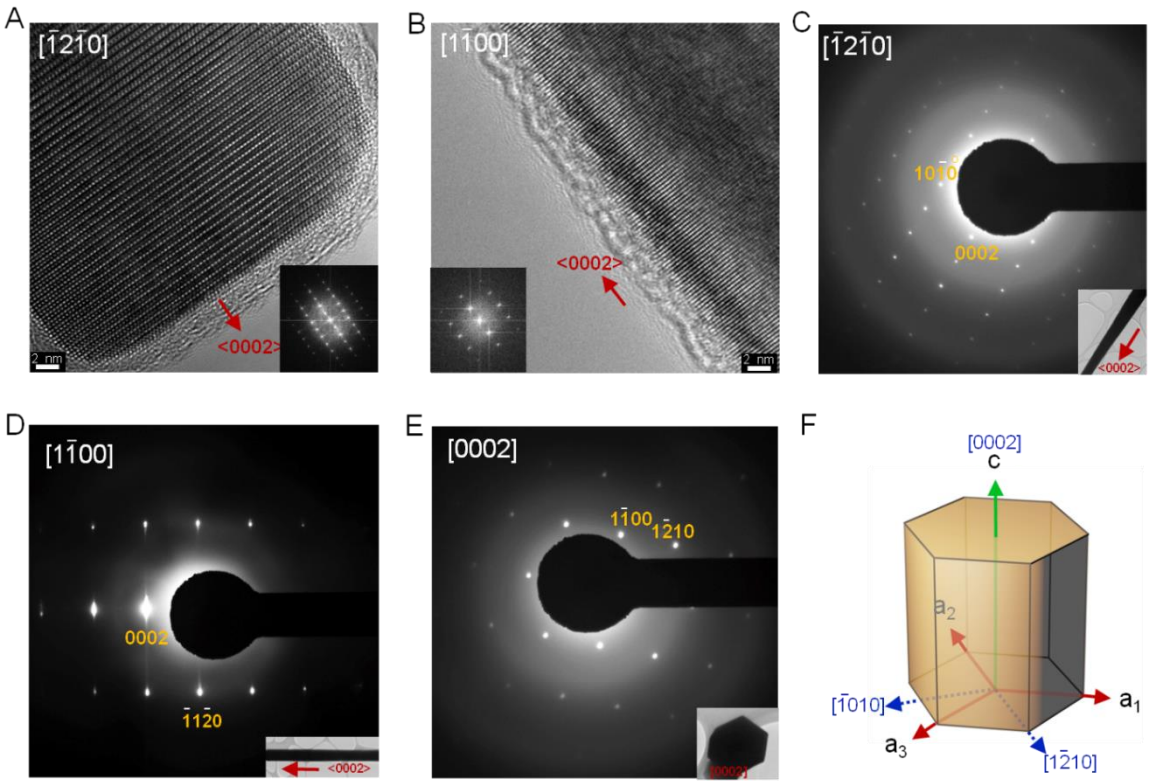

Figure 4.3. HRTEM (A,B) and electron diffraction (C-E) demonstrate that the InP NWs grow in the WZ phase with a <0002> growth direction, [1-100] side facets, and corners aligned with the [1-210] facets. A structural model is produced from the HRTEM and electron diffraction data (F).

4.4 Zinc Doping

Following the growth and structural studies, we proceeded to develop photocathodes from the InP NWs. For all subsequent studies, InP NW's with 15 SCCM TMIn, 500 SCCM TBP, and 20 min. growth times were used. Because InP grows intrinsically n-type as a result of phosphorus vacancies and oxygen impurities, it is critical to introduce a p-type acceptor to render InP suitable for photocathode fabrication.[132-134] Zn was chosen as a p-type substitutional dopant because its ionization potential lies near the InP valence band, and is the most commonly studied InP p-type dopant.[135] The as-grown InP NWs were doped with Zn *via* a thermal diffusion (400-700^{o} C for 1 hour under 10% H_2/Ar) based process using zinc phosphide both as source of Zn and to maintain a phosphorus rich atmosphere during the doping process.[136] We note that the actual local temperature of the InP and Zn source is likely to be substantially lower than the set point of the tube furnace heat source.

4.5 Optical Characterization

Steady-state photoluminescence (PL) and time-resolved photoluminescence (TRPL) measurements were performed on the as-grown and Zn-doped NWs. For this section, NWs doped with Zn at 550^{o} C were measured since they were found to exhibit optimal electrochemical properties. Steady state PL spectroscopy of as-grown InP NWs reveals that they emit at a wavelength of ~862 nm (1.44 eV) (figure 4A). In addition to the primary emission peak, a lower energy shoulder is present. This phenomenon is consistent with previous measurements of InP in the WZ phase and is attributed to valence band splitting in the band structure.[137-141] Zn doped NWs feature a red-shifted emission at ~878 nm (1.41 eV). A possible explanation for this could be radiative emission from a donor-acceptor transition.[142]

To further probe the optical properties of both types of NWs, we examined their PL emission *via* time-resolved measurements. We measured the lifetime of the NWs across six orders of magnitude of excitation intensity. The purpose of this was to glean information about the excited state recombination dynamics. For both types of NWs, the PL decay curves could be fit with a bi-exponential decay pattern (figure 3B). Bi-exponential decays in semiconductor materials typically indicate the presence of a faster defect or surface related component and a band to band recombination component. In our case, the fast component typically contributed to 70-80% of the data while the slow component contributed to 20-30% of the decay curve.

As excitation intensity is increased from 0.462 to 46200 mW/cm^2, the lifetime of both components decreased (figure 3C, D), providing evidence that in this regime, traps (likely due to surface states and crystallographic defects) are already filled and multi-electron processes are accelerating recombination kinetics. In addition, the as-grown NWs show consistent behavior while Zn-doped NWs exhibit a much larger spread (figure 4E, F and S4) in their lifetime values. This variation of optical properties is likely a result of the high temperature annealing in a Zn and P rich environment and may stem from the addition or elimination of various defects that may vary from wire to wire. This result indicates that the homogeneity of the NWs through the doping process could be improved and the effects of optical heterogeneity on the overall device performance remain an open question.

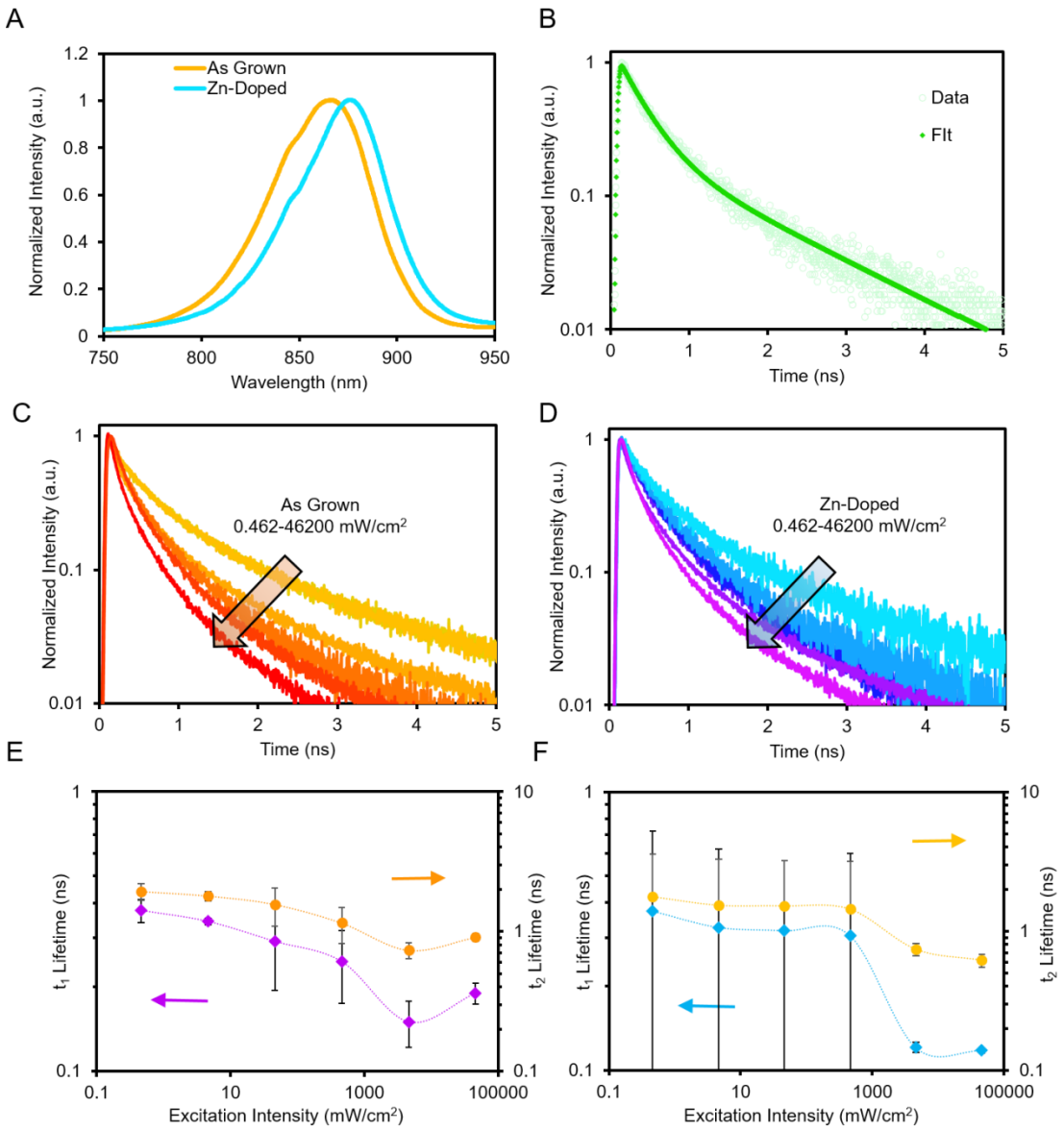

Figure 4.4. Steady state PL emission is slightly red-shifted for Zn-doped NWs relative to as-grown NWs (A). The PL lifetimes of NWs can be fit to a bi-exponential decay (B) in the case of as-grown as well as Zn-doped NWs. Both as-grown (C) and Zn-doped (D) NWs exhibit a decrease in PL lifetime with increasing excitation power. In contrast, the as-made NWs show far less heterogeneity in their lifetime distributions (E) relative to the Zn-doped NWs (F). t_1 and t_2 denote the fast and slow components in the photoluminescence decay.

4.6 Flat Band Potential Measurement

In this section, we examine the effects of Zn doping on the flat band potential of the InP NWs using open circuit photovoltage (OCP) and Mott-Schottky measurements. The flat band potential and interfacial band bending of the InP NWs were optimized by varying the temperature of the thermal diffusion Zn doping process. At elevated temperatures, Zn diffuses rapidly through the InP lattice.[143,144] Therefore, the primary factor that controlled the resulting concentration of Zn in the InP lattice was the temperature dependent partial pressure of gaseous Zn.[145] OCP measurements were first utilized to test the degree of band bending at the InP surface after the doping process. Briefly, after the ZnP thermal diffusion, an atomic layer deposition (ALD) titanium dioxide (TiO_2) layer was deposited onto the NW surface as a protection layer. Following the TiO_2 deposition, an indium-gallium eutectic was used to make an ohmic contact to the backside of the Si chip. In a three-electrode setup with a carbon foil counter and Ag/AgCl reference electrode, the working electrode potential was measured under dark and under one-sun illumination.

Figure 4.5 illustrates a simplified picture of the processes occurring during the OCP measurement: initially, the Fermi energy of the InP and the energy level of the redox couple in the (H^+/H_2) electrolyte lie at different positions on an absolute energy scale. Charge is injected into the InP (figure 4.5A) until the InP fermi energy equilibrates with that of the redox couple. This leads to a negatively charged region and downward band bending at the InP surface (figure 4.5B). In the case of a buried junction at the interface, the equilibration may occur between the semiconductor and shell material instead. When the InP electrode is illuminated at open circuit, electrons from the valence band are promoted to the conduction band, are driven to and build up at the semiconductor-electrolyte interface, leading to a splitting of quasi-fermi levels of electrons ($E_{F,e}$) and holes ($E_{F,h}$) (figure 4.5C). The degree of quasi fermi level splitting is measured by the change in the working electrode voltage under light and dark. This is an estimate of the attainable photovoltage under PEC operating condition.[146]

When considering the optimal doping level for our NW electrodes, of importance to us was to achieve a high enough doping level to support a full built-in electric field, without introducing an excessive amount of defects that can act as recombination centers and decrease photovoltage. The depletion width, W, is defined for a one-dimensional interface by:

$$W = \sqrt{\frac{2\varepsilon\varepsilon_0 \Delta V}{eN_d}}$$

where ε_0 is vacuum permittivity, ε is the InP dielectric constant, ΔV is the potential difference between the redox couple and the InP fermi level, e is the elementary charge and N_d is the carrier concentration. At insufficient carrier concentrations W is larger than the NW radius and a full built in electric field cannot be supported. W is plotted as a function of N_d and the results indicate that for a NW 500 nm in diameter, an N_d of at least ~10^{16} is required. A series of systematic OCP measurements as a function of ZnP annealing temperature were performed (figure 4.5D). Undoped InP displayed a negative OCP, indicating an upward band bending at equilibrium and likely an initial n-type character. The OCP was positive across our experimental range of annealing temperatures (400-700 ^oC), maximizing at 550 ^oC until decreasing again. This

is likely explained by the following: the NWs annealed at lower temperatures (400-450 ^{o}C) are fully depleted across their diameter. At optimal annealing temperatures (500-600 ^{o}C) the InP has an optimum carrier concentration and is no longer fully depleted. Higher temperature annealing (650-700 ^{o}C) leads to an increase in defects, through either excessive Zn incorporation or through thermal degradation, and OCP is likely reduced through defect-induced recombination.

An OCP plot from an optimized InP photocathode annealed at 550 ^{o}C is presented in figure 4.5E. At open circuit conditions, the electrochemical potential is at equilibrium with the primary redox couple in the acidic solution (H^+/H_2) at ~0V vs. RHE. Upon illumination and subsequent quasi-fermi level splitting the measured voltage increases to ~0.65 V vs. RHE. This can be viewed functionally as where the InP NWs can begin to generate a photocurrent. To determine whether this OCP measurement is close to the true value of the flat band potential, we measured the OCP as a function of illumination intensity. As presented in figure 4.5F, the OCP initially increases with increasing illumination intensity until ~100mW/cm^2, indicating that in this region, the OCP is likely dominated by the effects of non-radiative recombination. At illumination intensities higher than 100 mW/cm^2, the OCP increases at a much lower rate. This is evidence that at quasi-static equilibrium, the trap states are mostly filled, and the quasi-fermi level splitting is nearly maximized and thus approaches the true flat band potential.

The flat band potential was then independently measured *via* Mott-Schottky measurements. This particular technique measures the capacitance of the space-charge region (C_{sc}) in the dark under a range of applied potentials.[147] In an ideal system the C_{sc} obeys the relationship:

$$\frac{1}{C_{sc}^2} = \frac{2}{\varepsilon\varepsilon_0 A^2 e N_d}\left(E - E_{fb} - \frac{kT}{e}\right)$$

where A is the area of the semiconductor-electrolyte interface, N_d is the carrier concentration, E is the applied potential, E_{fb} is the flat band potential, and k is the Boltzmann constant. The Mott-Schottky plot for our optimized InP photocathodes in a commonly used frequency range for this material is depicted in figure 4.5G. The flat band potential can be measured and is determined to be at ~0.7 V vs. RHE. Importantly, this value converges with the flat band value measured through OCP measurements, providing confidence that we are indeed recording the C_{sc} in this measurement. Although a fully quantitative determination of carrier concentration is not possible due to uncertainties in the absolute area and the variability of slope under different frequencies, the carrier concentration in the InP was roughly estimated using double layer capacitance to record the surface area to be in the range of~2-8x10^{16}. Additional improvements in maximizing photovoltage and flat band potential can potentially be made through modification of the TiO_2 ALD process, minimizing crystallographic defect density, or introducing built in junctions through surface modification; these efforts may be pursued in future works.[95,124,136,148-150]

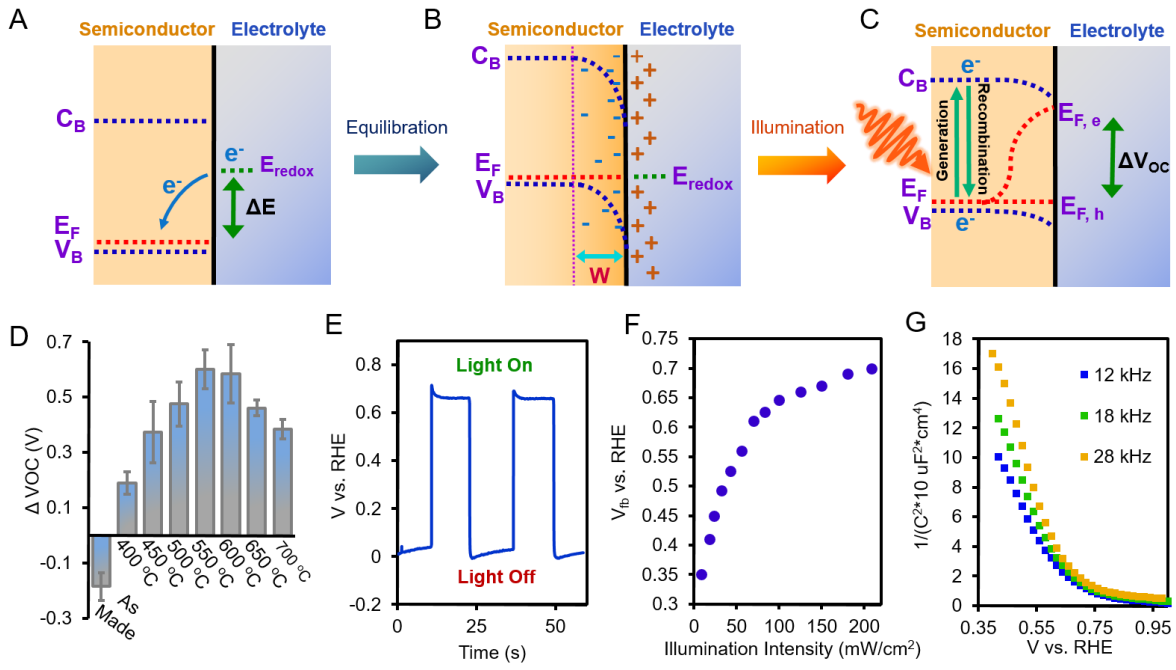

Figure 4.5. Due to differences between the semiconductor fermi level and redox couple electrochemical potential, charge is injected into the semiconductor (A) until the two levels equalize (B). This results in an interfacial built in electric field and band bending. The extent of the built in electric field into the semiconductor, the depletion width, W, is dependent on the semiconductor carrier concentration and difference between its fermi level and the redox couple potential. Upon illumination, minority carrier electrons are promoted to the conduction band until an equilibrium is reached between photoexcitation and recombination and the semiconductor bands flatten (C). The extent of the quasi fermi level splitting and flattening of the bands is measured through open circuit photovoltage measurements (D, E). The flat band potential measured through OCP does not change much with illumination intensity after 100 mW/cm^2, indicating that the measured value is close to the true flat band potential (G). Furthermore, Mott-Schottky measurements yield a flat band potential of ~0.7 V vs. RHE, which is consistent with OCP measurements (G).

4.7 Photoelectrochemical Half-Cell Performance

After optimizing the doping procedure through OCP measurements, the InP NW photocathode's photoelectrochemical performance was tested. First, platinum nanoparticles were photodeposited from a solution of Pt salt dissolved in a water-methanol mixed solvent (see experimental section for details). After optimization, this method yielded a well-dispersed coating of ~6 nm Pt particles on the InP surface (figure 4.6A). The Pt-loaded InP photocathode performance was then measured under chopped illumination in an acidic electrolyte (figure 4.6B). Out of 11 devices tested under these conditions, the current density at 0 V vs. RHE was

recorded to be 15.2±2.0 mA/cm^2. The onset potential of ~0.6 V vs. RHE is in good agreement with the flat band potential measured through OCP and Mott-Schottky measurements. Quantitative gas product measurement was utilized to confirm that the origin of this photocurrent primarily stemmed from H_2 production. One metric used to quantify photocathode performance is the half-cell efficiency. The efficiency, depicted as η, was calculated through:

$$\eta = \frac{1.23 * (V\ vs.RHE) * I\ (mA/cm^2)}{P_{incident}} * 100\%$$

where $P_{incident}$ was 100 mW/cm^2. While the actual device efficiency will depend on the photoanode performance, among other variables, this metric is useful for comparing to photocathodes. The half-cell efficiency of our InP photocathode (figure 4.6B) of 4.0% is comparable to that of InP NWs grown on InP substrates, indicating that using low-cost Si growth substrates may be a promising avenue for further development of such photocathodes.[97] However, this half-cell efficiency was lower that record InP devices, indicating that there is room for further improvement.[151]

The InP photocathode's current voltage and stability curves were also tested in neutral and basic electrolytes. In neutral and basic electrolytes, the InP fill factor was not as high as that of the InP in acidic conditions, likely due to differences in surface catalysis kinetics. Chronoamerometric scans of the InP in all three conditions were tested through 11-hour chronoamerometric measurements. The photocurrent typically decayed to 50-70% of its initial value before stabilizing. Further improvements can be made by developing an improved further protection layer and catalyst adhesion.

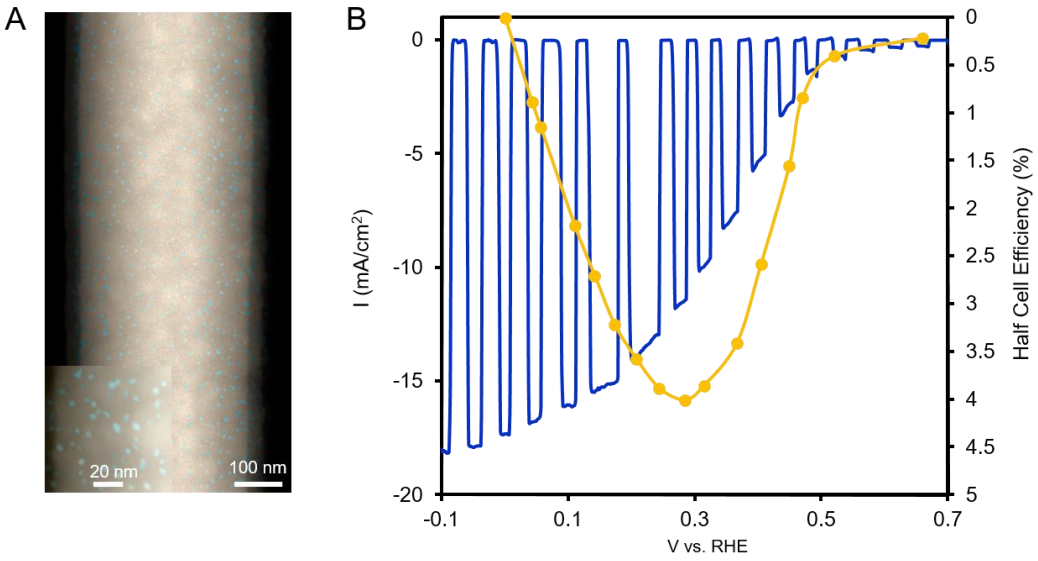

Figure 4.6. Pt nanoparticle co-catalysts were deposited *via* photodeposition. HAADF-STEM images reveal an average diameter of 6 nm (A). Current-voltage curve of InP photocathode indicates a maximum half-cell efficiency of 4%.

4.8 Overall Water Splitting

To explore the prospects for InP NWs as building blocks in integrated water splitting systems, we sought to combine the InP photocathode with a light absorbing photoanode to generate a proof of concept system. We chose bismuth vanadate ($BiVO_4$) as the photoanode component as recently it has been demonstrated to function efficiently in a half cell configuration. Furthermore, $BiVO_4$ can absorb photons with energies greater than 2.4 eV, rendering it promising to both spectrally match with low band gap semiconductor photocathodes and also attain a maximum photocurrent density of 7.5 mA/cm^2. This is not possible with high band gap photoanodes such as TiO_2.[93] We fabricated $BiVO_4$ photoanodes coated with a CoPi oxygen evolution catalyst according to a previously published procedure.[152,153]

Due to of the lack of stability of $BiVO_4$ in acidic conditions, the InP-$BiVO_4$ tandem was tested in neutral pH. In this experiment, a two optical path configuration was utilized as a result of the high degree of light scattering of the $BiVO_4$ electrode (Figure 4.7A). The half-cell photocurrent curves of InP and $BiVO_4$ electrodes under the same operating conditions are plotted in figure 4.7B. The crossover at ~0.85 mA/cm^2 indicates that this magnitude of unassisted water-splitting current should be attainable in a two electrode configuration. Indeed, under illumination the InP-$BiVO_4$ tandem system generates ~0.8 mA per 2 electrodes with an area of 1 cm^2 each, corresponding to a solar to hydrogen efficiency of ~0.5%. Aside from the continue development of the InP photocathodes, future work will include utilizing photoanodes with increased sub band gap transmission that will allow for one optical path to be used.[154]

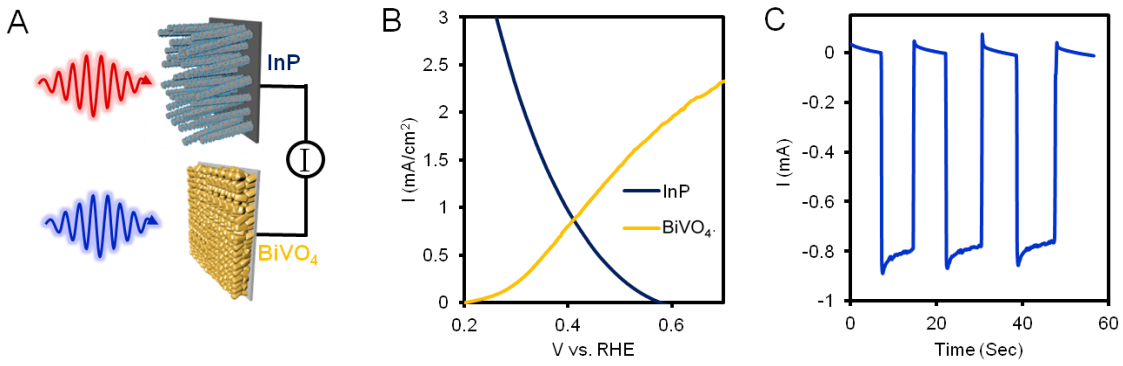

Figure 4.7. InP was combined with $BiVO_4$ in a tandem setup (A). The crossover in the current-voltage curves (B) is an estimate of the photocurrent generated from unassisted water splitting (C).

4.9 Concluding Remarks

In this section, we developed the growth and application of InP NWs as the light absorbing photocathode component of PEC cells. The growth of InP NWs was found to proceed *via* both, a self-seeded vertical growth and a radial epitaxial growth. This resulted in wurtzite phase InP NWs whose geometry can be rationally tuned over two orders of magnitude. Their integration on Si substrates renders them promising for potential scale up applications. To utilize the InP NWs as photocathodes, we doped them with Zn. The optimized NWs exhibit a 4.0% light to hydrogen efficiency in a half-cell configuration. When combined with a light absorbing photoanode in a tandem system, a 0.52% overall water splitting efficiency can be achieved. The present work represents the initial development the wurtzite InP NWs on silicon with many promising avenues to further improve.

5. Operando Spectroscopic Investigation of an Amorphous Cobalt Sulfide Hydrogen Evolution Electrocatalyst

5.0 Preface

In addition to my work with III-V materials as light absorbers, I studied reductive electrocatalysts as well. One catalyst that I chose to study was electrodeposited cobalt sulfide (CoSx). This particular material was developed two years prior to this work and was one of the best performing earth abundant materials in the literature. Beyond that, not much was known of this material. Hence, I decided to use the techniques available to me (electrochemistry, Raman spectroscopy, X-ray absorption spectroscopy) to elucidate some clues to the origin of high catalytic performance and perhaps derive important structure-function relationships of amorphous catalysts.

5.1 Introduction

Due to the intermittency of sunlight and temporal mismatch between maximum solar photon flux and peak power consumption, it is necessary to convert sunlight into an energy storage medium.[155] The production of H_2 via water electrolysis is a method of doing so that has attracted much attention, yet still faces numerous challenges.[5,156,157] One such limitation is the prohibitive cost of commonly used Pt hydrogen evolution reaction (HER) catalysts. Recently, a number of earth abundant HER catalysts have emerged in the form of amorphous transition metal chalcogenides that exhibit high catalytic activity, scalability, and low cost that renders them attractive candidates to replace Pt in water electrolyzer systems and photoelectrochemical cells.[158-164] However, these materials are poorly understood and the origins behind their remarkable catalytic efficiency remain elusive.

Despite the difficulty in characterizing these promising, yet not well understood catalysts, significant progress has been made over the last decade through the use of *operando* spectroscopic techniques. Investigations of amorphous HER and oxygen evolution reaction (OER) catalysts yield a common trend in which catalysts transform from a resting state to a catalytically active state which is quite different in terms of local atomic structure, oxidation state, or chemical composition. For example, an amorphous manganese oxide bi-functional OER and oxygen reduction reaction (ORR) catalyst was studied using X-ray absorption spectroscopy (XAS) and was shown to exist in three distinct atomic arrangements and average oxidation states, depending on the applied potential of the catalyst.[165] Moreover, electrodeposited amorphous molybdenum sulfide catalysts exhibiting significantly higher catalytic activities than bulk MoS_2 were examined with *in situ* X-ray photoelectron spectroscopy (XPS) and XAS.[166-168] The amorphous materials were found to be composed of a mixture of MoS_3 and MoO_x that formed a surface layer of MoS_2 with a high active site density under cathodic polarization that was believed to be responsible for the catalytic HER activity. Another study demonstrated that increases in the OER catalytic activity of amorphous Ni-Borate OER catalysts were accompanied by changes in Ni oxidation state and transformation into γ-NiOOH like molecular clusters.[169] These aforementioned works, in addition to multiple others, have yielded crucial structure-function relationships that are aiding both next generation catalyst design and understanding of fundamental chemistry.[170]

Within this context, we identified an amorphous cobalt sulfide (CoSx) HER catalyst recently developed in our lab as a worthwhile system to investigate its structure and function.[159] The CoSx HER catalyst requires only 83 mV overpotential to reach an operating current of 2 mA/cm^2 and is more active than many molybdenum sulfide catalysts, rendering it an intriguing, yet largely unknown system to study (Table S1). To perform such an analysis, we utilize a variety of spectroscopic tools to gain insight into the composition, local atomic structure, and catalytic activity of CoSx. In the following sections, we show through primarily Raman and X-ray absorption spectroscopies that CoSx exhibits a transient behavior, in which cobalt oxide and sulfide clusters spontaneously transform into CoS_2-like molecular domains with a high sulfur active site density under HER operating conditions. We stress that the XAS and Raman measurements are conducted in true *operando* conditions that are identical to those of the CoSx electrochemical testing.

5.2 Results and Discussion

The CoSx catalyst is synthesized through a simple electrodeposition procedure, in which a conductive substrate is cycled between negative and positive potentials in a precursor electrolyte solution (Figure 5.1a). Cobalt chloride and thiourea serve as cobalt and sulfur precursors, respectively, in a pH 7 aqueous phosphate buffered electrolyte. Beginning the cycle at -1.2 V *vs.* Ag/AgCl, the cyclic voltammogram (CV) initially shows an anodic peak at -0.5 V *vs.* Ag/AgCl, which is attributed to the oxidation of aqueous divalent cobalt ions.[171,172] When scanning in the negative direction, a cathodic peak arises and is likely due to the reduction and co-precipitation of cobalt and sulfur and formation of the CoSx film. Control experiments that performed the CV cycles in a phosphate buffer containing only thiourea showed neither anodic nor cathodic peaks while CV cycles in a phosphate buffer/cobalt chloride solution exhibited only the first anodic peak. The Raman spectra of the resulting electrodes revealed only the presence of thiourea, and cobalt oxide, respectively. The cathodic current at potentials more negative than -0.7 V *vs.* Ag/AgCl is attributed to the HER. As an increasing number of CV cycles is performed and consequently a thicker CoSx layer is deposited on the electrode, the HER current increases. This observation provides evidence for the electrodeposition of a porous CoSx film with HER active sites exposed not only at the surface but also throughout the film depth. If only the CoSx film surface was catalytically active, the HER current with each CV cycle would remain relatively constant or decrease from an increased CoSx film series resistance. Additional evidence for the porous nature of the film is provided by electrochemical double layer capacitance measurements. This measurement is conducted by recording capacitive current as a function of voltage sweep rate in a non-Faradaic potential region, which gives a first order approximation of the electrochemically active surface area[173,174]. The results of this measurement, shown in Figure 5.1b and 5.1c, indicate that the CoSx films from 5 and 15 electrodeposition cycles have roughness factors, defined as the ratio of electrochemically accessible surface area to projected surface area, of 8 and 23 relative to the bare FTO substrate on which the CoSx film is deposited. The as-deposited film shows a rough surface with cracks present throughout when observed using scanning electron microscopy (SEM) (Figure 5.1d). Energy dispersive spectroscopy (EDS) indicates that the film has a uniform Co:S ratio of 1.4:1.0. Macroscopically the CoSx has a shiny black appearance as shown in the inset of Figure 5.1d, for a CoSx film deposited on conductive fluorine-doped tin oxide (FTO) coated glass. A final annealing step under argon atmosphere at

300^0C is performed before measurements. X-ray diffraction (XRD) of the CoSx films presents no noticeable peaks other than those from the conductive substrate and only a broad background is observed.[159] Such an absence of diffraction peaks aside from those due to the substrate indicates the lack of significant long range crystalline order.

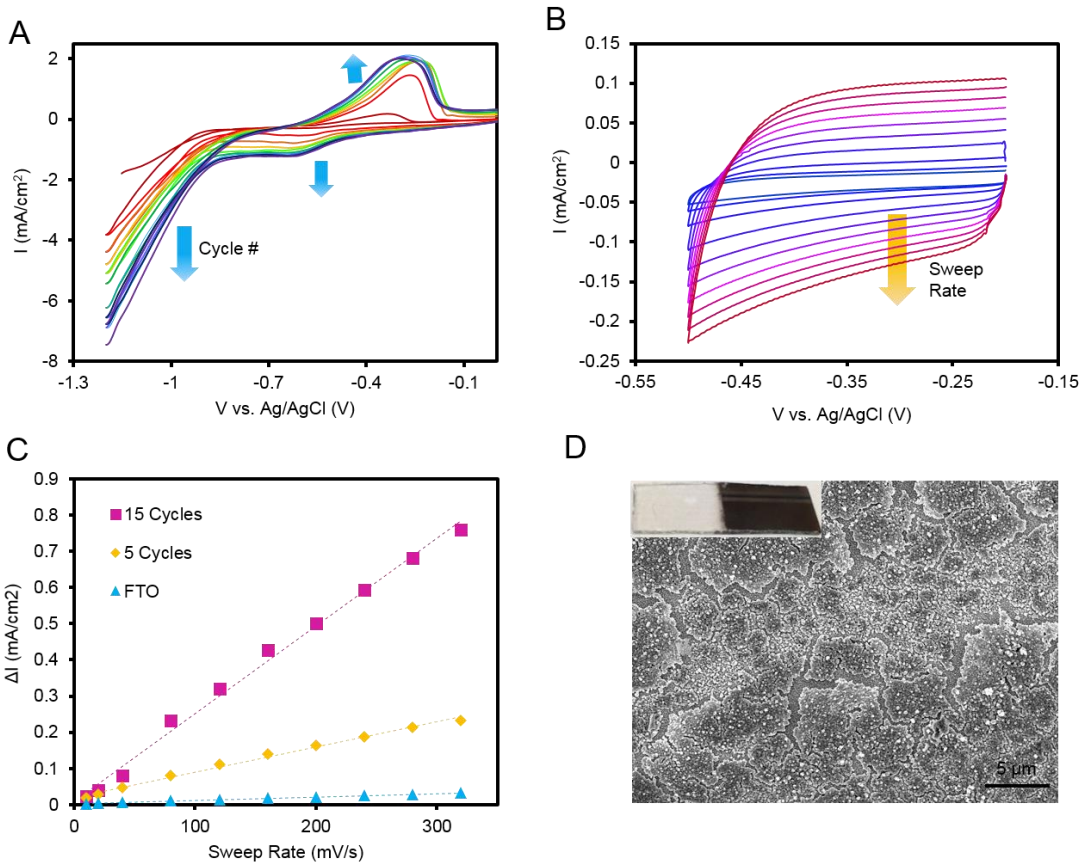

Figure 5.1. The CoSx catalyst is electrodeposited through a series of CV sweeps (A). A typical voltammogram shows an anodic peak at -0.3 V *vs*. Ag/AgCl, a cathodic peak at -0.5 V *vs*. Ag/AgCl, and a cathodic current at potentials more negative than -0.7 V *vs*. Ag/AgCl, which increases with increasing number of CV cycles. Electrochemical double layer capacitance (B,C) indicates that the CoSx film after 5 and 15 cycles of electrodeposition possesses a surface area of 8 and 23 times higher than the bare FTO substrate. An SEM image of the CoSx film (d) shows a rough, cracked surface. Optically, the film has a reflective black appearance (inset).

We next use Raman spectroscopy to obtain an initial picture of the as-made catalyst composition and structure. Raman spectroscopy has proved to be an invaluable tool in materials characterization.[175,176] This type of vibrational spectroscopy analyzes inelastically scattered light in which the energy lost is used to excite molecular vibrations that feature a change in polarizability. A representative Raman spectrum of the CoSx catalyst is presented in Figure 5.2.

Peaks at 682, 612, 518, 473, and 192 cm^{-1} are attributed to CoO or Co_3O_4 while the peak at 242 cm^{-1} is attributed to $Co(OH)_2$.[177-179] These peak positions are consistent with both the literature values and our own spectra on standard CoO, Co_3O_4 and $Co(OH)_2$ powders. The broad peak at 352 cm^{-1} cannot be matched to any standard nor to any well-characterized Co-S phase, yet lies in the wavenumber region where many transition metal sulfides exhibit Raman peaks and is tentatively attributed to a Co-S vibration. The oxide fraction in the CoSx likely forms upon exposure to air and its presence is not surprising, given that cobalt metal readily oxidizes in air and a porous, disordered film would likely have an even greater propensity to be at least partially oxidized. Depth-resolved x-ray photoelectron spectroscopy (XPS) indicates that an oxide is present through the entire thickness of the film, with the surface having similar chemical composition as the bulk. This is further evidence that the film is porous in nature, and a CoSx-air interface exists throughout the entire film thickness.

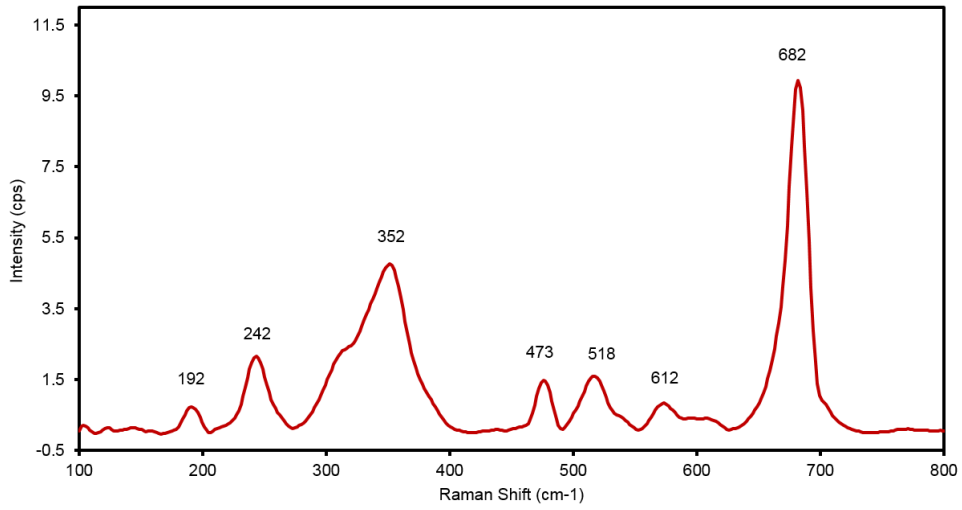

Figure 5.2. A typical Raman spectrum of the as-made CoSx film exhibits CoO/C_3O_4 and $Co(OH)_2$ peaks, as well as a broad peak at 352 cm^{-1}.

The electronic structure and local chemical environment of the CoSx film is probed with X-ray absorption near edge spectroscopy (XANES). For each XANES region, spectra of several standards are acquired and used as a basis for comparison. Cobalt K-edge XANES, which probes primarily the 1s-4p transitions, (Figure 5.3a) serves as a qualitative spectroscopic fingerprint to aid in identification of the cobalt species present in our film.[180-183] Cobalt oxides have an intense white line while cobalt sulfide has a much broader absorption edge, even though cobalt in these sulfides possesses the same oxidation state as CoO and $Co(OH)_2$. Qualitatively, the CoSx has a Co K-edge structure that resembles a mixture of an oxide and sulfide material. Co L-edge XANES offers a more quantitative determination of oxidation state, which is proportional to the area under the Co L_3 edge.[184-187] Analyzing the CoSx white line area after normalizing the pre and post edge to 0 and 1, respectively, reveals an average oxidation state of 2+ for the cobalt in CoSx (Figure 5.3b), consistent with previous XPS analysis[159].

Transition metal M-edge spectroscopy is an emerging materials characterization tool that utilizes extreme ultraviolet (XUV) photons to probe 3p-3d transitions.[188-191] The M-edge line

shape can reveal oxidation state, ligand field and spin state of the probed transition metal that arises from coulomb and exchange coupling between the 3d electrons and 3p core hole. We compared the static XUV absorption of CoSx, Co_3O_4 and CoS_2. Qualitatively, the CoSx spectra have features associated with both oxide and sulfides. The pre-edge feature at 58 eV and rising edge at 61 eV have previously been assigned to Co^{2+} ions.[190] The M-edge position in the CoSx spectrum suggests that the main oxidation state of cobalt is Co^{2+}, unlike Co_3O_4, which is a 1:2 mixture of Co^{2+} and Co^{3+} and has relatively more absorption features at higher energies.

The sulfur component in the CoSx films is next studied with S K-edge XANES. For sulfur compounds, the peak energy is proportional to sulfur oxidation state, which can range from 2471 eV for S^{2-} to 2483 for S^{6+}.[192-194] The S K-edge peak position for CoSx indicates that the sulfur has an average oxidation state of -1.5. Taken together, XANES analysis of CoSx Co K, Co L, Co M, and S K-edges presents a picture of a partially oxidized amorphous cobalt sulfide. The EDS Co:S ratio of 1.4:1.0 would have cobalt in excess for any of the main cobalt sulfide phases and it is likely that the excess Co is present in the form of an oxide.

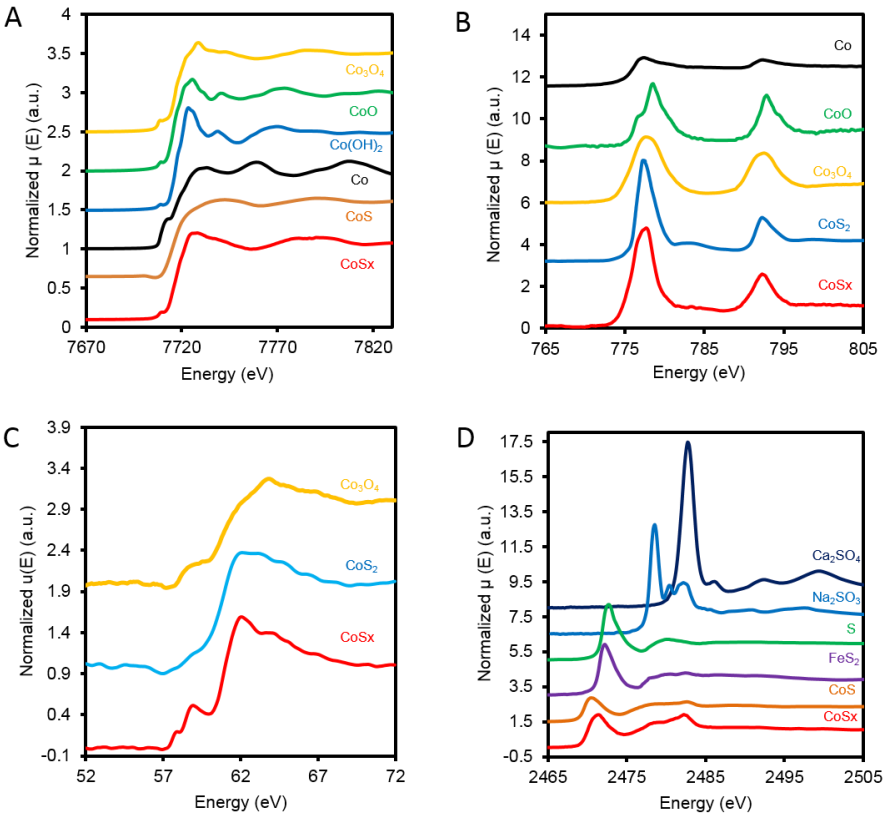

Figure 5.3. XANES characterization of CoSx. (A) Co K-edge spectra indicate both oxide and sulfide characteristics in the CoSx spectral lineshape. (B) The average oxidation state is confirmed to be Co^{2+} from L-edge analysis. (C) Co M-edge absorption spectroscopy further indicate oxide and sulfide character simultaneously present, (D) while the S is determined from S K-edge to be sulfide like with an average oxidation state of $S^{1.5-}$.

Ex-situ experiments yield valuable information on the chemical nature of CoSx yet the origin of high catalytic activity in this film remains largely unknown. To address this issue, analogous *opernado* experiments are performed on the same catalyst. Raman spectroscopy is first utilized as a spectroscopic means of observing any structural changes that may occur during HER reaction conditions. At open circuit conditions, the same spectral features as those on the as-made catalyst are observed (Figure 5.4a). As the CoSx electrode potential is systematically increased in the cathodic direction (more negative *vs*. the reversibly hydrogen electrode, (RHE)), new peaks in the Raman spectrum appear at 260 cm^{-1} and 370 cm^{-1}. The catalyst was held at the desired potential for 5 minutes before acquiring each spectrum to reach steady state conditions. The peaks previously attributed to CoO/Co_3O_4 disappear and the peak at 352 cm^{-1} remains constant. These changes initially become noticeable at +100 mV *vs*. RHE and seem to occur within the 5 minute timeframe after applying a cathodic potential. An initial explanation for the disappearance of the oxide is drawn from the cobalt-oxygen Pourbaix diagram, where at pH 7 the thermodynamically preferred state of cobalt transitions from Co^{2+} to metallic Co at a potential slightly positive of RHE[172]. As the potential of the electrode is shifted to more negative potentials, the two new peaks grow in intensity and dominate the Raman spectrum. These two peaks have the same Raman shift as the A_g and E_g modes of CoS_2, although their full width at half maximum intensity (FWHM) is 30 cm^{-1}, which is roughly twice that of crystalline CoS_2.[195-197] This line broadening is indicative of a disordered material or small cluster size.[198-200]

To the best of our knowledge, no experimentally or theoretically determined cobalt-sulfur Pourbaix diagram exists. However, one can draw analogy to the iron-sulfur Pourbaix diagram, where at pH 7 the FeS_2 pyrite phase becomes thermodynamically preferred at +300 mV *vs.* RHE.[201,202] The CoS_2 Raman signature observed in combination with previous electrochemical studies on analogous transition metal sulfide systems suggests that the CoSx is spontaneously transforming into CoS_2 like micro-domains under cathodic polarization. One observation of note is the blue-shift of the CoS_2-like Raman peaks with increasingly negative potential (Figure 5.4b). Potential-dependent Raman red-shifts are commonly observed in adsorbed molecules whose bonds are weakened or *vice versa* where bonds are being strengthened from an electrochemical process.[203-206] Changes in electronic density have also been attributed to potential-dependent Raman shifts.[207-209] The blue-shift in our case suggests the possible strengthening of Co-S bonds with increasingly negative potential. This CoS_2-like phase is stable only under reducing potentials and upon the return to open circuit, the Raman spectrum resembles that of cobalt hydroxide with the majority of the CoS_2 signal gone. This change is reversible for multiple cycles of switching between cathodic polarization and open circuit conditions (Figure 5.4c) though a small peak at 390 cm^{-1} remains 5 minutes after applying a negative potential, when the next spectrum at open circuit is taken.

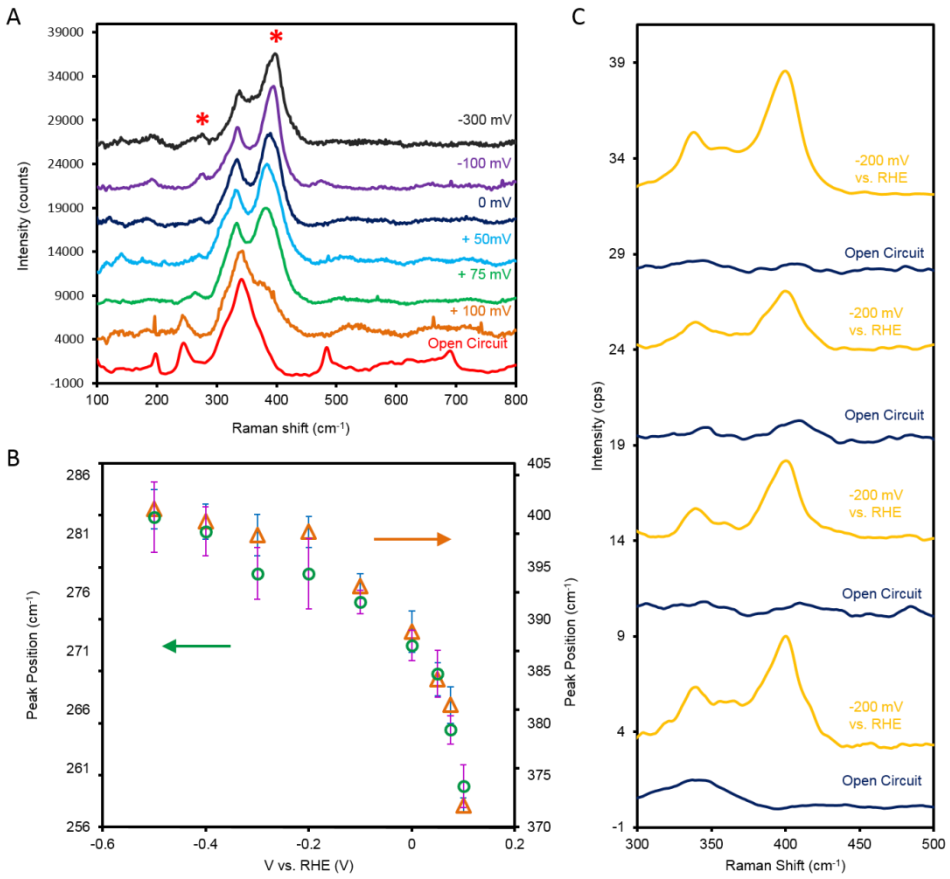

Figure 5.4. *Operando* Raman spectroscopy of CoSx. With increasingly negative potentials, two new peaks arise that are attributed to the formation of CoS_2-like domains (A). These peaks blue-shift with increasing negative potential (B), potentially indicative of bond-strengthening. Orange triangles represent the CoS_2 A_g-like peak and green circles represent the CoS_2 E_g-like peak. The CoS_2-like mode appearance is reversible and is maintained through multiple cycles (C). The bottom spectrum represents the 1st Raman spectrum of the CoSx film and the top represents the last.

Complementary *operando* X-ray absorption experiments are performed to more completely understand the structure of the CoSx catalyst during reaction conditions. From the dry sample to that immersed in electrolyte in open circuit conditions, there is minimal change in the near edge spectrum (Figure 5.5a), except for a slightly sharper white line characteristic of $Co(OH)_2$ (*vide supra*). However, under an applied potential of -150 mV vs. RHE, the Co K-edge white line dissapears and the spectrum resembles that of a transition metal sulfide.[180] The dissappearance of the oxide and formation of a cobalt sulfide species is consistent with the *operando* Raman data. The increase in intensity of the pre-edge peak, a dipole-forbidden 1s-3d transition, indicates increased p-d orbital mixing, which can be explained by an increased p-d hybridization in cobalt

sulfides relative to oxides.[210-212] Linear combination fitting of XANES data using the spectra of reference compounds is performed to obtain a first order approximation of the CoSx catalyst under dry and HER conditions. Through linear combination fitting, the best fits yeilded a composition of 60% CoO and 40% CoS in the dry state and 26% CoO and 74% CoS under HER conditions. *Opernado* Co L-edge XANES reveals that the oxidation state remains at +2, but features a satellite peak increase that is also attributed to p-d hybridization.[180,213-215] Likewise, the S K-edge spectrum remains consistent from open circuit conditions to reducing potentials, indicating that the sulfur has a similar oxidation state throughout the process and the overall change to CoS_2 microdomains affects the Co K-edge more than the S K-edge.

XANES data is an important tool for oxidation state analysis and qualitative spectroscopic fingerprint comparison, yet quantitative information about the immediate chemical surroundings of the investigated element is difficult to extract due to multiple scattering processes and bound to bound transitions. To this end, we utilize extended X-ray absorption fine structure (EXAFS) analysis to obtain such information. In essence, the EXAFS phenomenon is the modulation of the X-ray absorption coefficient of the absorbing atom due to constructive or destructive interference of the forward propagating and backscattered waves of the ejected photoelectron due to scattering by neighboring atoms.[216-218] By analyzing the fine structure of the X-ray absorption spectrum, quantitative information about coordination number, coordination atoms, bond lengths, and structural disorder can be obtained. We analyze the EXAFS spectra for two samples: an as-made CoSx film and the same CoSx film operating at reaction conditions at -150 mV *vs*. RHE. The Fourier transform EXAFS spectra for CoSx are plotted in R-space in Figure 5.5b. A qualitative assessment of the two spectra reveals two main differences between the as-made and *operando* samples. 1) Upon cathodic polarization, the average bond length increases slightly and 2) the second shell contribution decreases significantly. Co-S bonds are typically ~12% longer than Co-O bonds and the increase in average bond length points to an increase in the fraction of Co-S bonds in the CoSx film. Compared to CoO,[219] the dry CoSx film has significantly weaker features beyond the first shell and these features further decrease in intensity under HER catalytic conditions, indicative of Co-S clusters that are mainly comprised of Co surrounded by a single shell of S with little ordering beyond this first shell. Since the dry film is partially oxidized and likely more ordered, we see an increased amplitude in the 2nd and 3rd shells in the EXAFS data.

Quantitative analysis is performed by modeling the EXAFS spectra. Due to experimental evidence for the presence of CoO and CoS_2 as the main cobalt species present (*vide supra*), these two structures were used as initial models to fit the CoSx experimental EXAFS data. CoO and CoS_2 both have Co surrounded by octahedral O and S, respectively. Complete fitting parameters and results can be found in the supporting information. A best fit of the dry CoSx film yields a combination of octahedral Co atom that has on average 2.1 O atoms and 2.1 S atoms in the first shell. Second shell scattering paths with a coordination number approximately half that of bulk CoO and CoS_2 are fit to the data. The second shell paths give evidence for a slight phase segregation of cobalt oxide and sulfide into these sub-nanometer clusters as opposed to a homogeneous cobalt oxysulfide material. Data modeling utilizing only one crystal structure (CoO, Co_3O_4, Co_9S_8, or CoS_2) did not yield a reasonable fit.

A best fit for the *operando* CoSx film features the Co surrounded by 5.2 S atoms and 0.8 O atoms, which serves as further confirmation of the *operando* oxide-sulfide transformation. Second shell Co-S scattering paths have minimal contributions to the EXAFS fit likely due to the material disorder or relatively poor scattering ability of sulfur, while Co-Co scattering

contributions in the 2nd shell are fit to give a coordination of ~3, suggesting that the *operando* CoSx film consists of few-nuclei CoS_2 clusters.

Completely omitting the oxide fraction from the model results in a significantly poorer fit, suggesting that the there is a small oxide fraction remaining within the film, even under HER operating conditions. This oxide fraction may not be in electrical contact with the conductive substrate and therefore does not transform into CoS_2-like clusters. However, after electrolysis for 3 hours, the Co:S ratio, as measured by EDS, decreases from 1.4:1 to 0.98:1, indicating that a fraction of the cobalt dissolves into the electrolyte. This is consistent with the formation of CoS_2-like clusters under HER operating conditions since the sulfur content would be the stoichiometrically limiting reagent and some of the remaining cobalt is likely to dissolve away.

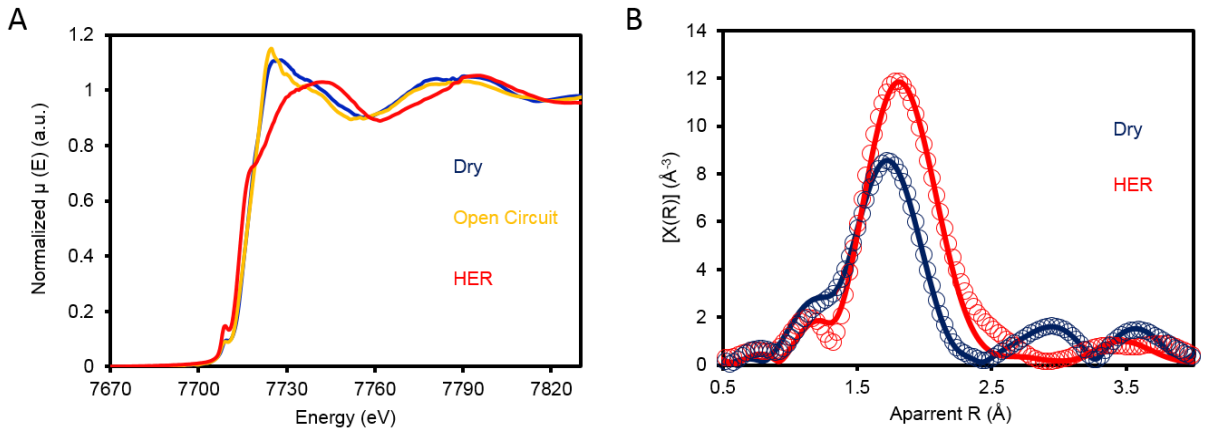

Figure 5.5. *Operando* Co K-edge XANES (A) reveals a lineshape change that suggests transformation from cobalt oxide to cobalt sulfide. EXAFS (B) qualitatively indicates an increased average bond length and decrease in decreased 2nd shell contributions. Open circles represent the experimental data and solid lines represent the fit.

From a comprehensive data set utilizing information from Raman, XANES, and EXAFS, an atomic structural model of the *operando* state of CoSx emerges (Figure 5.6). Immediately noticable are the undercoordinated sulfur atoms on the perimeter of the CoSx cluster. *Opernado* XANES determines the sulfur species to be sulfide-like even at open circuit conditions; therefore, their oxidation to sulfates upon exposure to electrolyte is not likely. *Operando* Raman measurements indicate the presence of a disordered CoS_2-like molecular cluster state. This state is confirmed through XANES and EXAFS as being the predominant form of cobalt. EXAFS analysis reveals a near complete octahedral shell of S around the central Co and partial 2nd shell contribution of 3 additional Co atoms yeilding the best fit, giving a cluster size of several cobalt nuclei. A small molecular CoS_2-like clusters is rendered in Figure 5.6. Additional renditions of the structural model are presented in the supporting information.

Transition and precious metal disulfides such as MoS_2, CoS_2, and RuS_2 were well-studied hydrodesulfurization (HDS) catalysts before drawing attention for their HER catalytic functionality.[220-226] For MoS_2, edge sites featuring undercoordinated S atoms were ascertained to be the primary HDS active sites and in recent years, the same sites were determined to also be the active sites for the HER reactions.[227] From the onset of this discovery, many efforts have

been put forth to engineer MoS_2 catalysts to feature an abundance of active sites and have resulted in significant improvements of MoS_2 catalytic efficiencies.[228-231]

It is plausible that disulfide anions (S_2^{2-}) play a similar role in the HER reaction on CoS_2 surfaces and initial reports have suggested likewise. Transition metal chalcogenides and crystalline pyrite materials, especially CoS_2, have been previously demonstrated to be highly active HER catalysts. [232-235] The density of exposed sulfide atoms, presumibly the active sites for the HER, on a microscopic level has been linked to the catalysts' performance. Within this context, the *operando* CoSx atomic model is an ideal structure for a CoS_2 based catalyst, because a significant fraction of S atoms are accessible for catalysis. The high catalytic activity observed for these amorphous films relative to crystalline CoS_2 might be explained by this high density of exposed active sites and possible electronic differences between these molecular clusters and the bulk pyrite structure, which warrants further study.

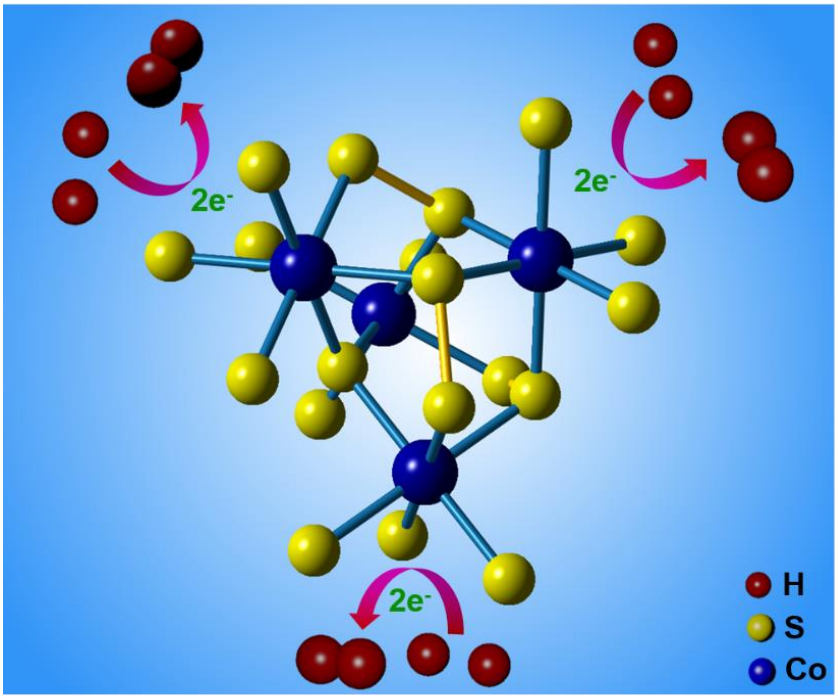

Figure 5.6 Atomic model of CoSx catalyst derived from Raman, XANES and EXAFS data.

5.3 Concluding Remarks

In summary, a highly active CoSx catalyst is investigated through an *operando* spectroscopic approach. Through a combination of Raman and XAS experiments, we find that the as-made CoSx consists of a porous amorphous film comprised of small oxide and sulfide clusters. Upon the application of cathodic polarization, the CoSx catalyst transforms into CoS_2-like molecular clusters. We speculate that the origins of high HER activity lie in the presence of a high density

of accessible sulfur atoms along the cluster periphery, which might exhibit different binding strength relative to the active sites in bulk CoS_2.

Parts of this section were published in: “Operando Spectroscopic Analysis of an Amorphous Cobalt Sulfide Electrocatalyst” **N. Kornienko**, J. Resasco, N. Becknell, C. Jiang, Y. Liu, K. Nie, X. Sun, J. Guo, S. Leone, P. Yang, *J. Am. Chem. Soc.*, 137, 7448 (2015)

6. Visible-Light Photoredox Catalysis: Selective Reduction of Carbon Dioxide to Carbon Monoxide by a Nickel *N*-Heterocyclic Carbene–Isoquinoline Complex

6.0 Preface

In the field of solar to fuel conversion, one of the most attractive yet difficult directions is the conversion of CO_2 to fuels. The desirability of CO_2 reduction is that hydrocarbons can be generated as chemical feedstock or fuels that are more readily integrated with current infrastructure. The challenge comes from the fact that this is a kinetically sluggish reaction and competition with hydrogen generation as well as the possibility of generating multiple CO_2 derived products renders catalytic selectivity difficult to achieve.

In this section, I teamed up with a collaborator from the Christopher J Chang group to examine a series of molecular catalysts for CO_2 reduction. We chose molecular catalysts because they offer precise tunability that may help overcome the various challenges of CO_2 reduction. We also utilized acetonitrile as the solvent due to its higher CO_2 solubility and to eliminate the competition with hydrogen generation. This allowed us to focus on structure-function relationships of our catalysts. In the final section, we combined the best performing catalyst with a soluble light absorber to demonstrate light driven CO_2 reduction with the help of a sacrificial electron donor.

This work was important to establish a series of non-aqueous CO_2 reduction catalysts. Next steps will serve to perform the CO_2 reduction in aqueous solvents, utilizing, in part, lessons learned in this work.

6.1 Introduction

The search for sustainable resources has attracted broad interest in the potential use of carbon dioxide as a feedstock for fuels and fine chemicals.[236-245] In this context, the photocatalytic reduction of CO_2 is an attractive route that can take advantage of the renewable and abundant energy of the sun for long-term CO_2 utilization,[10,246,247] with the eventual target of coupling the reductive half-reaction of CO_2 fixation with a matched oxidative half-reaction such as water oxidation to achieve a carbon-neutral artificial photosynthesis cycle.[5,248-254] Before this ultimate goal can be realized, however, a host of basic scientific challenges must be addressed, including developing systems that balance selectivity, efficiency, and cost. With regard to selectivity, it is critical to minimize the competitive reduction of water to hydrogen that is typically kinetically favored over CO_2 reduction, as well as selectively convert CO_2 to one carbon product.[255,256] Another primary consideration is the use of visible-light excitation, which more effectively harvests the solar spectrum and avoids deleterious high-energy photochemical pathways. Semiconductors such as TiO_2 and SiC have been widely employed as heterogeneous catalysts for photochemical and photoelectrochemical conversion of CO_2 to a variety of carbon products such as carbon monoxide, methanol, and methane. However, examples of selective light-driven CO_2 conversion to reduced carbon products in heterogeneous systems are limited mainly to these wide-band gap, UV absorbing materials that do not exhibit selectivity toward a single carbon product,[257-260] aside from select transition-metal doped silicates.[261-263] The use of semiconductors with molecular electrocatalysts has also been investigated for

photoelectrochemical CO_2 conversion,[264-266] and recent work in improved inorganic materials for electrocatalytic CO_2 reduction continues to emerge,[267-273] but limited photocatalytic applications have been reported. Homogeneous molecular systems offer an alternative strategy for solar CO_2 fixation that allows for modular tuning of their performances via synthetic chemistry. However, most CO_2 reduction efforts in this context have focused on electrocatalysts, including those based on cobalt and nickel polyamine macrocycles,[274-280] second- and third-row transition metal polypyridines,[243,281-289] metal porphyrins[290-293] and phthalocyanines,[294,295] metal phosphines,[296-299] and thiolates,[300] metal clusters,[301] pyridine and amine derivatives,[302-305] and N-heterocyclic carbene−pyridine platforms.[306]

To date, no one synthetic system combines visible-light excitation and earth-abundant metal catalysts to achieve sustainable, solar CO_2 conversion to a predominant product with high selectivity and activity. For example, photochemical reductions of CO_2 with selective product formation using rhenium polypyridine catalysts have been extensively investigated, but these third-row transition metal photosensitizers absorb largely in the UV region and do not utilize the full solar spectrum.[307,308] UV-excitable organic photosensitizers, such as p-terphenyl[279,309,310] and phenazine,[311] have also been used for photochemical CO_2 fixation. Visible-light photocatalytic CO_2 reduction has been largely limited to noble-metal catalysts that achieve low turnover numbers and/or selectivity. For instance, $[Ru(bpy)3]^{2+}$ can be used as both a photosensitizer and a catalyst for reducing CO_2 to formate with turnover numbers (TONs) reaching up to 27 within 24 h.[312] Related systems with $[Ru(bpy)3]^{2+}$ as a photosensitizer and $Re(bpy)(CO)_3Cl$ have reported TONs reaching up to 48 in 4 h for selective CO production. First-row transition metal complexes have also been used in conjunction with $[Ru(bpy)3]^{2+}$; early work on nickel N4- macrocycles and $[Ru(bpy)3]^{2+}$ have been demonstrated to approach TONs of 0.1 for CO production, but with concomitant H_2 production with TONs up to 0.7.[313,314] Such undesirable proton reduction pathways are also observed in cobalt-based systems with $[Ru(bpy)3]^{2+}$, where CO/H_2 ratios typically range between 0 to 3, with optimized CO/H_2 ratios of up to 19 resulting in markedly lower overall CO and H_2 production.[315,316] Multinuclear bipyridine-based Ru−Re[317,318] and Ru−Ru[319] complexes can also reduce CO_2 to CO and formic acid, respectively. More recently, a series of Ir(tpy)(R-ppy)Cl complexes (where tpy = terpyridine, ppy = phenylpyridine, R = H, Me) that absorb visible light have been reported to reduce CO_2 to CO photocatalytically with TONs of up to 50 within 5 h.[320] Moreover, in the aforementioned cases, high-power 500− 1000 W Xe or Xe−Hg lamps are typically necessary to achieve the reported turnover numbers, noting that values for power per area are not noted. Since the average solar intensity is measured to be around 136.6 $mW \cdot cm^{-2}$,[321,322] low-intensity light would be advantageous for more practical application of these technologies.

Against this backdrop, we have initiated a program aimed at developing visible-light photoredox systems using earth-abundant catalysts for the selective conversion of CO_2 to value-added products. Inspired by the seminal $[Ni(cyclam)]^{2+}$ complex (where cyclam = 1,4,8,11-tetraazacyclotetradecane) and related systems that exhibit high selectivity for reducing CO_2 over H_2O,[323] and the rapid emergence of visible-light photoredox catalysis for organic transformations,[324-329] we sought to couple visible-light photosensitizers of appropriate reducing power with first-row transition metal catalysts to drive CO_2 fixation chemistry at earth-abundant metal centers. We now report the synthesis, properties, and evaluation of a new family of nickel complexes supported by N-heterocyclic carbene−amine ligands that can perform both electrocatalytic and photocatalytic carbon dioxide reduction with high selectivity over proton reduction. Through systematic substitutions on the ancillary donors, we have discovered a nickel

N-heterocyclic carbene−isoquinoline platform that achieves visible-light catalytic photoredox conversion of CO_2 selectively to CO with no detectable formation of hydrogen from off-pathway proton reduction processes. Using a relatively low-power 150 W Xe lamp that corresponds to 130 mW·cm^{-2} under our experimental conditions, we achieve TONs and turnover frequencies (TOFs) approaching 98,000 and 3.9 s^{-1}, respectively. Further experiments reveal that the catalytic activity in this photoredox cycle is limited by either the formation of the active nickel catalyst or the chemical conversion of CO_2 to CO, providing a path forward for future designs of carbon-neutral solar-to-fuel conversion processes based on this strategy.

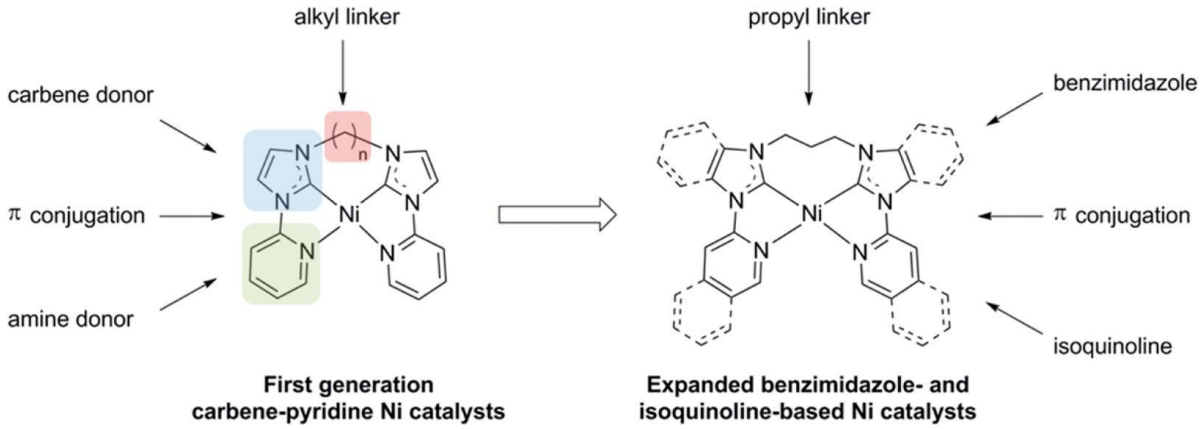

Scheme 6.1: Ligand Design Strategy for Developing Nickel Carbene−Amine Catalysts for CO_2 Reduction

6.2 Synthesis and Characterization of a Homologous Family of Nickel N-Heterocyclic Carbene−Amine Complexes Bearing Benzimidazole-Based Carbene Donors or Isoquinoline Amine Donors

On the basis of the precedents with [Ni(cyclam)]$^{2+}$ and related N4 macrocyclic systems that exhibit high selectivity for reducing CO_2 over H_2O under electrocatalytic conditions, we reasoned that developing new planar, electron-rich platforms with a dz^2 - based nucleophile would provide a good starting point for investigation. To this end, we previously communicated a trio of nickel complexes supported by N-heterocyclic carbene−pyridine ligands that demonstrated adjustments in the length of the bridgehead tether to offer tunability of cathodic reduction potentials. Although these first-generation systems are capable of highly selective electrochemical reduction of CO_2 over H_2O, they are limited by their modest catalytic activity and long-term stability. To address these shortcomings, we designed and synthesized a new family of nickel catalysts with systematic changes at the N-heterocyclic carbene and amine donors (Scheme 6.1). Using the modular synthetic approach outlined in Scheme 6.2, building blocks 1a−3a were synthesized by a palladium- or copper-catalyzed carbon− nitrogen coupling of an imidazole or benzimidazole precursor and a halogenated pyridine or isoquinoline.[330]

The respective bis-N-heterocyclic carbene−amine ligands 1b−3b can be readily prepared by alkylation of 1a−3a with the appropriate dihalide linker. For example, alkylation of 1a by dibromopropane, followed by an anion exchange with NH_4PF_6, afforded ligand 1b. In addition,

the effects of conjugation on CO_2 reduction can be interrogated by the synthesis and characterization of bis(2-(benzimidazolylmethyl)pyridinyl)propane hexafluorophosphate (4b), which contains extra methylene groups that break the π system between the N-heterocyclic carbene and the pyridine donors. Deprotonation of the ligands by Ag_2O followed by metalation with $Ni(DME)Cl_2$ yielded the chloridebound nickel complexes, which were then treated with $NaPF_6$ to afford the final catalysts 1c−4c in near-quantitative yield. As expected, all four complexes are diamagnetic as shown by 1 H and 13C NMR measurements. The solid state structures of 1c−4c determined from singlecrystal X-ray crystallography are shown in Figure 6.1. In line with our previous work on tuning alkyl linkers in the Ni(Rbimpy) series, the propyl bridge allows a great degree of flexibility, and the four-coordinate nickel centers in all four complexes display distorted square-planar geometries. This distortion is quantified by measuring the torsion angle formed by N-amine− Ni−N-amine−Cortho in the complexes, and these angles range from 24.7° to 57.2 (Figure 6.1). The Ni−N and Ni−C bond lengths are within the typical range for these types of donors.[331-333]

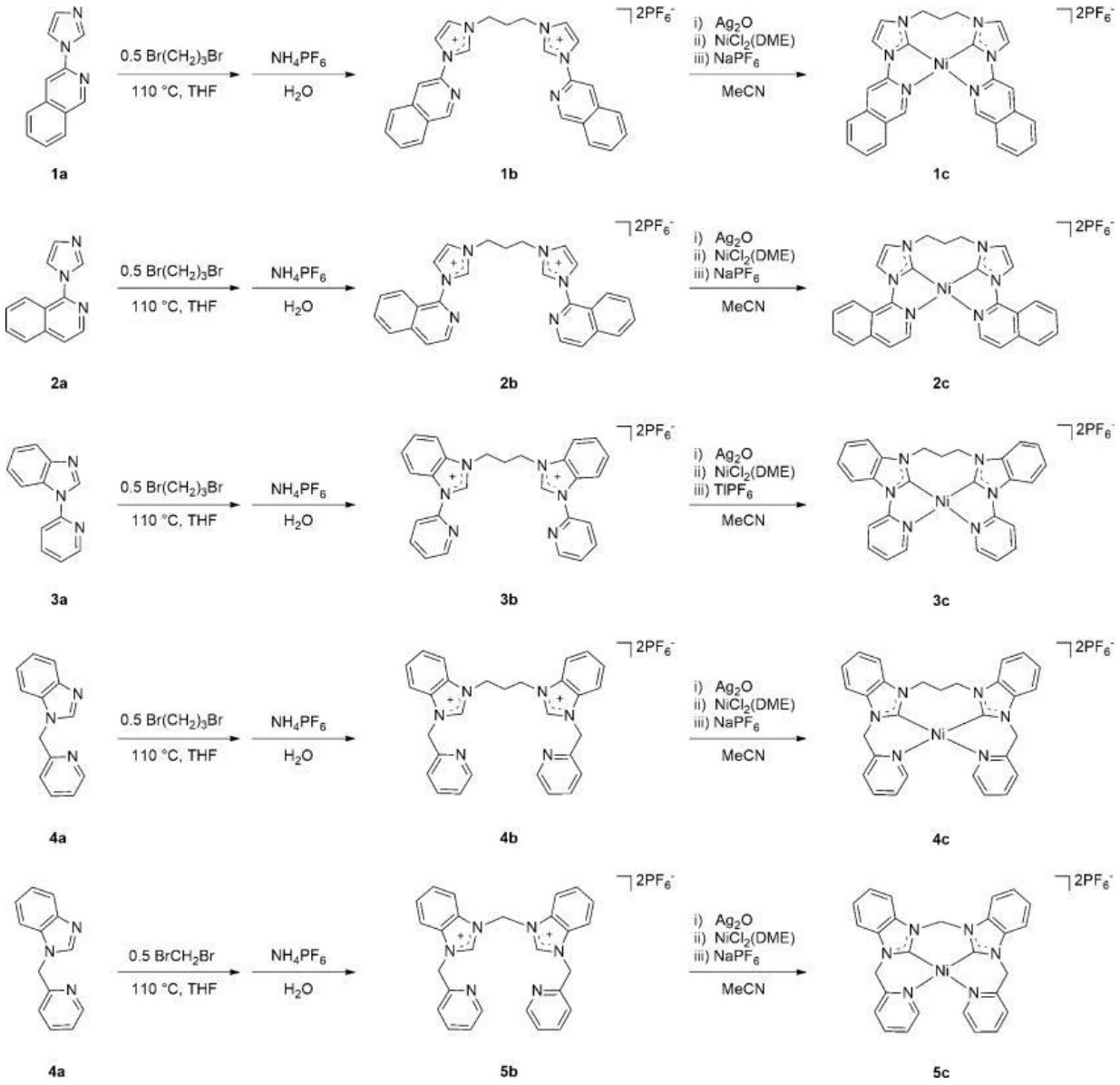

Scheme 6.2. Synthesis of N-Heterocyclic Carbene−Amine Ligands 1b−5b and Their Ni Complexes 1c−5c

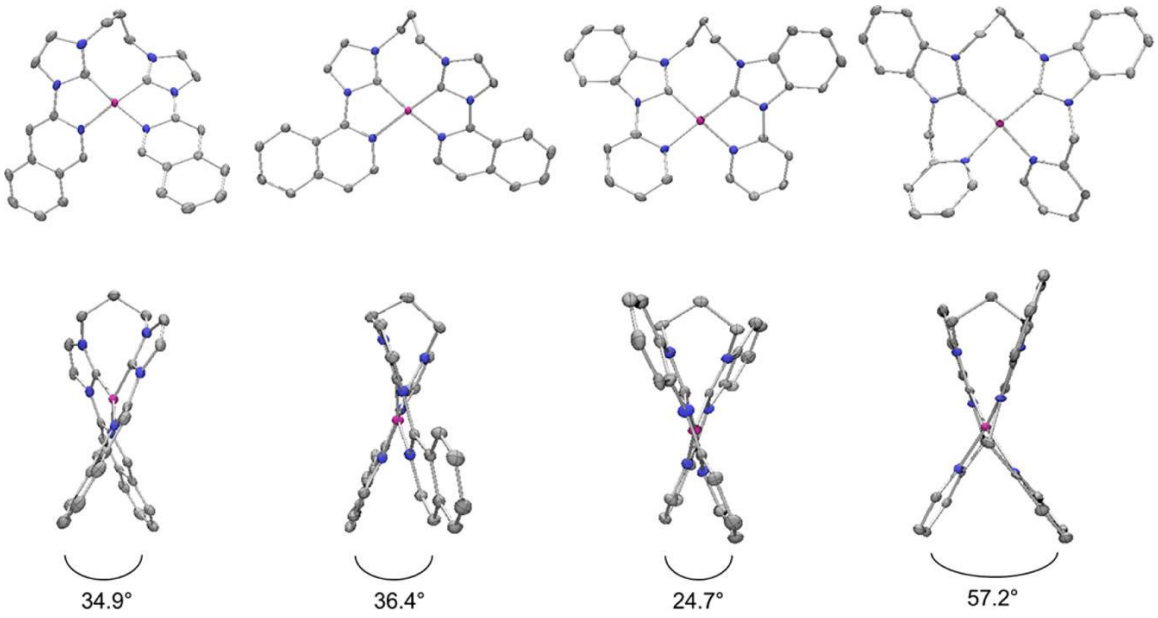

Figure 6.1. Solid-state structures of 1c−4c (left to right). The top row shows a front view; the bottom row provides a side view, highlighting the torsional twist induced by ligand flexibility. Anions, solvent molecules, and hydrogen atoms are omitted for clarity; thermal ellipsoids are shown at 50% probability

6.3 Evaluation of Nickel N-Heterocyclic Carbene−Amine Complexes for Electrocatalytic CO2 Reduction.

The electrochemical behaviors of complexes 1c−4c were interrogated by cyclic voltammetry. First, the electronic effects of the extended conjugation on the carbene and amine donors of the ligand scaffold were examined (e.g., isoquinoline for pyridine, benzimidazole for imidazole). The cyclic voltammogram of an acetonitrile solution of quinoline-based 1c and 0.1 M NBu_4PF_6 electrolyte exhibits two reversible reductions at $E_{1/2} = -0.92$ and −1.38 V vs SCE under a nitrogen atmosphere (Figure 6.2a). For comparison, the cyclic voltammogram of quinoline-based 2c, in which the N-heterocyclic carbene is substituted at the 1-position of the isoquinoline ligand, displays two reversible reductive processes at $E_{1/2} = -0.74$ V, −1.20 V and an irreversible process at $E_{pc} = -1.60$ V under N_2 (Figure 6.2b). Under a CO_2 atmosphere, the cyclic voltammograms of both complexes 1c and 2c show enhanced current at Eonset = −1.20 and −1.40 V, respectively, which is indicative of electrocatalysis. Notably, catalyst 1c represents a marked improvement in overpotential compared to the parent complex $[Ni(Prbimpy)](PF_6)_2$, which exhibits a cathodic catalytic current for reducing CO_2 at $E_{onset} = -1.40$ V. In contrast to what is observed for complexes 1c and 2c where the conjugation is extended by using an isoquinoline donor, extending the conjugation on the imidazole-based N-heterocyclic carbene donor with a benzimidazole carbene shifts the onset reduction potential for CO_2 reduction to more negative values. Indeed, the cyclic voltammogram of 3c features two reversible reductions at $E_{1/2} = -0.63$ and −1.22 V vs SCE (Figure 6.2c) under a nitrogen atmosphere and enhanced current at $E_{onset} = -1.47$ V under a CO_2 atmosphere.

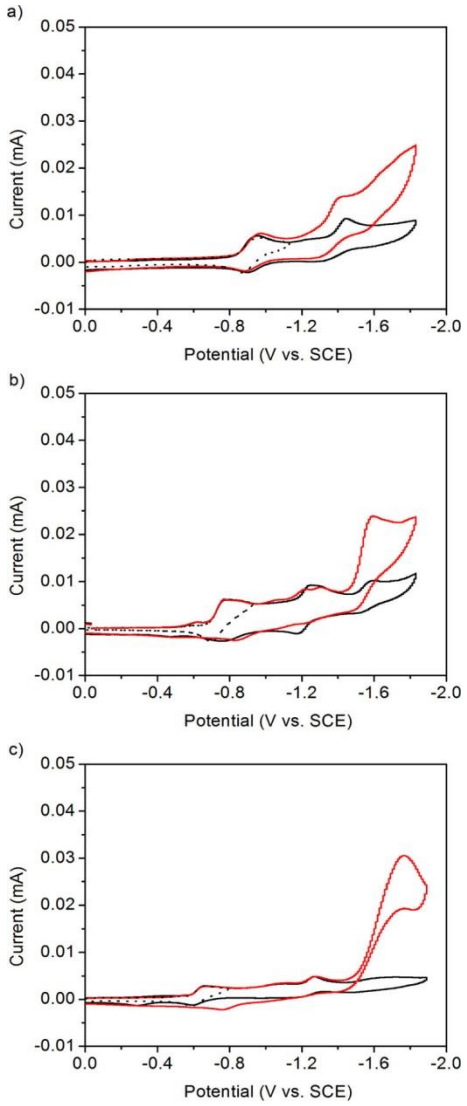

Figure 6.2. Cyclic voltammograms of complexes (a) 1c, (b) 2c, and (c) 3c in a 0.1 M NBu4PF6 acetonitrile solution under a N2 (black) and CO2 (red) atmosphere using a glassy carbon disk electrode at a scan rate of 100 $mV \cdot s^{-1}$.

Breaking the conjugation between the N-heterocyclic carbene and the amine donors also shifts the onset potential of CO_2 reduction to more negative values. For example, the cyclic voltammogram of 4c displays two irreversible processes at $E_{pc} = -1.10$ and -1.43 V under N_2 with only a slight current enhancement at $E_{onset} = -1.45$ V under CO_2 (Figure 6.3a). As a result of the larger chelate ring size around the Ni center, the steric strain in 4c is expected to be higher than in the case of 3c. Indeed, this strain is reflected in the differences in the torsion angles along NPy−Ni−NPy−Cortho core between 3c and 4c; the extra methylene groups between the pyridine and carbene cause the observed torsion angle in 4c (57.2°) to be much larger than that of 3c (24.7°). We further probed the extent of these strain effects on CO_2 reduction by evaluating an analogous nickel N-heterocyclic carbene−pyridine complex previously synthesized by Chen and

co-workers (5c), which contains a methylene bridge between the N-heterocyclic carbenes in place of the propyl linker in 4c. This small change leads to a decreased torsion angle of 45.1° along NPy−Ni−NPy−Cortho core. As anticipated, the cyclic voltammogram of 5c shows two irreversible reductions at $E_{pc} = -1.02$ and −1.56 V under an N_2 atmosphere with only a modest current enhancement at $E_{onset} = -1.50$ V upon addition of CO_2 (Figure 6.3b). Both 4c and 5c are significantly less active than 1c−3c toward CO_2 reduction, suggesting that the extended conjugation at the appropriate location on the ligand platform is favorable for catalytic CO_2 reduction.

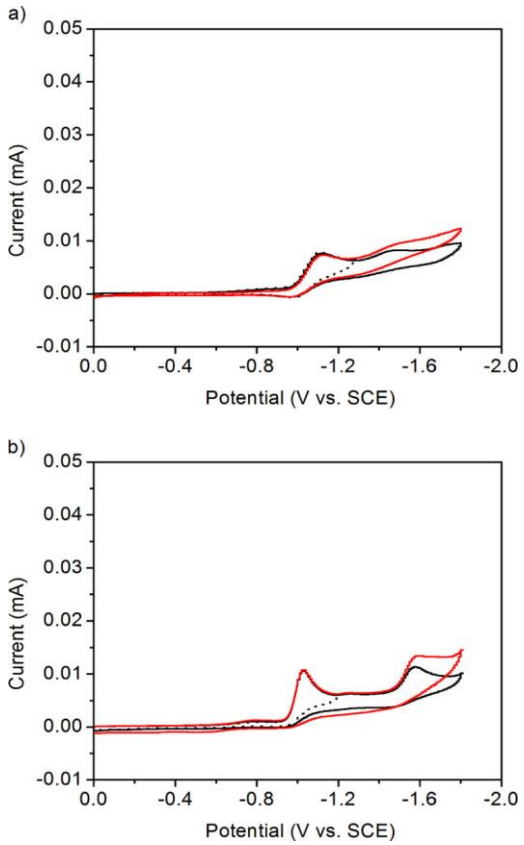

Figure 6.3. Cyclic voltammograms of complex (a) 4c and (b) 5c in a 0.1 M NBu_4PF_6 acetonitrile solution under a N_2 (black) and CO_2 atmosphere (red) using a glassy carbon disk electrode at a scan rate of 100 $mV \cdot s^{-1}$.

By systematically tuning the location and type of ligand conjugation in this series of nickel complexes, catalyst 1c is determined to have the lowest overpotential for CO_2 reduction potential at $E_{onset} = -1.20$ V. Controlled-potential electrolysis of an acetonitrile solution of 0.02 mM of 1c in the presence of 0.1 M NBu_4PF_6 at $E_{cat} = -1.80$ V vs SCE was conducted over an 8h period. The headspace was analyzed by gas chromatography in 30-min intervals and CO was detected as the major gas product (Figure 6.4), along with trace amounts of CH_4. The Faradaic efficiency (FE) for CO production is 90% with no detectable formation of hydrogen within the first 30 min. A total turnover number (TON) of 35 and an end point FE of 22% are calculated for CO production at 8h. No other gas or solution products are detected through GC or NMR

analysis. We speculate that the decrease in FE from 90% within the first 30 min to 22% at 8 h may be attributed to the re-oxidation of CO_2-reduced products at the counter electrode as they accumulate in the reactor; in this case, we anticipate that FE could be improved through reduced mass transfer of CO_2- reduced products between the working electrode and counter electrode compartments. Indeed, this mass transfer issue is solved through the use of a photoredox cycle with an external quencher, which achieves much higher activity, selectivity, and long-term stability.

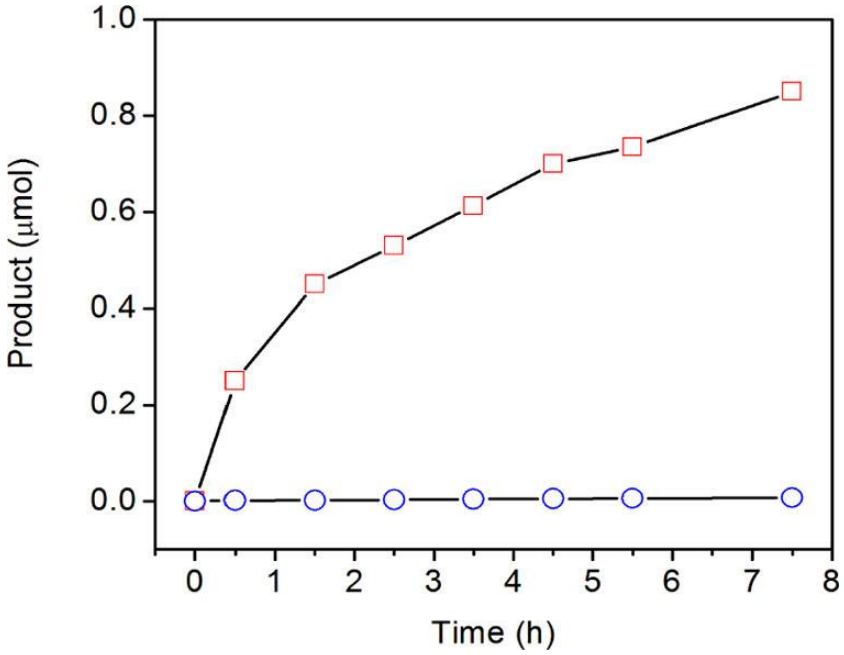

Figure 6.4. CO (red squares) and CH4 (blue circles) formation vs. electrolysis time in a controlled potential electrolysis in a 0.1 M NBu4PF6 acetonitrile solution containing 2 μM 1c at −1.8 V vs SCE using a glassy carbon disk electrode under a CO_2 atmosphere.

6.4 Development a Solar-Driven Photoredox Cycle for Catalytic CO_2 Reduction with Nickel N-Heterocyclic Carbene−Isoquinoline Complex 1c

With electrochemical data showing that improvements in overpotential, we moved to incorporate molecular catalyst 1c into a solar-driven photoredox cycle for CO_2 reduction. Specifically, we sought to combine this earth-abundant CO_2 catalyst with an appropriate light absorber that could subsequently transfer a high-energy electron to the nickel center. An iridium photosensitizer supported by fac-tris(phenylpyridine), $Ir(ppy)_3$, was selected owing to its ability to absorb solar photons in the visible region and potentially large driving force for the subsequent reduction of the nickel catalyst.[334,335]

A series of experiments were conducted to test the viability of using catalyst 1c combined with the visible-light absorber $Ir(ppy)_3$ and a sacrificial reductant, triethylamine (TEA), in a photoredox cycle for CO_2 reduction. Typical photolysis experiments were conducted with a 130

mW·cm^{-2} Xe lamp equipped with an AM 1.5 filter to simulate the solar spectrum and intensity. A glass bubbler containing an acetonitrile solution containing CO_2 (~0.28 M), catalyst, photosensitizer, and quencher was illuminated, and the headspace was directly analyzed by GC every hour. As shown in Figure 6.5, the visible light photoredox cycle produced a significant amount of CO product over background, along with trace amounts of CH_4 and C_2H_4, with activity that persisted for at least 7 h. Moreover, no hydrogen was observed above the detection limit of 1 ppm, establishing the high selectivity of this photoredox system for CO2 over proton reduction. Table 1 summarizes the TONs and TOFs under a variety of conditions. At 200 nM of catalyst 1c and 0.2 mM $Ir(ppy)_3$, the TON and TOF values are 1500 and 0.058 s^{-1}, respectively, using the CO product quantified after 7 h of photolysis. Moreover, TONs and TOFs as high as 98,000 and 3.9 s^{-1}, respectively are determined using 2 nM loadings of 1c. The high turnover values achieved using this earth-abundant catalyst under visible-light photoredox conditions establish its promise for potential larger-scale CO production cycles.

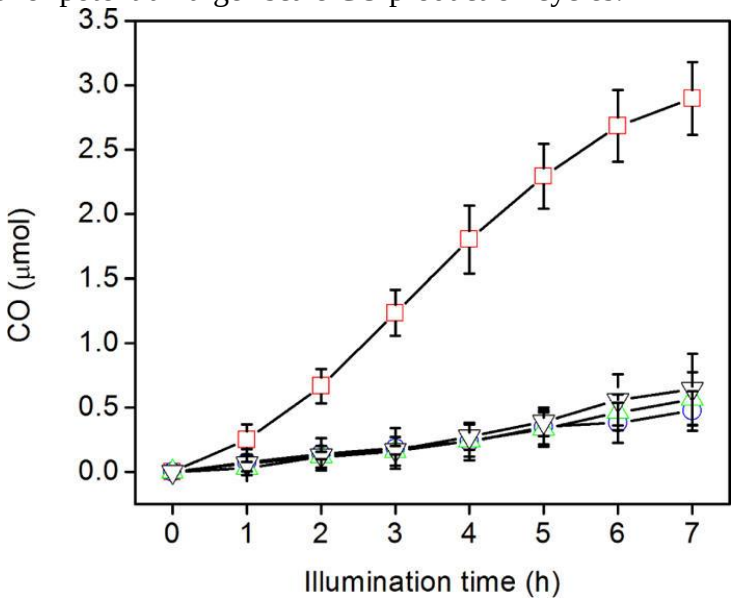

Figure 6.5. Photocatalytic reduction of CO_2 to CO in a 0.07 M TEA acetonitrile solution containing 0.2 mM Ir(ppy)3 (black triangles), 0.2 μM 1c (blue circles), 0.2 mM $Ir(ppy)_3$ and 0.2 μM Ni- $(CH3CN)_4(PF_6)_2$ (green triangles), and 0.2 mM $Ir(ppy)_3$ and 0.2 μM 1c (red squares), using a 130 mW·cm^{-2} Xe lamp fitted with an AM 1.5 filter.

[**1c**] (nM)	TON	TOF (s^{-1})
2	98,000	3.9
20	9,000	0.36
200	1,500	0.058

Table 6.1. Turnover Numbers (TON) and Turnover Frequencies (TOF) at various Concentrations of Catalyst 1c in an Acetonitrile Solution Containing 0.2 mM $Ir(ppy)_3$ and 0.07 M TEA Illuminated with a Light Intensity of 130 mW· cm^{-2}

A number of control experiments were performed to establish that all molecular components are necessary for the observed solar-to-fuel catalysis. First, negligible CO product was detected in an illuminated acetonitrile solution containing only 0.2 mM $Ir(ppy)_3$ photosensitizer and 0.07 M TEA in the absence of catalyst 1c. Additionally, solutions containing the simple nickel salt $[Ni(MeCN)_6]^{2+}$ or the free ligand 1b did not produce comparable activity to the nickel complex 1c. Control experiments without photosensitizer or quencher also showed negligible CO generation under photochemical irradiation, and no CO was produced in a dark reaction with all components added. To ascertain if heterogeneous particles were formed during photolysis, transmission electron microscopy (TEM) experiments were conducted on the samples before and after photolysis. Samples were prepared by drop-casting 100 μL of solution onto a thin-film copper or molybdenum TEM grid, and the grid was allowed to completely dry before loading into the instrument. The TEM images between samples pre- and post photolysis are similar, and several energy dispersive spectroscopy (EDS) measurements over large areas of the samples show no detectable Ir and Ni content at the sensitivity limit of this experiment.

6.5 Characterization of the Visible-Light Photoredox Cycle for Catalytic CO_2 Reduction

We next sought to probe various aspects of the photoredox cycle for catalytic CO_2 reduction mediated by nickel complex 1c. First, the quantum efficiency (QE) of the overall catalytic photoredox cycle for CO_2 reduction is determined by using the following equation:

$$\mathrm{QE} = \frac{\text{CO molecules} \times 2}{\text{incident photons}} * 100\%$$

Here, the number of incident photons can be calculated from the incident photon flux of 1.2 × 1021 photons·cm_2 ·h^{-1} (at 130 mW·cm^{-2}) and an illuminated area of 4.24 cm^2. The molecules of CO generated are then back-calculated from the concentration of CO (in ppm) and the total volume of the system (80 mL); after 7 h of photolysis, 2.1 × 10^{-5} mol of CO is produced. The calculated quantum yield for this visible-light molecular photosensitizer system is 0.01%, which is 2 orders of magnitude higher than that achieved using illuminated semiconductor powders.[336,337]

In an attempt to improve upon this yield, we varied the solar intensity under photoredox conditions. As plotted in Figure 6.6, the CO production rate increases almost linearly up to illumination intensities of 50 mW·cm^{-2} (which corresponds to an incident photon flux of approximately 1.32 × 1017 photons·s^{-1}). We observe that the CO production levels off with illumination intensities above this value, suggesting that the CO production rate is not limited by the light absorption past this point and that another step in the photoredox cycle is limiting the overall solar-to-fuel conversion efficiency. Furthermore, the relatively low intensity of light used

in the current photoredox system may be advantageous for conditions in which solar flux is limiting, such as when direct sunlight is not available.

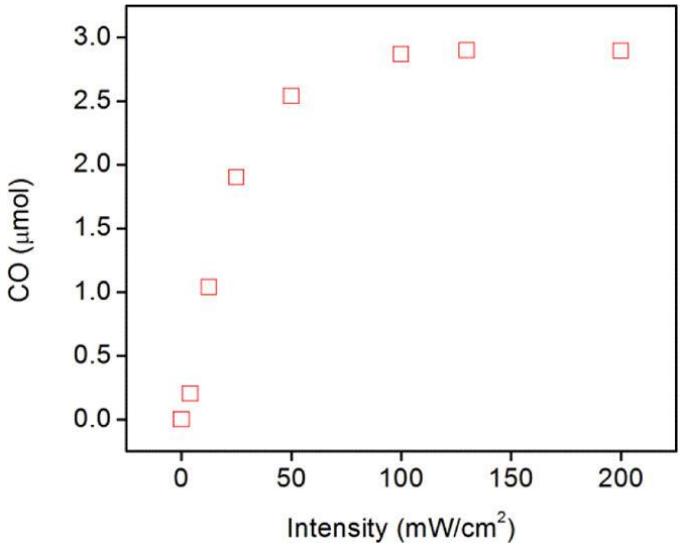

Figure 6.6. Photocatalytic reduction of CO_2 to CO in a 0.07 M TEA acetonitrile solution containing 0.2 mM $Ir(ppy)_3$ and 0.2 μM 1c while varying the light intensity of a Xe lamp fitted with an AM 1.5 filter.

We next examined the dependence of photosensitizer concentration on CO production by varying the concentration of $Ir(ppy)_3$ from 2 μM to 200 μM while maintaining the concentration of catalyst 1c at 200 nM and keeping all other reaction parameters constant. A plot of moles of CO productgenerated vs photosensitizer concentration shows a clear firstorder dependence on $Ir(ppy)_3$ concentration (Figure 6.7).

Similar experiments were performed where the concentration of 1c was varied. However, extracting useful kinetic information proved to be more elusive in this case. Although patent differences in the rates of CO product formation are observed when the catalyst concentration is varied between 0 and 200 nM, there are similar rates of product formation at 2 and 20 nM catalyst loading within experimental error. We speculate that this peculiar dependence may indicate a change in mechanism, as the concentration of the catalyst varies between 10- and 103 -fold less than the photosensitizer and between 103 - and 106 -fold less than the quencher; this open question will be a subject of future studies.

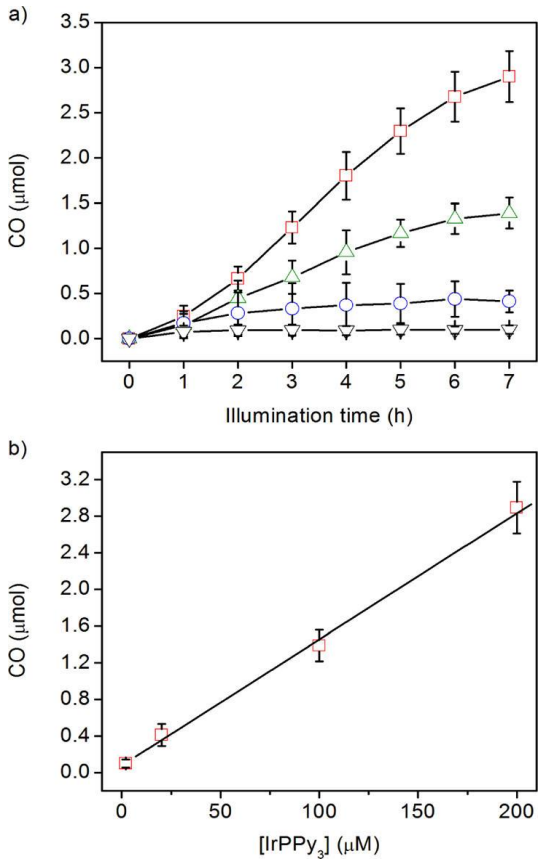

Figure 6.7. (a) Photocatalytic reduction of CO_2 to CO in a 0.07 M TEA acetonitrile solution containing 0.2 μM 1c and 0.2 mM (red squares), 0.1 mM (green triangles), 0.02 mM (blue circles), and 0.002 mM (black triangles) $Ir(ppy)_3$, using a 130 $mW \cdot cm^{-2}$ Xe lamp fitted with an AM 1.5 filter. (b) Linear plot of CO production at the end of 7 h versus $Ir(ppy)_3$ concentration.

To probe the mechanism of photoinduced electron transfer in this catalytic system further, we examined the rate of quenching of the Ir(ppy)3 excited state by the catalyst and by the electron donor, TEA, under our photocatalytic conditions using Stern−Volmer analysis according to the following equation:

$$\frac{I_0}{I} = 1 + k_q \tau_0 [Q]$$

In this equation, I0 and I are the fluorescence intensity in the absence and presence of the quencher, kq is the apparent rate of quenching, τ0 is the lifetime of the excited state, and [Q] is the concentration of the quencher. At an excitation wavelength of 400 nm, the fluorescence intensity at 517 nm for the Ir(ppy)3 lumophore was plotted against varying concentrations of catalyst 1c to give an apparent quenching rate constant of $1.7 \times 109\ s^{-1}$ (Figure 6.8). For comparison, typical rate constants for quenching of $[Ru(bpy)_3]^{2+*}$ are on the order of 107 −1010 s −1 ,[338] suggesting that direct oxidative quenching of the $Ir(ppy)_3$ with the catalyst can reasonably operate in this photocatalytic system. As further evidence for an oxidative quenching mechanism, the fluorescence of $Ir(ppy)_3$ is not attenuated when TEA alone was used as the quencher (Figure 6.8c).

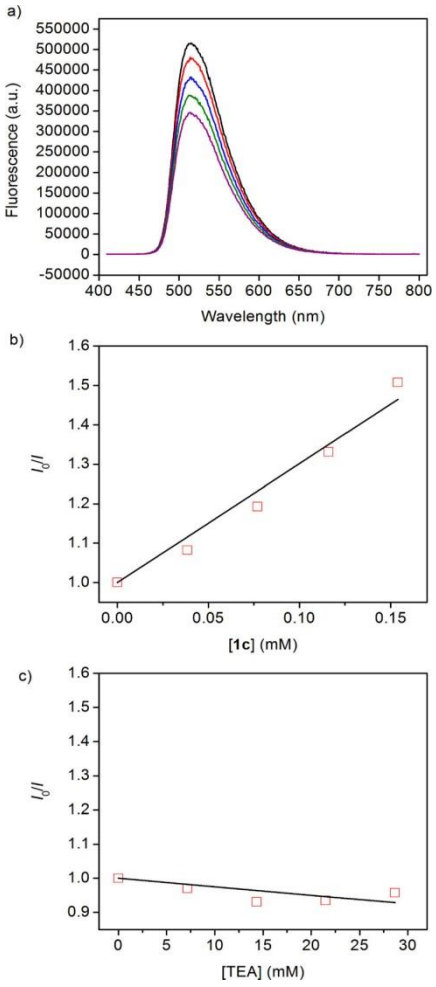

Figure 6.8. (a) Fluorescence spectra of an acetonitrile solution containing 0.05 mM Ir(ppy)3 in the absence (black) and presence of 0.04 mM (red), 0.08 mM (blue), 0.12 mM (green), and 0.15 mM (purple) 1c. (b) Linear plots of ratio of fluorescence intensities in the absence and presence of 1c versus the concentration of (b) 1c ($y = 3021x + 1$, $R^2 = 0.97$) and (c) TEA, according to the Stern−Volmer equation

Finally, we examined the role of the sacrificial reductant in the photoredox catalysis cycle. Oxidation of triethylamine by $[Ir(ppy)_3]$ + generates an amine radical, which can potentially act as an oxygen atom acceptor and form the N-oxide, diethylamine, and acetaldehyde.[339] We also screened a series of other electron donors. Using a standard set of conditions (0.2 mM $Ir(ppy)_3$, 0.2 μM 1c, and 0.07 M of the sacrificial reductant), we observed total CO production at 7 h increasing in the following order: isopropanol (IPA) < triethanolamine (TEOA) < dimethylaminoethanol (DMAE) < triethylamine (TEA). These results confirm the importance of the quencher in the photoredox system and may suggest that the ability of the sacrificial reductant to accept oxygen atoms can impact CO_2 reduction. For the realization of large-scale CO_2 reduction using this system, a more economic sacrificial reductant such as sulfite or ascorbic acid may be used in a solubilizing solvent.

6.6 Implications for Design of Improved Photoredox Systems for Catalytic CO_2 Reduction.

In addition to establishing an active and selective visible-light photoredox cycle for catalytic reduction of CO_2 to CO, the aforementioned results have implications for the future design of improved systems for solar-to-fuel conversion. Scheme 3 summarizes a potential set of reactions occurring during the photocatalytic reduction of CO_2 to CO. Upon illumination, $[Ir(ppy)_3]$ is excited to $[Ir(ppy)_3]$*, which is governed by the apparent rate constant k1. The excited [Ir(ppy)]* is then quenched and, with a reduction potential of −1.73 V,106 is oxidized by the nickel catalyst at an apparent kq (composed of kq1 and kq2) measured to be $1.7 \times 109\ s^{-1}$. Since the first and second reduction potentials of 1c are E1/2 = −0.92 and −1.38 V, the driving forces for generating the one- and two-electron reduced species are ∼800 and 350 mV, respectively. The oxidized $[Ir(ppy)_3]$ + is subsequently reduced by the sacrificial reductant at a reduction potential of $E_{1/2}$ = 0.77 V to close the catalytic cycle (apparent k2). On the basis of the electrochemical behavior of 1c, we speculate that 1c may be reduced twice via two one-electron transfers before being activated toward the two-electron reduction of CO_2 to CO (apparent kcat). As the overall conversion efficiency in our system is limited by the slowest of these complex processes, we have systematically probed various reaction parameters directly associated with each of these processes to find the critical factors that can be improved in future designs.

Visible-light absorption by the photosensitizer is unlikely to be a limiting step under our reaction conditions as the CO production remains constant at illumination intensities greater than 50 $mW \cdot cm^{-2}$. The first-order dependence of CO production on the $Ir(ppy)_3$ photosensitizer concentration also suggests that k1 is not rate-limiting. However, the identity of the sacrificial reductant does affect the production of CO and offers an alternative variable to tune for improvement. On the basis of these systematic experiments, we hypothesize that the ratedetermining step is likely either CO_2 reduction at the nickel center (kcat) or the reduction of 1c to the active Ni catalyst by $[Ir(ppy)_3]$* (kq), since two one-electron transfers from $[Ir(ppy)_3]$* to the Ni catalyst must occur for every one CO_2- to-CO transformation.

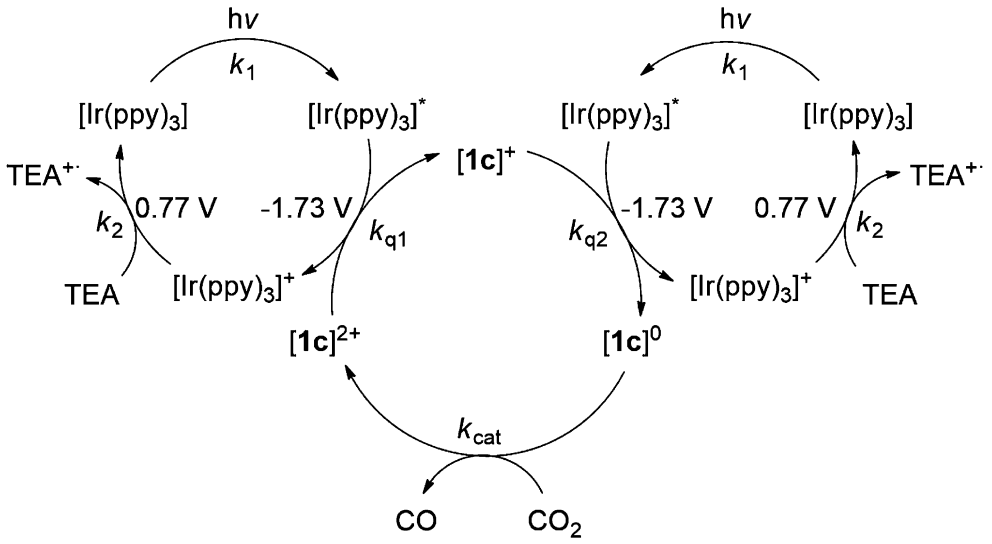

Scheme 6.3. Proposed Photoredox Cycle for Visible-LightInduced Reduction of CO_2 to CO

Finally, perhaps the most straightforward path forward for improvement is revealed by long-term stability measurements of the photocatalytic CO2 reduction cycle. The observed rate of CO production remains linear over a time span of 7 h but plateaus after this time point. However, when a second equivalent of visible-light photosensitizer was injected into the solution after 13 h of continued photolysis, CO production resumed at a similar rate (Figure 6.9). This result suggests that degradation of the photosensitizer, rather than catalyst deactivation, is a limiting factor for extended CO_2 reduction. Developing photosensitizers with greater photostability and more efficient absorption of incident visible and near-infrared photons in the solar spectrum is a promising strategy to increase the long-term activity and efficiency of these solar-tofuel conversion systems. Another direction is to increase the water-solubility or water-compatibility of the photosensitizer such that more economical electron donors such as sulfites and ascorbic acid can be employed.

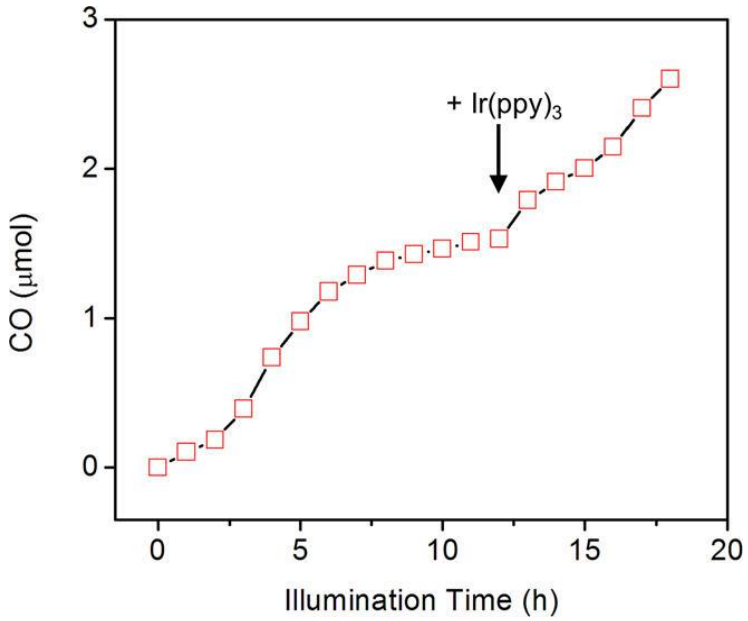

Figure 6.9. Photocatalytic reduction of CO_2 to CO in a 0.07 M TEA acetonitrile solution containing 0.2 μM 1c and 0.2 mM $Ir(ppy)_3$, using a 130 $mW \cdot cm^{-2}$ Xe lamp fitted with an AM 1.5 filter. At 13 h, a fresh source of $Ir(ppy)_3$ was injected, and CO production was continued.

6.7 Concluding Remarks

In summary, we have described the synthesis and characterization of a new family of nickel complexes supported by N-heterocyclic carbene−amine ligands and their application for electrocatalytic and photocatalytic reduction of CO_2 to CO. Focusing on N-heterocyclic carbene−isoquinoline complex 1c, the most promising candidate in terms of cathodic onset potential, controlled potential electrolysis studies establish its utility as a CO_2-to-CO reduction catalyst with high selectivity over competing off-pathway proton-to-hydrogen reduction reactions. Using this molecular CO_2 reduction catalyst in conjunction with the photosensitizer, $Ir(ppy)_3$, we have developed a visible-light photoredox system for the catalytic conversion of CO2 to CO at a relevant solar intensity of 130 $mW \cdot cm^{-2}$. Solar-driven CO_2 reduction proceeds with TONs and TOFs reaching as high as 98,000 and 3.9 s−1 , respectively, with no detectable formation of hydrogen. The overall solar-to-fuel efficiency of 0.01% for this molecular system is 2 orders of magnitude higher than that achieved using illuminated semiconductor powders. Experiments to probe various charge-transfer steps in this photoredox cycle reveal that the generation of the active Ni catalyst by [Ir(ppy)]* and the conversion of CO_2 to CO by the reduced nickel center are likely limiting steps. In addition to performing further ligand modifications to decrease overpotential and increase the rate of catalysis, current lines of investigation include optimizing electron transfer between photosensitizer and catalyst components, exploring molecular and solid-state photosensitizers with greater light-harvesting capabilities across the solar spectrum, translating this catalytic chemistry to environmentally benign aqueous media, and coupling this reductive light-driven half reaction to an appropriate oxidative process to achieve a complete solar-to-fuel system.

Parts if this section were published in: "Visible Photoredox Catalysis: Selective Reduction of Carbon Dioxide to Carbon Monoxide by a Nickel N-Heterocyclic Carbene Isoquinoline Complex", V Thoi*, **N. Kornienko***, C Margarit, P. Yang and C. Chang, *J. Am. Chem. Soc.*, 135, 14413 (2013).

7. Growth of Thin Film Metal Organic Frameworks

7.0 Preface

Chapter 6 detailed an in-depth study on a homogeneous CO_2 reduction catalyst that showed relatively high activity and selectivity in non-aqueous electrolyte. Our next goal was to retain the advantages of molecular level tunability and catalytic selectivity of molecular catalysts but also impart stability and efficiency in aqueous solvents. We envisioned that this can be accomplished by utilizing metal-organic frameworks as catalysts. These frameworks consisted of inorganic nodes that were linked together with molecular linkers that function as CO_2 reduction catalysts. In this way, a molecular catalyst can be effectively heterogenized to overcome barriers of stability and solublity. However, before this idea can be implemented, we had to develop a synthetic scheme to grow thin films of MOFs onto conductive substrates. A thin film growth was necessary because MOFs are intrinsically not conductive and charges transport primarily by hopping. Furthermore, when estimating turnover frequencies and loading densities in the MOF framework of our goal molecular catalysts, metalloporphyrins, we needed several tens of nanometers of MOF thickness. This value allowed us simultaneously balance mass and charge transport within the MOF framework with active site density to drive a sufficient CO_2 reduction current (3-5 mA/cm^2) at modest electrochemical overpotentials. In addition, a clean substrate-catalyst interface was necessary to efficiently transport charge. This chapter delves into detailed MOF growth and characterization in preparation for subsequent catalytic applications. Additional potential applications are discussed by growing MOFs directly on the surfaces of plasmonic nanoparticles.

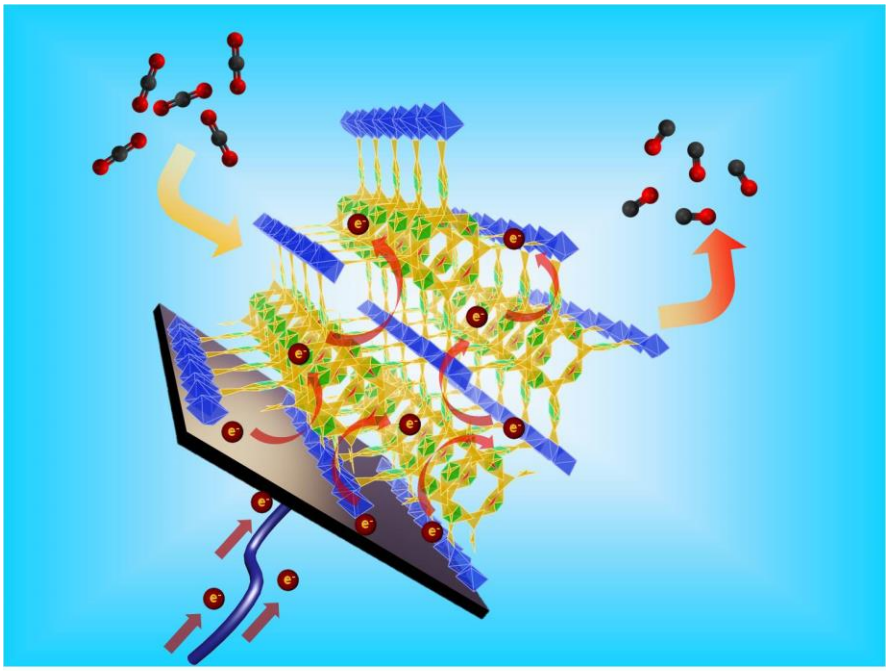

Scheme 7.1. Our enevisioned MOF catalyst featuring a 3D network of accessible molecular sites stabilized within an inorganic skeleton.

7.1 Introduction

Inorganic nanocrystals are important because they occupy a size regime intermediate between small molecules and extended structures. Their chemistry has been largely explored through surface functionalization. The fundamental problem is that it is difficult to control the spatial arrangement and order of the functional units and therefore the chemistry occurring at the interface between the inorganic nanocrystal and an incoming substrate. We believe that this 'functionalization problem' could be overcome by using metal-organic frameworks as well-defined units for which the spatial arrangement of functional organic and inorganic units, porosity, density and thickness can be precisely controlled. Addressing this problem requires a new synthetic approach to overcome four challenges: (a) a pristine interface between inorganic nanocrystals and MOFs that is free of surfactants and other surface ligands to take advantage of synergistic effects at the interface, (b) well-ordered and precisely oriented MOF enclosures around the inorganic nanocrystals to impart high degree of spatial control over the desired functional groups, (c) sufficiently thin MOF enclosures for facile diffusion and high resolution chemical mapping, and (d) bridging multiple length scales by combining the MOF atomically defined scale with the nano dimension for plasmonic structures, thus realizing new chemical and physical functions. In this way, it would be possible to construct mesoscopic assemblies where the MOF and the plasmonic nanocrystals are linked across multiple length scales yet operate differently and synergistically.

Although efforts to grow MOFs on inorganic nanocrystals have been made, a general method addressing all four challenges has not emerged [340-353]. In this work, a general method has been developed to overcome these four challenges using atomic layer deposition (ALD) technique where a thin metal oxide film is deposited onto plasmonic silver nanocrystals and used as a metal ion source to nucleate the desired MOF when the appropriate organic linker is added (Scheme 7.1). We show that ALD allows control of MOF thickness by controlling the metal oxide thickness, while the slow release of metal ions from the metal oxide layer results in control of crystallinity of MOF and ultimately its orientation on the silver nanocrystals. The MOF crystallinity, orientation, and the pristine interface thus produced enabled metalation and linker variation chemistry to be carried out on the MOF-silver nanocrystal mesoscopic construct. Integration of MOF onto nanocrystal surfaces further enables the direct probing of such chemistry by surface enhanced Raman spectroscopy (SERS) using the plasmonic silver nanocrystal substrates. Specifically, we show that the course of metalation in a porphyrin based MOF can be tracked and, in addition, different chemical signatures within MOF can be imaged at high spatial resolution down to a single nanoparticle level.

On a fundamental level, this system is an illustrative example of how two materials of self-similar structures can be combined into a mesoscopic ensemble of heterogeneous construction yet endowed with precisely defined chemical, spatial and metric characteristics. This coupled to the demonstrated ability to make mesoscopic constructs of these MOF-inorganic nanocrystals provides an unparalleled opportunity for tracking, probing and mapping of passing molecules; an aspect that is expected to be a boon for catalytic chemical conversions, sensing and imaging applications.

7.2 Results and Discussion

Our strategy to overcome the functionalization problem involves making silver nanoparticle-MOF constructs (O_h-nano-Ag⊂MOF) in which silver nanoparticles are wrapped by MOF enclosures. Silver octahedra were synthesized by the polyol method: silver nitrate salt is reduced by a pentanediol solvent and polyvinylpyrolidone (PVP) employed as a surfactant [354]. Silver nanocrystals are selected as a model plasmonic metal nanostructure as they have intense local surface plasmon resonances in the visible range and have been extensively studied as SERS substrates [355,356]. The chosen MOF is $Al_2(OH)_2$(TCPP) [TCPP: meso-tetra(4-carboxyphenyl)porphine], which consists of chains of corner-sharing aluminum octahedra running along the *b*-axis and connected by the TCPP units through the carboxylate groups (Fig. 1) [357]. This MOF was synthesized in bulk by reacting TCPP with $AlCl_3$ in water at 180 °C to give large, microcrystalline powder.

With the eventual goal of creating thin films of this MOF on the silver surface, we chose to use ALD thin films as a localized metal precursor source. The fabrication procedure of the O_h-nano-Ag⊂MOF begins with the deposition of Al_2O_3 films on the silver nanocrystals as the aluminum source for the MOF synthesis. The silver nanocrystal is drop cast on a silicon substrate and conformal, thickness-controlled alumina is deposited at 60 °C using trimethylaluminum and water as precursor at a deposition rate of 0.1 nm/cycle. The alumina coated silver nanocrystals are converted to MOF by reacting with the TCPP linker. However, the original hydrothermal condition used to synthesize this MOF would not be appropriate as the high temperature will melt the silver nanocrystals and the TCPP linker is not soluble enough in water to sufficiently react with alumina. Considering this, the reaction temperature was reduced to 140 °C, and DMF water mixed solvent is used, containing 5 mg TCPP dissolved in 1.5 ml DMF and 0.5 ml H_2O. The conversion of alumina to MOF was carried out in a sealed glass tube in a microwave reactor using, in the initial runs, 20 nm thick layers of alumina. Unfortunately, an interfacial 10 nm thick alumina layer between the MOF and the silver was observed instead of the desired pristine interface. This lead us to reduce the alumina layer thickness to below 3 nm and found it to be sufficient to eliminate the interfacial alumina layer while enabling the fabrication of conformal and thin MOF enclosures (Scheme 7.1).

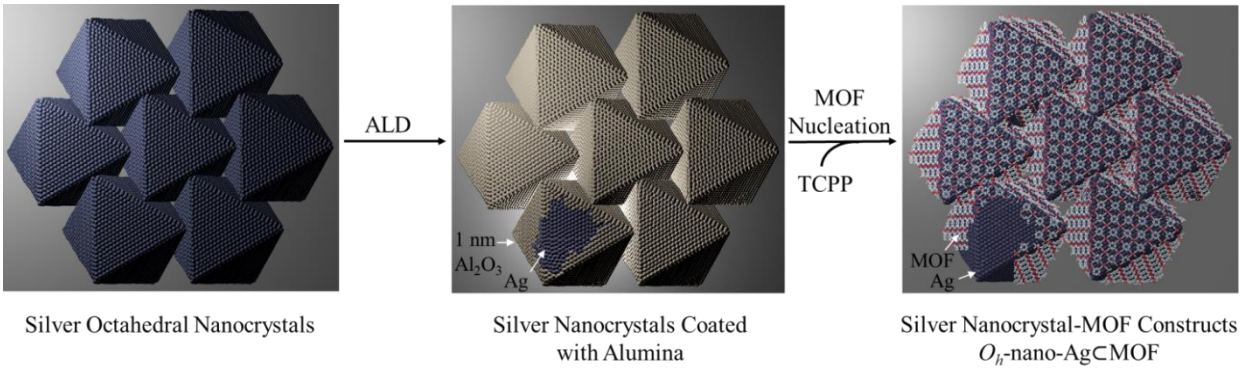

Scheme 7.1. The fabrication process of O_h-nano-Ag⊂MOF particles

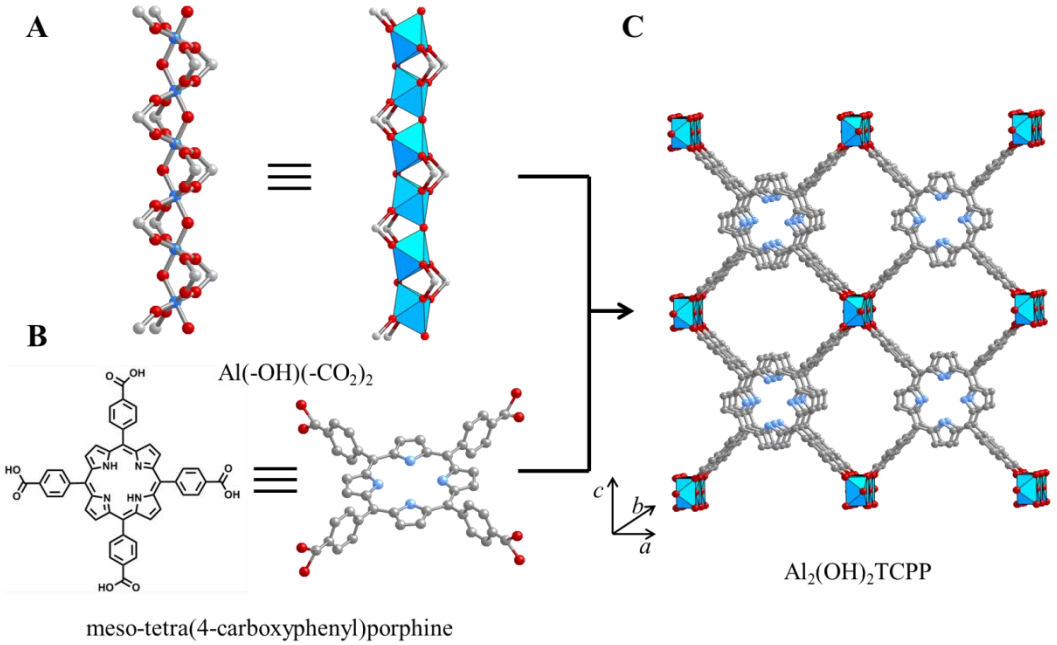

Figure. 7.1. The structure of $Al_2(OH)_2TCPP$ MOF. Construction of $Al_2(OH)_2TCPP$ MOF from (**A**) rod-shaped aluminum oxide units linked by (**B**) porphyrin units (TCPP) to give a three-dimensional MOF (**C**) having 0.11×0.6 nm^2 opening along the *b*-axis [357]. Al, blue octahedral polyhedra and blue spheres in (**A**); N, blue spheres; O, red spheres; C, gray spheres. Hydrogen atoms are omitted for clarity.

We next utilized Raman spectroscopy to characterize the MOF composition of the thin film and in particular detect the signature of the porphyrin building units in the MOF. However, we found that the PVP at the interface between the silver and MOF gave a strong signal which overwhelmed the Raman spectrum. We address this issue by employing an additional surface cleaning step using a Meerwein's salt treatment to remove PVP surfactant before coating the silver with ALD alumina to ensure a pristine interface between the MOF and Ag nanocrystal (fig. S2) [358]. Following the surfactant removal, the MOF conversion was carried out again, and only the strong TCPP signal was visible in the Raman spectrum.

The phase purity and high crystallinity of the MOF enclosures synthesized using 1, 5, and 30 cycles of ALD Al_2O_3 is confirmed by grazing incidence wide angle x-ray scattering (GIWAXS) measurements. Scanning electron microscopy (SEM) was used to characterize the morphology of O_h-nano-Ag⊂MOF, and showed that the shape of the silver nanocrystal is retained throughout the process of fabrication and crystalline plate-like MOF regions are visible on the silver nanocrystal surface (Figure 7.2A, B).

We proceeded to quantify the thickness control of the resulting MOF enclosures by controlling the ALD layer thickness. Figure 7.2 shows typical SEM and transmission electron microscopy (TEM) images of MOF films obtained from alumina layer thicknesses of 3, 0.5, and 0.1 nm (Figure 7.2C-H). With increased cycles of alumina, the size and coverage of MOF crystallites on the Ag surface as well as the overall MOF layer thickness increases. The average thickness of the MOF enclosures are approximately 50 nm, 25 nm and 10 nm for 30 cycles, 5 cycles and 1 cycle ALD alumina, respectively (Figure 7.2F-H). At the lowest limits of the ALD precursor film thickness of less than one nanometer, highly crystalline MOF enclosures as thin as several nanometers were made. The crystallite size and morphology of the MOF was finely tuned by varying the reaction conditions: a water:DMF ratio of 3:1 solvent mixture results in a more uniform, conformal MOF enclosure in contrast to the plate-like structure.

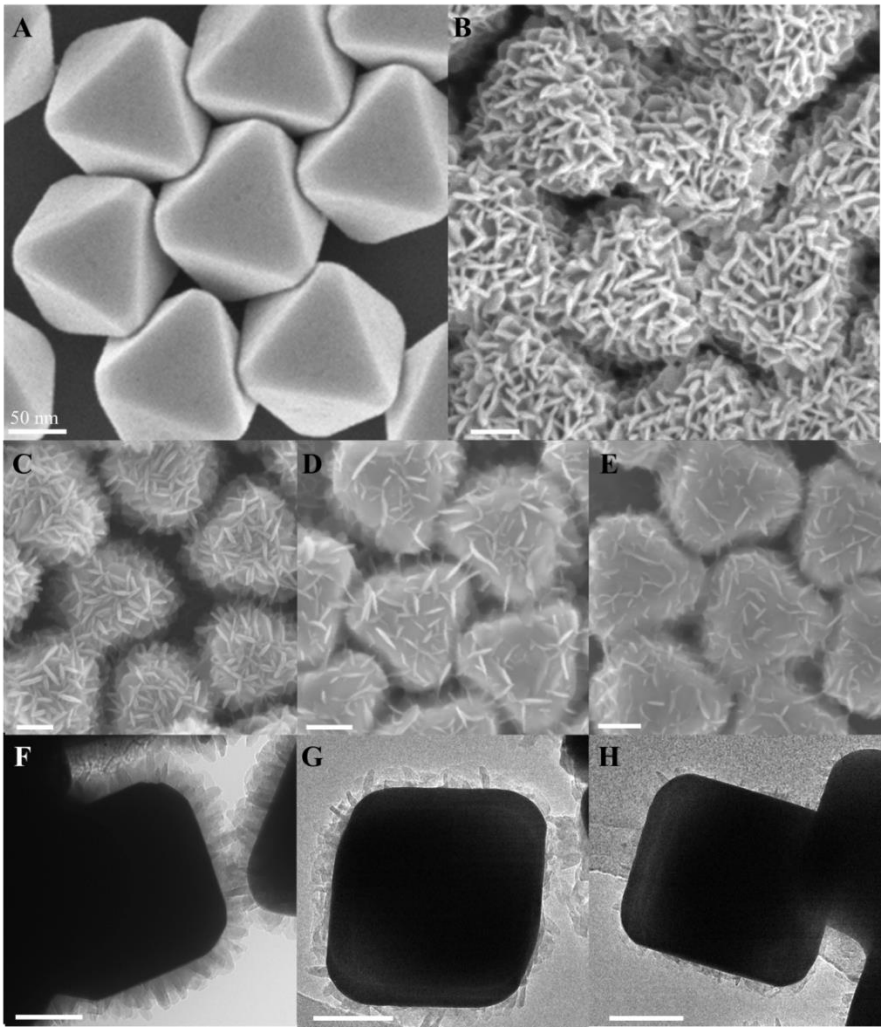

Figure 7.2. The SEM and TEM images of the O_h-nano-Ag⊂MOF particles. Octahedral silver nanocrystals (**A**) are subjected to ALD deposition of alumina followed by addition of TCPP linkers to make MOF enclosed silver nanocrystals, O_h-nano-Ag⊂MOF, (**B**). Variation in the alumina thickness from 3 to 0.5 to 0.1 nm allows control of MOF coverage on the silver nanocrystals with their SEM shown respectively (**C** to **E**) and the corresponding TEM (**F** to **H**) where the thickness and coverage of the MOF is further confirmed. The black square-like figure in **F** to **H** is the silver nanocrystal. Scale bars are all 50 nm.

The MOF crystallinity and orientation at the interface was examined by high resolution TEM. Imaging at a low electron dosage and accelerating voltage of 120 KV showed MOF lattice fringes (Figure 7.3A). This confirms, at a microscopic level, the high crystallinity of the MOF enclosure at the interface and the fact it is pristine. The orientation of the MOF regions was determined from the TEM images (Figure 7.3B), where the lattice fringes of 1.6 nm correspond to the MOF (200) planes parallel to the interface. This indicates that the porphyrin units of the MOF are perpendicular to the silver surface. The two dimensional lattice fringes of 1.16 nm, which correspond to MOF (201) plane, are also observed (Figure 7.3C), and thus provide an unambiguous determination of the MOF orientation being perpendicular to the silver surface. No evidence of porphyrin units oriented parallel to the silver surface was found among the TEM images. Energy dispersive x-ray spectroscopy (EDS) elemental mapping was utilized to further confirm the enclosed structure of the O_h-nano-Ag⊂MOF as described further below.

GIWAXS structural analysis is performed on a macroscopic level using a flat silicon substrate for MOF growth to further confirm the crystallinity and orientation of the MOF at an ensemble level. The spot pattern on GIWAXS image (Figure 7.3D) matches that expected for the preferred orientation of the MOF with the porphyrin units perpendicular to the substrate (MOF [200] direction perpendicular to the substrate). A random orientation of the MOF would result in a ring rather than a spot pattern in the GIWAXS image. This oriented growth is also observed when glass is used as substrate to grow the MOF, which suggests that the oriented MOF growth is not substrate specific. The TEM and GIWAXS findings combined lead to a structural model of the MOF-substrate interface (Figure 7.3E), in which the porphyrin units of the MOF are perpendicular to the interface. This clearly demonstrates that this synthetic approach is well-suited for fabricating crystalline and precisely oriented MOF enclosures on inorganic nanocrystals. Knowledge of the porphyrin orientation to the silver nanocrystals also conveys their spatial arrangement and allowed us to carry out, for the first time on a nanocrystal substrate, chemistry specific to the porphyrin units (metalation with cobalt, see below) and probe it by SERS.

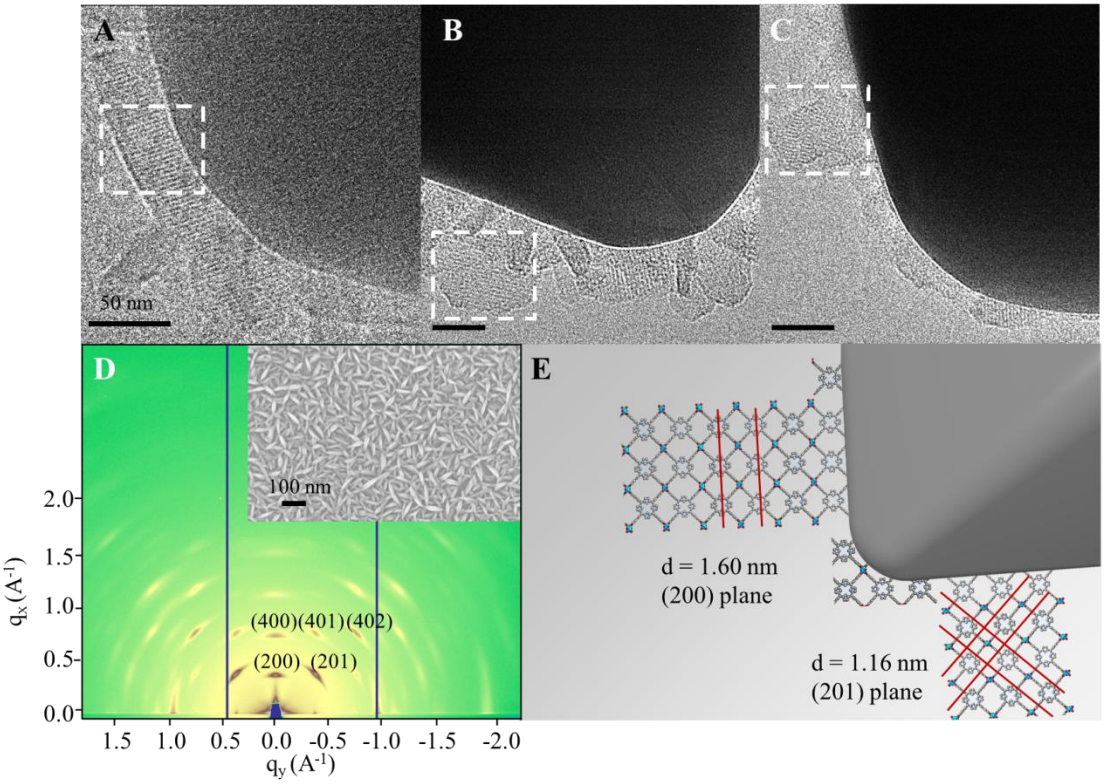

Figure 7.3. Order (crystallinity) and orientation of MOF on the silver nanocrystal interface. High resolution TEM images of the O_h-nano-Ag⊂MOF showing the MOF lattice fringes of 1.16 nm (bordered by dotted rectangle) (**A**) corresponding to the MOF (201) plane, and clearly shows a pristine interface with the silver nanocrystals (large darkened shapes). Confirmation of MOF orientation is evidenced by the lattice fringes of 1.6 nm (bordered by dotted rectangle) (**B**) corresponding to the MOF (200) plane and indicating that the porphyrin units in the MOF enclosure are perpendicular to the silver nanocrystal surface. Further confirmation of this orientation is evident by the lattice fringes of 1.16 nm (bordered by dotted rectangle) (**C**), in this case, recorded along two directions, corresponding to the (201) planes. The crystallinity of the MOF enclosure and its orientation in O_h-nano-Ag⊂MOF are confirmed by GIWAXS diffraction plot (**D**) which shows spot pattern indicative of high crystallinity and preferred orientation. The in-plane diffraction spot of MOF (200) and (400) indicates the porphyrin is perpendicular to the substrates with the *b*-axis parallel to the substrate (**D** and **E**). Another indistinguishable assignment [the in-plane diffraction spot is (001) and (002)] gives the same conclusion concerning the *b*-axis and the porphyrin orientation. The scale bars are all 20 nm.

It is worth noting that this approach for making mesoscopic constructs can also produce MOF on other substrates such as carbon disk with the same morphology and crystallinity. In addition, this method of MOF fabrication is also applicable to a variety of MOFs made up of other metals. Here, the appropriate metal oxide could be used as a precursor. For example, a film of ALD indium oxide was used as the metal precursor to react with TCPP to give an isoreticular

(having the same net topology) indium MOF as the present aluminum MOF. Different linkers could also be used to react with the same oxide to give the corresponding MOF, as in the case of DUT-5, in which *biphenyl-4, 4'-dicarboxylic acid* was used. A member of a subclass of MOFs, ZIF-8, could also be fabricated using ALD zinc oxide. We expect that since this MOF fabrication approach is substrate independent, it is generalizable and can be extended to produce multiple oriented and ordered MOF enclosures on a variety of inorganic nanostructures.

With the ability to form thin MOF enclosures on plasmonic nanocrystals without an interfacial surfactant layer, unprecedented opportunities emerge in high resolution probing of chemical processes in MOF using SERS. The pristine interface enables the synergistic effects between the MOF enclosure and the silver nanocrystals. In a O_h-nano-Ag⊂MOF sample, all peaks in the SERS spectrum match those of the bulk MOF and the TCPP molecule and can be assigned according to previous literature studies of porphyrin molecules.[359,360] This spectroscopic handle allowed us to track the metalation of the porphyrin units within the MOF enclosure. Metalation was carried out by heating the O_h-nano-Ag⊂MOF in a 10 mg/ml cobalt acetate methanol solution at 100 ^oC under microwave irradiation. The metalation of the porphyrin molecule is evidenced mainly by the decline of the υ_8 mode corresponding to the free base porphyrin at 330 cm^{-1} and the rise of the υ_8 mode of the metalated porphyrin at 390 cm^{-1} [359]. This is further confirmed by UV-Vis spectroscopy and energy dispersive x-ray spectroscopy (EDS) where in the latter, elemental mapping is utilized to further confirm the enclosed structure of the O_h-nano-Ag⊂MOF. Within the enclosure of MOF, this post-synthetic metalation is tracked with SERS (Figure 7.4A) and found to be complete within 50 minutes; thus pointing to the facile diffusion of the cobalt acetate reagent due to the porosity of the MOF and access to the silver interface.

The confocal Raman SERS mapping is next applied to study heterogeneous MOF enclosures on silver nanocrystals and the unique capability of this system to generate spatially resolved chemical information. The size of an O_h-nano-Ag⊂MOF octahedron is 300 nm, which is similar to the diffraction limited spatial resolution possible with a 532 nm laser in a confocal microscopy setup. Therefore, chemical information at the limit of a single silver nanoparticle can be obtained. The multivariate approach, in which different organic linkers are incorporated into the same framework, is a powerful technique to introduce heterogeneity and complexity into MOFs and one that has presented challenges to its characterization due to lack of techniques capable of deciphering the spatial arrangement of the linkers [361].

Here, pre-metalated porphyrin linker, meso-tetra(4-carboxyphenyl)porphinato cobalt (II) , was mixed with the unmetalated TCPP linker in a 1:3 ratio in the precursor solution and reacted with the alumina coated silver nanocrystals under the conditions described above. The SERS spectrum was measured on clusters of O_h-nano-Ag⊂MOF particles, and found to have peaks attributable to υ_8 mode of both the metalated and unmetalated forms of the porphyrin unit. One of the fundamental difficulties in nano-MOF chemistry is to decipher whether the nanoparticles as a whole are homogenous in their composition, especially when a multivariate approach in metalation or mixing of linkers is employed in the synthesis of the MOF. The materials prepared here allow us to address this issue. Mapping of the metalated and unmetalated linkers in a monolayer of O_h-nano-Ag⊂MOF using SERS reveals a well-mixed porphyrin system. In that, on the single particle level there is no segregation of metalated and unmetalated regions of the MOF (Figure 7.4C, D). This is quantified by the ratio of the Raman scattering intensity of the two υ_8 modes for the metalated and unmetalated. This ratio is obtained from integrating the

corresponding peaks and it is found to lie at 1.5 which is in between all metalated and all unmetalated scenarios (Figure 7.4C), which indicates that the distribution is homogenous from particle to particle as evidenced from mapping 7 μm regions (Figure 7.4D).

To illustrate the power of combining MOF and plasmonic nanocrystal into one mesoscopic construct, O_h-nano-Ag⊂MOF, we examined an area occupied by multiple discrete particles for their chemical composition using confocal Raman spectroscopy. Figure 7.4F and G show the area of particles and their corresponding SERS maps, respectively. It is very clear that because of the thin enclosure of MOF around the silver, it is possible to observe strong SERS signals for each of the particles and furthermore within each such particle the metalated and unmetalated porphyrin units in the MOF can be observed. This is possible because the MOF is grown on a plasmonic inorganic nanocrystal with a clean interface. Comparison of Figure 7.4F and G also reveals that the SEM and SERS mapping are consistent in providing a highly resolved picture of the spatial arrangement of the mesoscopic O_h-nano-Ag⊂MOF particles.

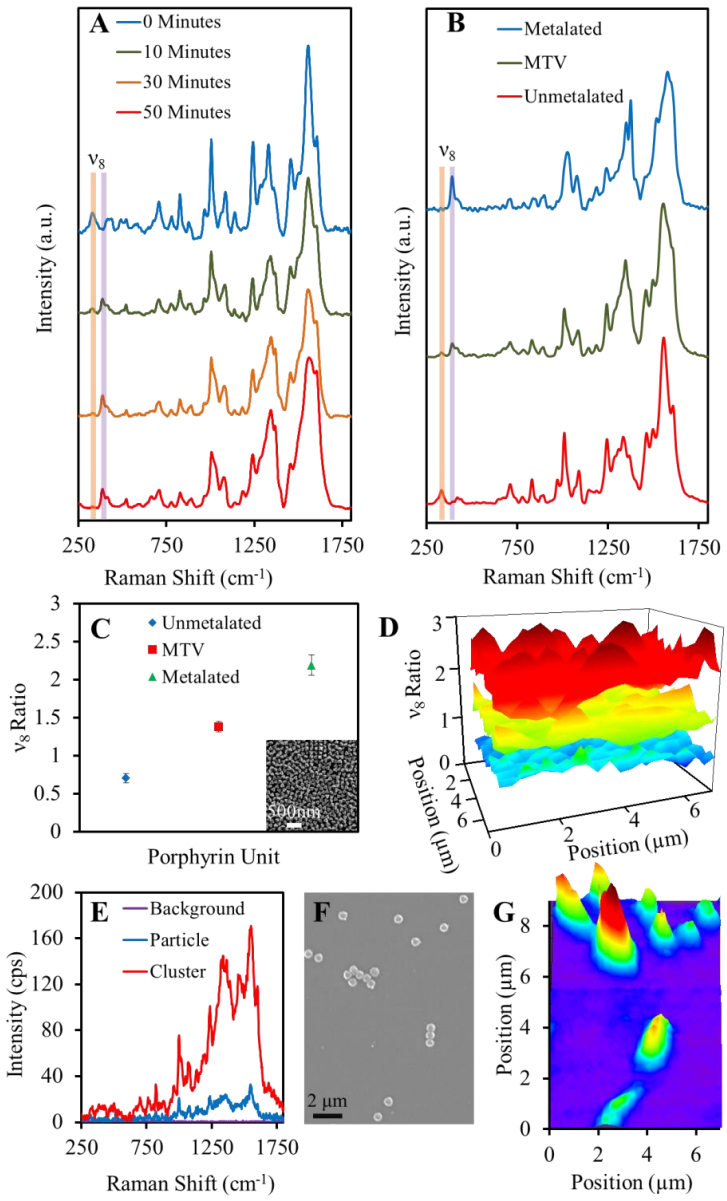

Fig. 4. Tracking metalation of MOF linkers and mapping of metalated and unmetalated linkers in O_h-nano-Ag⊂MOF using SERS. Time-dependent SERS spectroscopic tracking of metalation of the porphyrin linker units (**A**) showing the evolution of the ν_8 mode and the completion of reaction within 50 minutes. The SERS spectra for metalated, unmetalated, and multivariate metalated O_h-nano-Ag⊂MOF (B) showing the system is multivariate (mixed metalated and unmetalated MOF enclosures). The ratio of metalated and unmetalated linkers (**C**), and the homogeneity of these in the MOF enclosures is mapped (**D**). The SERS enhancement shown for single particles and clusters of O_h-nano-Ag⊂MOF (**E**), SEM of spatially resolved discrete O_h-nano-Ag⊂MOF (**F**), and the result of their SERS mapping showing the one-to-one correspondence.

7.3 Concluding Remarks

In conclusion, we have developed a growth scheme for thin films of MOFs on arbitrary surfaces. We have shown that that a number of different structures can be grown from precursor metal oxide films, rendering this a highly generalizable approach. One potential application in SERS sensing was demonstrated by growing a multivariate MOF on silver nanoparticles and tracking the spatial distribution of metallated and non metallated porphyrin linkers. The next step in this direction is to utilize these thin film MOFs as CO_2 reduction catalysts.

Parts of this section were published in: "Mesoscopic Constructs of Ordered and Oriented Metal-Organic Frameworks on Plasmonic Silver Nanocrystals" Y. Zhao*, **N. Kornienko***, Z. Liu,C. Zhu, S. Asahina, T. Kuo, W. Bao, C. Xie, O. Terasaki, P. Yang, O. Yaghi, *J. Am. Chem. Soc.*, 137, 2199, 2015

8. Metal-Organic Frameworks as CO_2 Reduction Electrocatalysts

8.0 Preface

In this chapter I continued in the direction of MOF research towards CO_2 reduction. In chapter 7, a synthetic strategy for growth of thin films of MOFs was developed. Here, I used a cobalt porphyrin functionalized MOF as a CO_2 reduction electrocatalyst. Utilizing a MOF as a catalyst imparts several advantages over both homogeneous and heterogeneous catalysts. In this work, we show that our MOF catalyst overcome solubility and stability issues that limit many homogeneous molecular catalysts while exhibiting precise molecular level tunability that cannot be easily achieved with heterogeneous catalysts. We explored balancing active site density with mass and charge transport in our MOF films by varying the MOF thickness. Furthermore, we used *in situ* techniques to probe the oxidation state of the cobalt active sites during catalysis. Our optimized catalyst performed favorably compared to the best heterogeneous and homogeneous catalyst and offers plenty of room for improvement.

8.1 Introduction

One of the most attractive approaches towards providing carbon-neutral energy is the electrochemical conversion of atmospheric carbon dioxide (CO_2) into energy dense carbon compounds to be used as fuels and chemical feedstock.[242,245,362,363] Extensive efforts have been devoted to the development of homogeneous and heterogeneous catalysts for this purpose. The outstanding challenges remain in the design of catalyst systems featuring (I) selectivity for CO_2 reduction in water with minimum H_2 generation, (II) long term stability, (III) catalytic efficiency at low electrochemical overpotential and (IV) compositions of earth abundant materials. In this report, we show that nanosized metal-organic frameworks (MOFs) meet these criteria and also present additional opportunities because of the flexibility with which their components can be functionalized and precisely arranged in the crystal structure.[364-371] We chose a stable cobalt porphyrin MOF where these porphyrin units are linked with aluminum oxide rods to form a 3-dimensional porous structure with pores of 6 × 11 *Å*. Electrochemical CO_2 reduction studies were performed on thin films of the nano form of this MOF, which was found to convert CO_2 to CO selectively (76% Faradaic efficiency) and with high turnover number (TON = 1400). *In situ* spectroelectrochemical measurements revealed that the Co(II) centers are reduced to Co(I) throughout the MOF and subsequently reduce CO_2. This is the first MOF catalyst construct for the electrocatalytic conversion of CO_2 to CO, and its high performance characteristics are encouraging for the further development of this approach.

In the context of aqueous electrocatalytic CO_2 reduction studies where heterogeneous catalysts, such as metal foils,[268,372-375] metal nanostructures,[376-384] oxide derived metals,[269-271] 2-dimensional materials,[385] carbon nanomaterials,[386-388] bio-inspired catalysts,[389-392] and homogenous molecular catalysts[273,278,299,302,305,393-397] are used; MOFs combine the favorable characteristics of both heterogeneous and homogeneous catalysts. Exploration of MOFs for CO_2 reduction has only just begun through their use as photocatalysts in colloidal dispersions, however with the aid of sacrificial reagents[398-400] and MOFs have only twice been utilized as electrocatalysts for CO_2 reduction, though not for CO generation.[401,402]

Our strategy to construct the MOF-based electrochemical CO_2 reduction system was to select MOFs with catalytic linker units and fabricate them into thin films covering conductive substrates homogeneously (Figure 1): appropriate catalytic linker units (Figure 1A) are assembled into a porous thin film MOF (Figure 1B, Figure S1) which is grown homogeneously on a conductive substrate (Figure 1C). We first screened MOFs with systematically varied building blocks and then chose the most promising MOF catalyst for in depth electrochemical studies. The thickness of the selected MOF was next optimized to yield the final CO_2 reduction system, which was shown to be active, selective, and stable towards CO production. We also demonstrate that the majority of cobalt centers are reduced from Co(II) to Co(I) during the electrochemical process through *in situ* spectroelectrochemical measurements. Using MOFs as heterogeneous electrocatalysts is an efficient strategy to reticulate catalytic molecular units into a porous network in which the number of active sites is maximized and both charge and mass transported could be simultaneously balanced by controlling the nanoscopic MOF morphology.

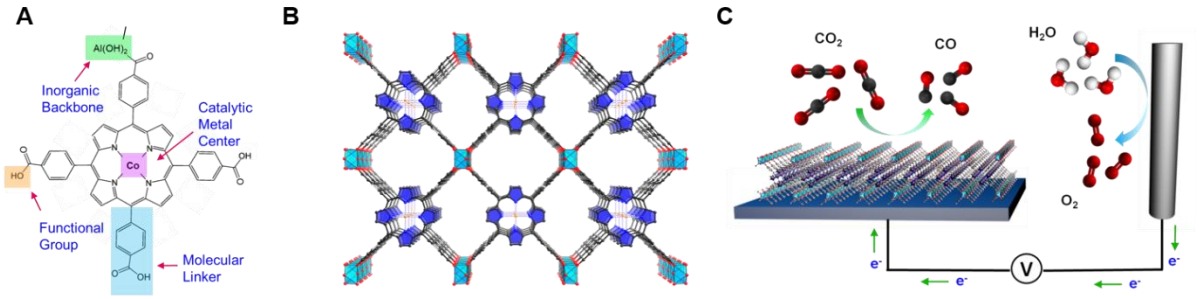

Figure 8.1. Our MOF catalyst allows for modulation of metal centers, molecular linkers, and functional groups at the molecular level (A). The organic building units, in the form of cobalt metallated TCPP, are assembled into a 3-dimensional MOF, Al2(OH)2TCPP-Co with variable inorganic building blocks (B). Co, orange spheres; O, red spheres; C, black spheres; N, blue spheres; Al, light blue octahedra; pyrrole ring, blue. The MOF is integrated with a conductive substrate to achieve a functional CO2 electrochemical reduction system (C)

8.2 Results and Discussion

The catalysts we selected in this work are the $Al_2(OH)_2TCPP\text{-}H_2$ series [TCPP-H_2 = 4,4',4",4"'-(porphyrin-5,10,15,20-tetrayl)tetrabenzoate], which incorporate the porphyrin-based molecular units previously reported as selective and efficient homogeneous CO_2 reduction electrocatalysts.[393,403,404] Specifically, the cobalt metallated porphyrin units are known to be of particular interest for CO_2 reduction and are explored in detail in this work.[405-407] The advantage over using molecular porphyrins as homogeneous catalysts is that each active site is simultaneously exposed to the electrolyte and electrically connected to the conductive support. We employ our previously developed methodology for thin-film MOF synthesis,[408] which involves the ALD deposition of metal oxide thin films as metal precursors onto the electrode and

subsequent MOF creation through reacting the coated electrode with the appropriate linker in a DMF solvent in a microwave reactor.[345]

Initially, we studied the effect of employing different metal centers in the porphyrin units on the catalytic properties of the MOF (Figure S3). We began with 50 ALD cycles of alumina thin films (thickness of 5 nm) deposited onto conductive carbon disk electrodes, and converted the alumina film to porphyrin-containing MOF [$Al_2(OH)_2$TCPP-M'] structures with free-base porphyrin as well as porphyrin centers metallated with M' = Zn, Cu, and Co. Cyclic voltammetry (CV) measurements of the synthesized metallated porphyrin containing MOFs under an argon or carbon dioxide environment were used to screen the MOF catalytic performance (Figure S2). The voltammogram traces feature redox waves attributed to the reduction of the metal centers and catalytic peaks stemming from the reduction of either protons or aqueous CO_2, qualitatively matching the behavior of previously studied analogous porphyrin homogeneous catalysts.[403] Notably, the cobalt metallated MOF exhibits the highest relative increase in current density after saturating the solution with carbon dioxide (1 atm, 33 mM concentration), increasing from 3.5 to 5.9 mA/cm^2. Hence, this particular catalyst is chosen for further in-depth examination. Previous works have reported differences in activity and selectivity amongst porphyrins and porphyrin analogues with different metal centers and cobalt was consistently among the best.[409,410] To exhibit a further layer of modularity with our MOF-based catalyst design, we modified the inorganic backbone to prepare cobalt metallated [$M_2(OH)_2$TCPP-Co, M = Al and In] MOFs (Figure S4, S5). The In and In-Al based MOF catalysts also exhibit significant current density increases under a CO_2 saturated aqueous bicarbonate electrolyte relative to an argon bubbled electrolyte, suggesting that the porphyrin units are the essential catalytic active center and the inorganic backbone may be tuned for other purposes.

Based on our initial catalyst screening, we focused our subsequent investigation on the [$Al_2(OH)_2$TCPP-Co] MOF. The voltammogram trace of this MOF showed an enhanced current density under a CO_2 saturated solution relative to argon saturated solution and displayed a reversible redox couple in addition to an irreversible catalytic peak (Figure 2A). Increasing the CV scan rates (Figure 2B) illustrated that a cathodic wave centered roughly -0.4 to -0.5 V vs. reversible hydrogen electrode (RHE), an irreversible catalytic peak immediately following, and an anodic peak at -0.2 V vs. RHE increase in magnitude linearly proportional to the square root of the sweep rate, indicative of a diffusion limited process (Figure 2C).[411,412] The first cathodic wave and the lone anodic wave are likely due to counter ion diffusion to balance a Co(II/I) redox change and the irreversible cathodic peak at the most negative potentials stems from the diffusion and subsequent reduction of carbon dioxide. The wave separation increased from ~100 mV to ~250 mV with increasing sweep rate, which provided evidence that the underlying reaction is not a simple reversible redox process. Previous electrochemical studies of cobalt porphyrins have attributed a cathodic wave at -0.5 V vs. RHE to the reduction of the Co(II) to Co(I) center and we see similar behavior for the homogeneous H_4TCPP-Co (Figure S6).[413] Spectroelectrochemical studies confirmed the chemical nature of this cathodic wave as discussed below.

Balancing reactant diffusion and charge transport is essential for electrochemical catalysis. To this end, the thickness of the MOF catalyst film is tuned to optimize the performance of the MOF catalyst by varying the starting ALD alumina layer thickness from 0.5 to 10 nm (Figure 2D).

Upon testing a carbon disk electrode with only 5 layers (0.5 nm) of ALD precursor converted to the MOF, resulting in a ~10 nm thick MOF layer, we observed a two-fold increase in the catalytic current density (measured at -1.2 V vs. RHE at a sweep rate of 100 mV/s) relative to the bare carbon disk substrate. The performance of the MOF catalyst increased with increasing active site loading until reaching a maximum at 50 ALD cycles. Inductively coupled plasma atomic emission absorption (ICP-AES) was utilized to quantify the total cobalt loading on this sample and indicated an upper limit of 6.1×10^{16} cobalt atoms (1.1×10^{-7} mol) per cm^2. The performance decrease observed for higher active site loading is likely due to charge transport limitations from the electrode to the MOF periphery or impedance through a thin insulating alumina layer not fully converted to the MOF. This result highlights the strength of our ALD-based MOF conversion technique, which allows nanometer precision of catalyst loading to balance active site density with mass/charge transfer.

Comprehensive product analysis using gas chromatography (GC) and nuclear magnetic resonance (NMR) was carried out to reveal the nature of the chemical processes occurring within our MOF catalysts (Figure S7). As illustrated in Figure2E, the two main products measured were CO and H_2, with current selectivity for CO reaching up to 76% at -0.7 V vs. RHE. The average steady state current density from these measurements is displayed in Figure 2F. When plotting the partial current density for CO production on a logarithmic scale vs. the thermodynamic overpotential (Figure 2G) we obtain a Tafel slope of 165 mV/decade in the low overpotential region, which points to a one electron reduction of CO_2 to form the $CO_2^{\cdot}$ radical as a probable rate limiting step, though the reaction may is likely to be at least in part diffusion limited.[268,414-416] For comparison, studies of porphyrin homogeneous catalysts have measured Tafel slopes ranging from 100 to 300 mV/decade; thus, the rate limiting step and mechanism may depend on more than just the active site itself.[417-419] We stress that this is the first incarnation of our MOF electrocatalyst and efforts are being undertaken to further exploit the modular nature of such systems for the next generation of catalyst.

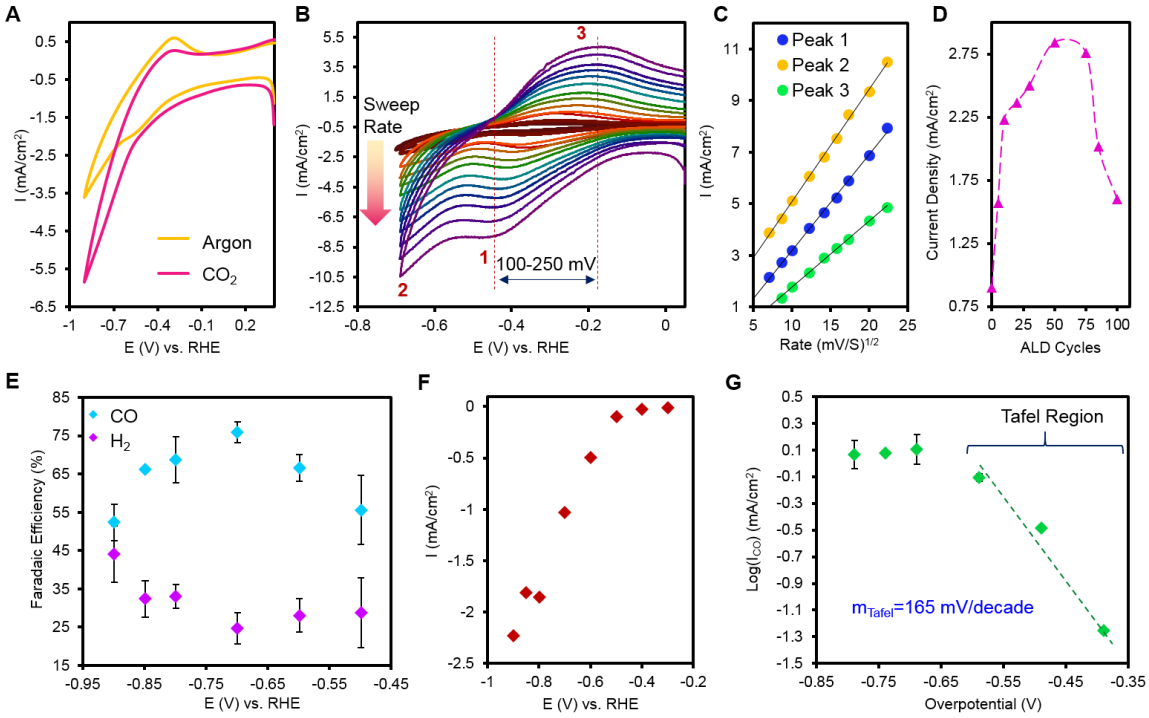

Figure 8.2. The voltammogram trace of the MOF catalyst exhibits a current increase in a CO2 environment relative to an argon saturated environment (A). As the scan rate is systematically increased (B), the electrochemical waves increase in magnitude proportional to the square root of the scan rate (C), indicative of a diffusion limited process. The MOF catalytic performance is maximized at a starting layer thickness of 50 ALD cycles (D), which offers a balance of charge transport, mass transport, and active site density. The selectivity for each product is tested over a potential range of -0.5 to -0.9 vs. RHE (E) and reaches upwards of 76% for CO. The steady state current density for product quantification is illustrated in (F). In the low overpotential region, the Tafel slope of 165 mV/decade is closest to that of a one-electron reduction from CO2 to the CO2· rate limiting step (G).

The stability of the MOF catalyst was next tested over an extended period of time. In controlled potential electrolysis at -0.7 V vs. RHE in carbon dioxide-saturated aqueous bicarbonate buffer, the current density reached a stable state after several minutes and subsequently showed no sign of decrease for up to 7 h, generating 16 mL of CO (0.71 mmol, 5.25 cm^2 substrate) (Figure 3A, S8 and S9). The lower limit of the TON of the MOF catalyst is quantified through ICP analysis of the electrode after a testing and is measured to be 1400 assuming every cobalt atom is an electrochemically active site (Turnover frequency (TOF) = ~200 h^{-1}). The MOF largely retains its crystallinity after electrolysis and preservation of the framework was evidenced through the retention of the major powder X-ray diffraction (XRD) peaks (Figure 3B). Furthermore, scanning electron microscopy (SEM) analysis reveals the plate-like morphology has been retained (Figure 3C, D). *In situ* surface enhanced Raman spectroscopy (SERS) was utilized to confirm the integrity of the organic units throughout the catalytic process

(Figure S10). At each applied potential, the primary SERS peaks attributed to the porphyrin linker remain in the SERS spectrum.

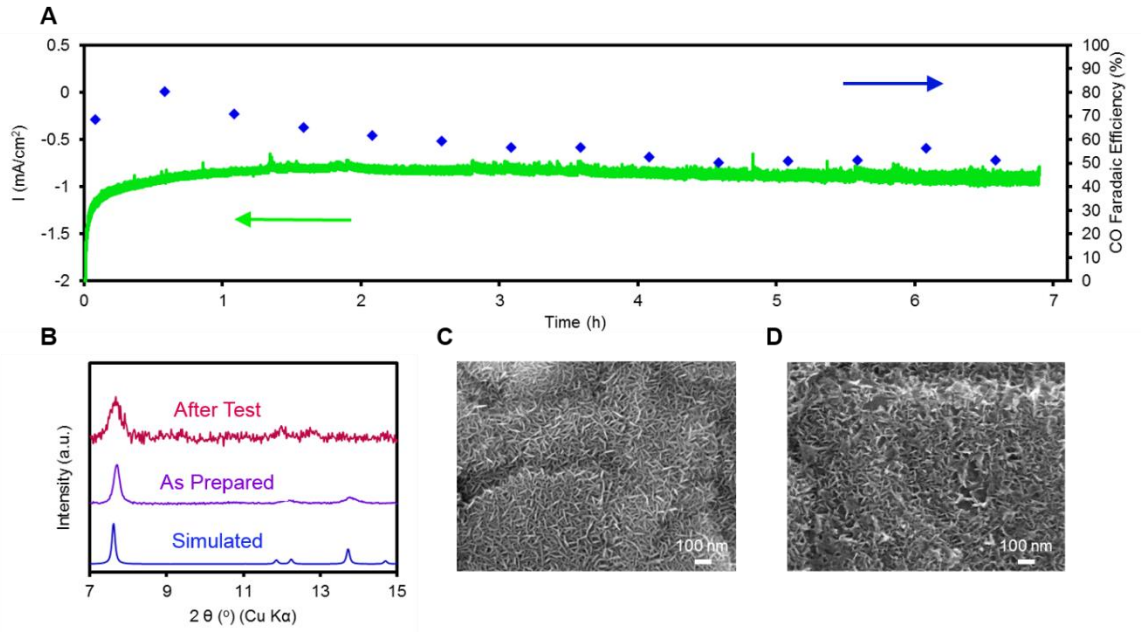

Figure 8.3. The stability of the MOF catalyst is evaluated through chronoamperometric measurements in combination with faradaic efficiency measurements (A). XRD analysis indicates that the MOF retains its crystalline structure after chronoamperometric measurement (B). SEM images of the MOF catalyst film before (C) and after electrolysis (D) reveal the retention of the plate-like morphology.

In situ spectroelectrochemical testing was next employed to ascertain the cobalt oxidation state under operating conditions. Such techniques have proven valuable for studying the electronic structure of porphyrins.[413,420-426] We grew the MOF on a transparent conductive fluorine-doped tin oxide (FTO) substrate and measured the film UV-Vis absorbance for a series of applied electrochemical potentials (Figure 4A). A typical absorption of the cobalt-metallated [$Al_2(OH)_2$TCPP-Co] MOF in open circuit states featured a Soret band ($S_0 \rightarrow S_2$) at 422 nm and a Q-band ($S_0 \rightarrow S_1$) at 530 nm. Upon applying increasingly negative potential (0 to -0.7 V vs. RHE) to the FTO/MOF electrode in a CO_2 saturated electrolyte, the Soret band at steady state conditions decreases in intensity at 422 nm and increases at 408 nm, with isosbestic points at 413 nm and 455 nm (Figure 4A). Plotting the difference spectra (Figure 4B) illustrates the band bleach and increase in the aforementioned spectral regions, which is subsequently quantified to deduce the formal redox potential ($E_{1/2}$) of the cobalt center in our system. The peak in the first derivative of the difference magnitude in these two wavelengths signified the formal reduction potential of the cobalt porphyrin unit in the MOF at -0.4 V vs. RHE (Figure 4C), which is consistent with the position of the first cathodic wave in the voltammogram trace. However, even at more positive potentials than -0.4 V vs. RHE, a fraction of the cobalt centers are still reduced and are likely to be participating in the catalytic conversion of CO_2 to CO.

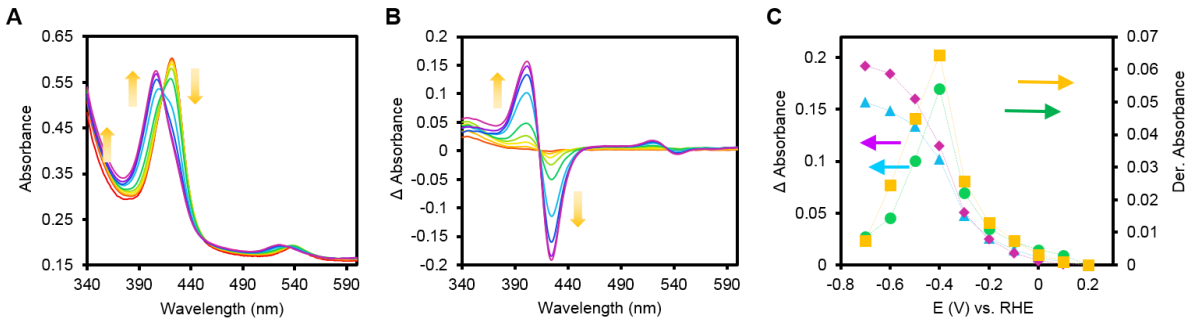

Figure 4. In situ spectroelectrochemical analysis reveals the oxidation state of the cobalt catalytic unit of the MOF under reaction conditions. Upon varying the voltage from 0.2 to -0.7 V vs. RHE, the Co(II) Soret band decreases at 422 nm and is accompanied by a Co(I) Soret band increase at 408 nm (A). This change is quantified (B) and plotted to elucidate a formal redox potential of the Co center, which is deemed to be at the peak of the first derivative (C) of the Co(II) bleach and Co(I) enhancement.

The buildup of a Co(I) species under operating conditions and a Tafel slope of 165 mV/decade indicates that the rate limiting step in our reaction mechanism may be either a CO_2 molecule adsorbing onto a Co(I) porphyrin coupled with a one electron reduction or a one electron reduction of a Co(I)-CO_2 adduct. We stress the importance of this spectroelectrochemical data in signifying that the majority of the cobalt centers are electrically connected to the electrode and are reduced to the catalytically active Co(I) state.

8.3 Concluding Remarks

We have demonstrated the applicability of MOF-integrated catalytic systems as modular platforms for the electrochemical reduction of aqueous CO2. This study represents the development of our first generation of MOF-based CO2 reduction electrocatalysts in which the active site, inorganic backbone, and thickness/loading were rationally chosen and the resulting MOF integrated onto a conductive support. The modularity of these systems yields many opportunities to further improve performance and open new directions in electrocatalyst development.

Parts of this section were published in: “Metal-Organic Frameworks for Electrocatalytic Reduction of Carbon Dioxide” **N. Kornienko***, Y. Zhao*, C. Kley, C. Zhu, D. Kim, S. Lin, C. Chang, O. Yaghi, P. Yang, *J. Am. Chem. Soc.*, 137, 14129 (2015)

9. Spectroscopic Elucidation of Picosecond Energy Transfer Pathways in Hybrid Inorganic-Biological Organisms for Solar-to-Chemical Production

9.0 Preface

In this chapter I departed from synthetic CO_2 reduction catalysts to investigate a hybrid inorganic-biological system capable of transforming carbon dioxide into acetate. As a final project, I chose to pursue this direction for multiple reasons 1) to develop a more generalized understanding of catalysis by probing biological catalytic systems, 2) extract key structure-function relationships and important lessons regarding efficient and selective CO_2 conversion from biological systems that may be transferred across to synthetic catalysts, and 3) explore the potential commercial large-scale viability of carbon dioxide reduction *via* a biological or hybrid approach.

9.1 Introduction

The sluggish kinetics governing the transduction of solar energy into chemical bonds through natural photosynthesis have hindered society's efforts to fully take advantage of this resource. Since the Industrial Revolution, we have temporarily sidestepped this limitation by tapping into large reserves of fixed carbonaceous energy to drive an exponential growth in manufacturing, agriculture, urbanization and ultimately population. However, the growing scarcity petrochemical feedstocks have issued forth a call for a return to photosynthesis - rather a new form of photosynthesis capable of keeping up with the rapid pace of modern society.[427] To accomplish this, inorganic semiconductor light harvesters now routinely surpass the energy efficiency of plants and algae. To this date, synthetic molecular or heterogeneous catalysts still struggle to replicate the complex carbon-carbon bond forming chemistry of biological catalytic pathways. Significant strides towards efficient, comprehensive solar-to-chemical production have been demonstrated through several inorganic-biological hybrid systems, combining inorganic semiconductor based light harvesters with microbial CO_2 reduction to value-added products.[428] Recently, we have reported the self-photosensitized hybrid acetogenic bacterium, *M. thermoacetica*-CdS, which photosynthetically produces acetic acid from CO_2 *via* bio-precipitated CdS nanoparticles with >80% quantum efficiency under low light conditions.[429]

Though electron transfer from abiotic semiconductors to these electrotrophic bacteria has been demonstrated across several genera, the mechanism remains in contention.[430] Spectroscopic investigations of bacterium-to-electrode anodic electron transfer in electrogenic microbial fuel cells have implicated cytochrome mediated mechanisms.[431] However, analogous studies of semiconductor-to-bacterium cathodic charge transfer in electrotrophic microorganisms have remained sparse. Electron transfer first to membrane bound or extracellular H_2ase to generate molecular H_2 as an intermediate followed by uptake into the native acetogenic Wood-Ljungdahl pathway (WLP) has been speculated or inferred.[432] Still, detailed spectroscopic characterization has remained elusive due to the difficulty of adapting previous techniques to solid electrode platforms. In contrast, our model system, *M. thermoacetica*-CdS, as a translucent colloidal suspension in which photoelectrons are generated by an optically addressable CdS nanoparticle, eliminates the need for solid electrodes and opaque electrical contacts, thereby enabling existing transmittance based spectroscopic techniques in uncovering the molecular basis of this charge

transfer mechanism (Fig. 9.1A). In this work, we present TAS and TRIR results correlated with biochemical activity to propose a model of the dynamics of inorganic-biological charge and energy transfer.

Upon photoexcitation of CdS, cysteine (Cys) oxidation to cystine (CySS) and protons quenches the valence band hole, while the conduction band electron may go to a number of different membrane bound proteins and solvated electron acceptors. Genomic mining, enzyme purification and characterization, as well as thermodynamic comparison of protein redox potentials have proposed several viable electron transfer pathways (Fig. 9.1B).[433] Electron transfer to membrane bound Ni-Fe H_2ases may play a significant role as H_2 production directly feeds into the first stages of the WLP. Demonstrations of direct electron transfer between metal chalcogenide nanoparticles and purified Fe-Fe H_2ases *in vitro* lend credibility to this pathway's existence in complex whole cells. Alternative pathways have been suggested, implicating charge transfer first to membrane bound cytochromes, ferredoxin (Fd), flavoproteins (Fp) and menaquinones (MK). While these pathways may generate reducing equivalents, implicitly these pathways must couple to generation of a proton gradient to allow ATP generation by ATPase. The generation of this proton motive force, either through the transmembrane Ech complex or simply through surface proximal Cys oxidation, may be crucial to electrotrophic behavior, as a related acetogen, *Acetobacterium woodii*, which instead utilizes a Na^+ motive force, is notably unable to engage in electrotrophic metabolism.[434]

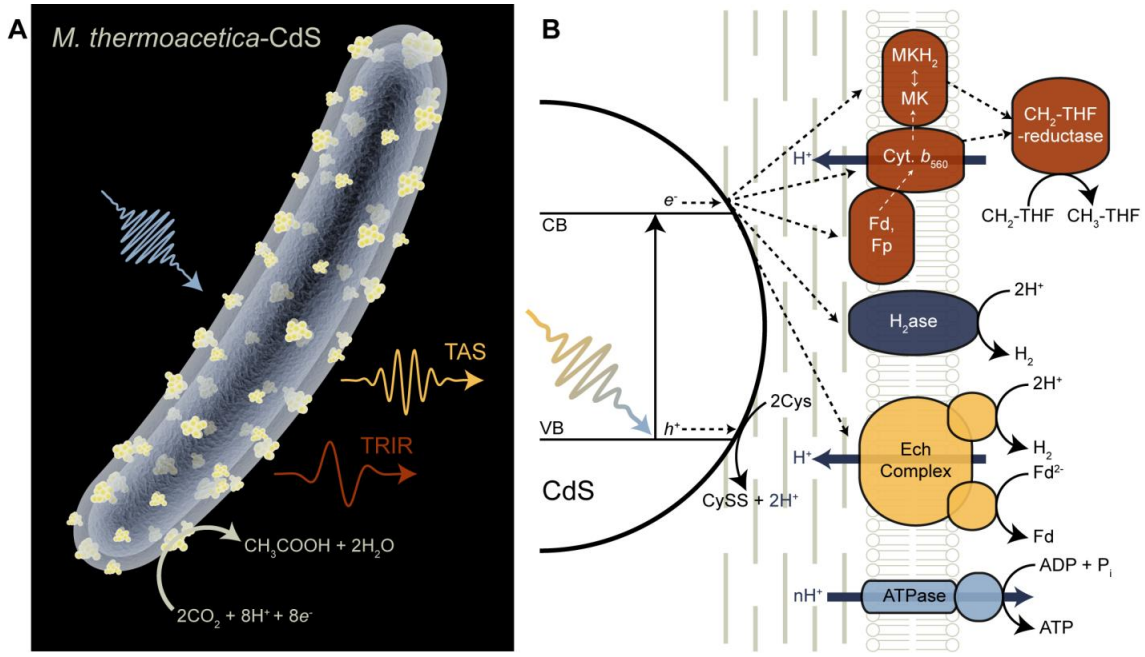

Figure 9.1. Schematic of *M. thermoacetica*-CdS Photosynthetic Charge Transfer. (A) Visible light excitation of optically addressable CdS photosensitizing nanoparticles enables photosynthetic acetic acid production from CO_2, as well as characterization by TAS and TRIR spectroscopy. (B) Potential electron transfer pathways in *M. thermoacetica*-CdS.

9.2 Results and Discussion

To investigate the possibility of H_2ase mediated electron transfer, *M. thermoacetica*-CdS was incubated from 0 to 48 hrs on H_2 (H_2:CO_2, 80:20, henceforth referred to as just H_2 incubated) or glucose (25 mM) to vary the expression and activity of H_2ase. Activity was assayed photometrically by standard benzyl viologen reduction in the presence of H_2 (Fig 9.2A).

Consistent with previous characterizations of *M. thermoacetica*, H_2 oxidation-benzyl viologen reduction activity increased under increasing incubation time under H_2 presumably through increased expression of H_2ase. Comparison of *M. thermoacetica*-CdS incubated for 24 hrs under glucose and H_2 showed H_2ase activity of $6.56\pm0.92\times10^{-15}$ (atm s cell)$^{-1}$ and $1.85\pm8.39\times10^{-17}$ (atm s cell)$^{-1}$, respectively.

To correlate these enzyme activities with CO_2-to-acetic acid performance, the same samples were subjected to simulated solar illumination (0.5% sun, AM1.5G) and analyzed for acetic acid production. Interestingly, during the initial 3 hrs of photosynthesis, the rate of CO_2 reduction was anti-correlated with H_2ase activity, with the 0 hrs sample demonstrating the highest activity (0.23 ± 0.02 mM hr^{-1}). The 24 hrs glucose sample produced acetic acid at a rate of 0.47 ± 0.15 mM hr^{-1}, one order of magnitude faster than the 24 hrs H_2 sample. However, at longer illumination times, H_2 incubated samples demonstrated the opposite trend. When averaged over 24 hrs of illumination, photosynthesis rates increased with increasing incubation time in H_2 (Fig. 9.2C). These contrasting results suggest two competing charge transfer mechanisms: a non-H_2ase mediated pathway dominant at short time scales (<3 hrs) and a H_2ase mediated pathway dominant at long time scales (~24 hrs).

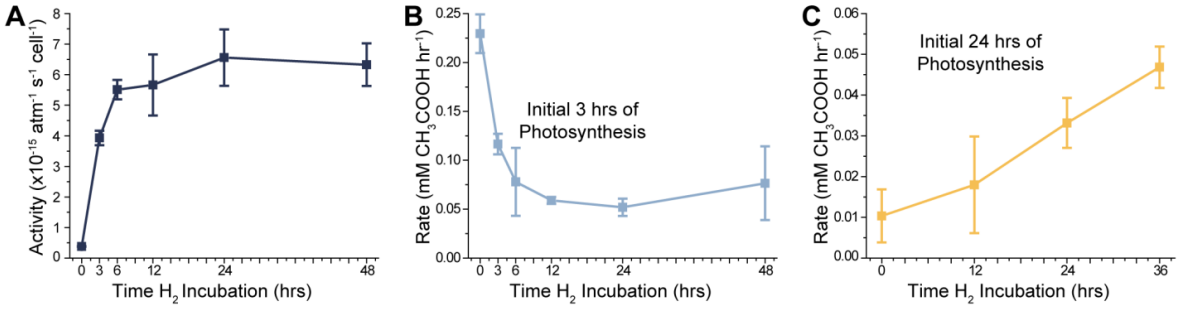

Figure 9.2. Biochemical Assays of *M. thermoacetica*-CdS. (A) H_2ase activity with varying incubation time under H_2. See Methods for details of quantification. (B) CO_2-to-acetic acid conversion rates averaged over the first 3 hrs of photosynthesis show a decreasing trend with increasing H_2 incubation time. (C) CO_2-to-acetic acid conversion rates averaged over the first 24 hrs of photosynthesis show an increasing trend with increasing H_2 incubation time. Error bars represent the standard deviation obtained from triplicate experiments.

To delve deeper into the molecular basis of these two mechanisms, we turned to time-resolved spectroscopic techniques for a dynamic understanding of the activity trends. TAS decay kinetics follow the rate of photogenerated electrons leaving CdS for various preparations of *M. thermoacetica*-CdS (Fig. 9.3). A transient bleach from 450-490 nm matches typical spectra observed with TAS measurements on CdS-electron acceptor systems. A control sample of *M. thermoacetica* without CdS did not display this transient absorption spectrum/kinetics. The spectrum of CdS alone decays much slower than CdS attached to the glucose and H_2 incubated

M. thermoacetica indicating that more rapid quenching may result from a proximal electron acceptor in the hybrid *M. thermoacetica*-CdS system. This result rules out the possibility that simple H_2 production at the CdS surface contributes significantly to solar-to-chemical production. Interestingly, the H_2 incubated *M. thermoacetica*-CdS displays even faster decay kinetics than the glucose analogue, correlating well with the higher H_2ase activity of H_2 incubated cells. These observations point to the presence of faster electron transfer to an acceptor site or more electron acceptors available in H_2 incubated bacteria.(24, 29) Fitting of the transient spectral data to a tri-exponential decay revealed three lifetimes: a fast component in the range of 3-9 ps (τ_1), a longer component in the range of 20-60 ps (τ_2) and an even longer component in the range of several 100 ps (τ_3). A multi-exponential decay unsurprisingly indicates several processes at play in the complex *M. thermoacetica*-CdS hybrids. Rapid decays, on the order of picoseconds, were previously measured with colloidal CdS that featured well positioned molecular acceptors with fast electron transfer behavior. However, previous studies of Fe-Fe H_2ase-colloidal nanorod CdS constructs reported TAS lifetimes in the range of 100 ns, significantly longer than the data presented here.(23, 24) The discrepancy may be attributed to the presence of surface ligands (not present in *M. thermoacetica*-CdS) which present a charge transfer barrier, as well as the relatively impaired functionality of purified enzymes under *in vitro* vs. *in vivo* conditions.[435]

The differences in lifetimes between cell-free CdS, H_2 incubated, and glucose incubated cells suggested the relative importance of H_2ase expression levels in charge transfer kinetics. To correlate with the above biochemical H_2ased activity (Fig. 9.2A), the TAS lifetimes of the H_2 incubated time series were measured (Fig. 9.3B, C). Both the fast τ_1, τ_2 and their weighted average show decreasing lifetimes with increasing H_2ase activity, suggesting that the fast charge transfer kinetics are due to an increase in H_2ase electron acceptor sites. Inhibition of the H_2ase active site (H-cluster) with CO did not significantly change the transient absorption kinetics, indicating that the first electron acceptor site can still function when the H-cluster is inhibited, similar to what has been seen in previous works, in which charge transfer initially proceeds through the Fe-S cluster chain rather than directly to the Ni-Fe active site.[436]

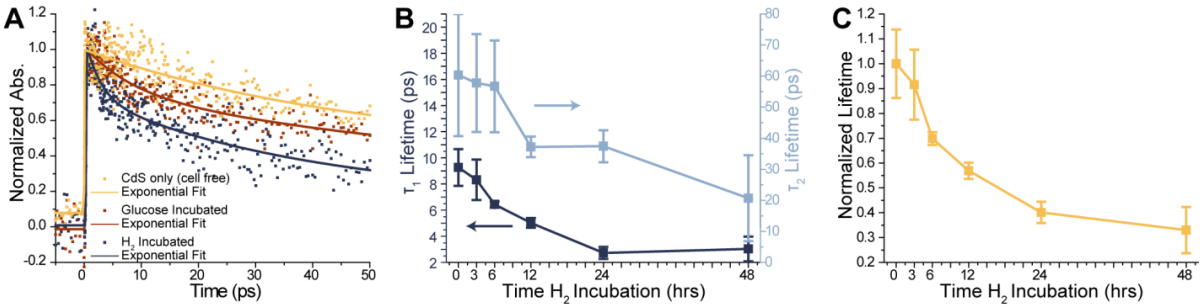

Figure 9.3. TAS of *M. thermoacetica*-CdS. (A) TAS plots of CdS only (cell-free), 24 hrs glucose incubated, and 24 hrs H_2 incubated. (B) Trends of exponential τ_1 and τ_2 lifetimes with increasing incubation time under H_2. (C) Weighted averages of the normalized τ_1 and τ_2 lifetimes with increasing incubation time under H_2. Error bars represent the standard error associated with the exponential fitting.

While kinetically efficient electron transfer to membrane bound H_2ase may explain the increasing photosynthesis rates at long time scales (Fig. 9.2C), we turned to TRIR to determine the molecular basis of the decreasing rates seen at short time scales (Fig 9.2B).

We observe spectral changes in the 1760-1880 cm^{-1} spectral window, roughly corresponding to the vibrational range of C, O, and N double and triple bonds (Fig. 9.4). The peaks decay on the same timescale as the TAS signal, giving further evidence that the picosecond electron transfer results from a molecular, rather than purely physical, process. While the complexity of the whole cell *M. thermoacetica*-CdS system renders unambiguous peak assignment beyond the scope of these initial results, careful construction of controls will yield valuable insight into the nature of these vibrational changes.

H_2 and glucose incubated samples yielded different TRIR spectral responses. While several bleach features in the range of 1760-1820 cm^{-1} on the picosecond time regime appeared for the H_2 incubated sample (Fig. 9.4A, S3)), in the same spectral window, glucose incubated samples showed long lived peak growth (Fig. 9.4B). These features may be indicative of H_2ase mediated charge transfer, with the differential response seen in glucose potentially representing an alternate pathway. In the region of 1810-1880 cm^{-1}, signal bleaches of similar time scales appear in both H_2 and glucose incubated samples, though their relative peak intensities differ qualitatively (Fig 9.4C,D). While the pair of bands at 1823 and 1827 cm^{-1} retain a roughly 1:1 ratio for the H_2 incubated sample, in the glucose incubated sample, the 1823 cm^{-1} feature does not grow in until 1-2 ps after the pump excitation, and decays back to zero faster than the 1827 cm^{-1}. Additionally, the single feature at 1842 cm^{-1} in the H_2 incubated sample blue shifts to 1845 cm^{-1} in the glucose incubated sample, temporarily forming a pair of peaks in the same region. Further assignment of these spectral responses will require further characterization of potentially knockout mutants in which protein expression is selectively deleted. Currently, we conclude that these spectral responses point towards different predominant charge transfer pathways in H_2 vs. glucose incubated samples.

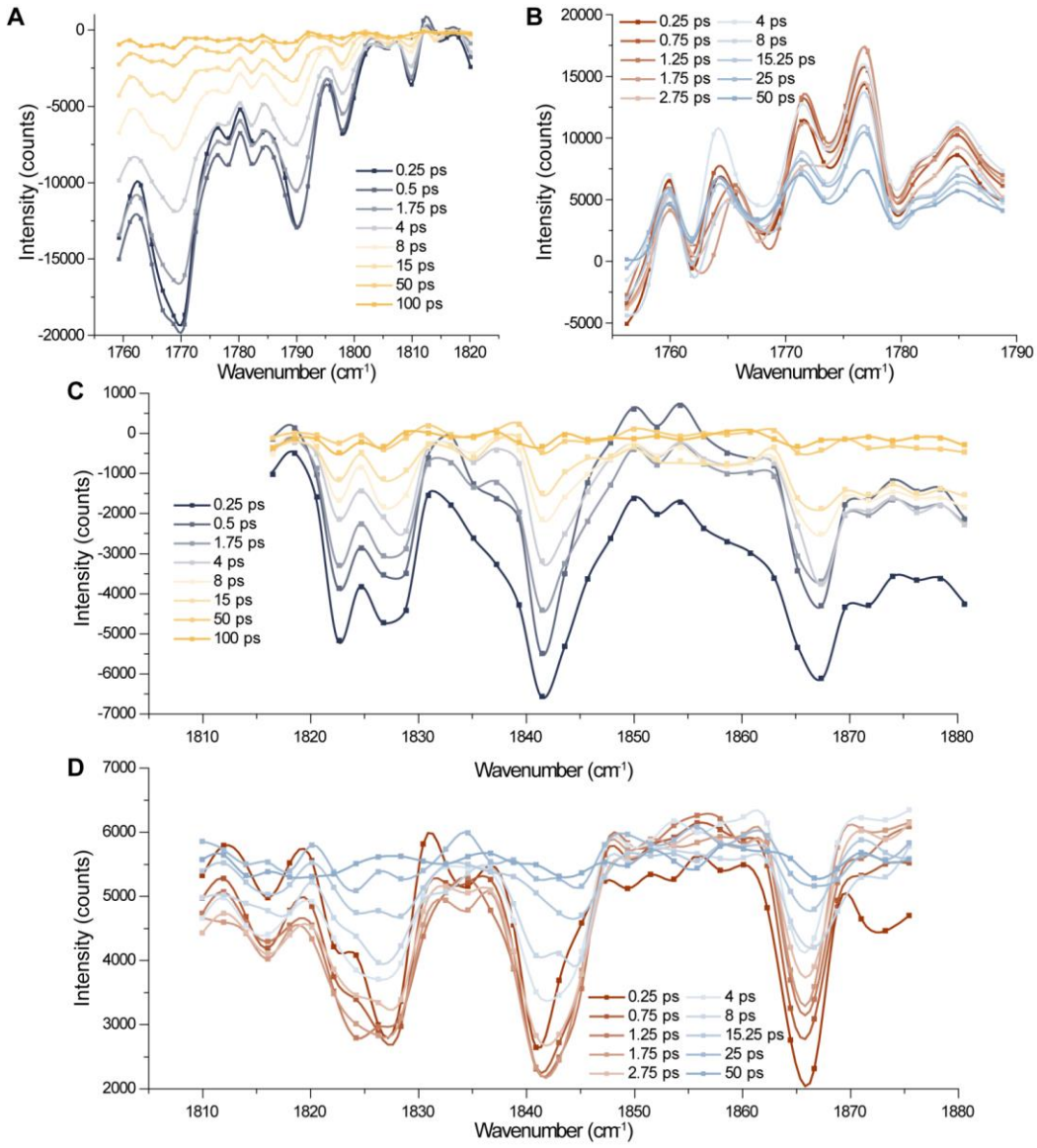

Figure 9.4. TRIR Spectra of *M. thermoacetica*-CdS. (A,C) TRIR of 24 hrs H_2 incubated *M. thermoacetica*-CdS showing bleaching of several peaks in the region of C, N, O double and triple bonds. (B,D) TRIR of 24 hrs glucose incubated *M. thermoacetica*-CdS.

Taken together, the biochemical, TAS and TRIR data suggest two competing pathways for electron transfer within *M. thermoacetica*-CdS (Fig. 9.5). Initially, low H_2ase expression favors electron injection to a membrane bound electron acceptor (Fd, Fp, cytochrome, MK) that generates a proton motive force for ATP generation, as well as directly reduces CH_2-THF for the final stages of the WLP. However, slower charge transfer leads to poor quantum efficiency, likely due to e^--h^+ recombination loss. Additionally, this pathway is unable to generate high energy reducing equivalents (H_2, NAD(P)H, Fd) needed for the first reductive steps of the WLP. As H_2ase expression increases, charge transfer kinetics favors electron transfer to a membrane bound H_2ase to generate molecular H_2. While this H_2ase mediated pathway may display higher

quantum efficiency, the higher photosynthetic rates only kick in once a significant concentration of extra(intra)cellular H_2 accumulates. This results in lower photosynthetic rates in the first 3 hrs with increasing H_2ase activity (electrons diverted from the non-H_2ase pathway), but eventually higher rates after 24 hrs. This H_2 then enters the normal WLP via oxidation by the HydABC complex. Since H_2 is the normal substrate of the WLP, both ATP and reducing equivalents are generated.

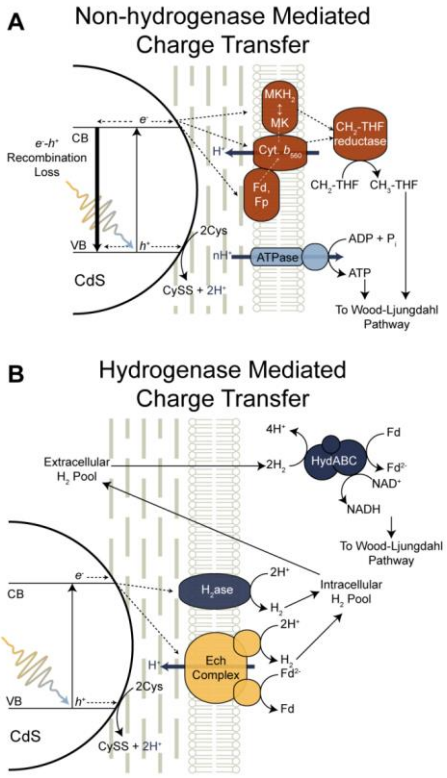

Figure 9.5. Proposed Dual Pathway of Charge and Energy Transfer in *M. thermoacetica*-CdS.(A) The proposed non-H_2ase mediated pathway predominant in glucose incubated cells, transiently faster during the initial 3 hrs of photosynthesis. (B) Membrane bound H_2ase mediated pathway dominant in H_2 incubated cells and photosynthetically faster at long time intervals.

9.3 Conclusion

In conclusion, the work here represents an initial experimental probe into the photosynthetic, electrotrophic behavior of *M. thermoacetica*-CdS. With the careful construction of controls, and mild, bio-compatible probing conditions, complex biological behaviors may be studied through conventional spectroscopic techniques. Increasing H_2ase activity was found to correlate with long term faster photosynthetic rates of acetic acid. Evidence provided by TAS and TRIR likewise supported the existence of a picosecond charge transfer pathway that correlated well with results from biochemical characterization. Our proposed two-pathway mechanism bears further investigation to probe more acutely the molecular and enzymatic basis of this biotic-abiotic charge transfer. Such insights will ultimately lead to a deeper understanding

of the burgeoning complex nexus of inorganic materials and biological systems, and provide a rational framework for the optimization and design of next generation solar-to-chemical systems.

Parts of this section to be published in: “Spectroscopic Elucidation of Picosecond Energy Transfer Pathways in Hybrid Inorganic-Biological Organisms for Solar-to-Chemical Production ” **N. Kornienko***, K. Sakimoto*, D. Herlihy, S. Nguyen, A. P. Alivisatos, C. B. Harris, A. Schwartzberg, P. Yang *In Preparation*

10. Conclusion

In summary, the work I have presented here represents significant advances in electrochemical and photoelectrochemical energy conversion. These developments consist of photocathode and electrocatalyst design, fabrication and testing.

With regards to photoelectrochemistry, we focused on developing a new generation of photocathodes to replace silicon, which produced insufficient photovoltage to couple with most photoanodes to drive the overall water splitting reaction (see figure 4.1 B). Therefore, I chose InP as a target material. The solution phase InP and InGaP growth developed in section 3 represents a promising strategy for scalable electrode processing and these materials featured high voltage, low cost, and band gap tunability, yet suffered from low photocurrent. Nevertheless, they represented promising candidates for future devices.

Next, I pursued a gas phase synthesis of InP on silicon substrates in section 4. InP nanowires grown on silicon are promising photocathode candidates because 1) InP has previously exhibited high photovoltage in photoelectrochemical cells, 2) the high surface area allows for enhanced photon absorption through light trapping effects and increased catalyst loading, 3) light absorption and carrier diffusion is orthogonalized and 4) growth on silicon instead of on InP substrates minimizes indium consumption and has potential for scale-up. During the initial synthetic development stages of this project, we discovered that under our growth conditions, the resulting material was faceted InP nanowires in the Wurtzite phase. Intrigued by this discovery, we performed a systematic study on the growth mechanism and factors affecting the InP growth rate and morphology. We subsequently developed the InP nanowires into p-type photocathodes by doping with zinc and carried out a detailed optical and electrochemical study on their resulting properties. Optimized photocathodes exhibited a significant improvement over typical silicon photocathode performance and enabled us to integrate our InP with a BiVO4 photoanode to achieve overall water splitting with 0.5% efficiency. While this efficiency is not yet high enough for scaled up commercial applications, our work presents a step in the right direction through the continual improvement of the photocathode component of the envisioned modular tandem water splitting system.

In addition to light absorber development, I aimed my efforts at catalyst innovation and the generation of structure function relationships. I consider the knowledge gained in section 5 to be a strong addition to the field of electro and photoelectrochemistry. Here, I examined a highly promising, yet poorly understood earth abundant hydrogen evolution catalyst alternative to Pt. This material consisted of an amorphous cobalt and sulfur and cobalt oxide containing film. However, under operating conditions, *in situ* Raman and X-ray absorption spectroscopic measurements revealed that the oxide dissolved away and the cobalt and sulfur components spontaneously crystallize into few-nuclei CoS_2-like clusters that presumably serve as high density active sites that are responsible for the high electrochemical activity of this material. The lessons learned here can be broadly applied to many amorphous catalysts that likely undergo spontaneous transformations into their active site only under reaction conditions. The methodology developed in this section enables further interrogation into such materials with state of the art *in situ* spectroscopic techniques.

Sections 6-8 deal with catalyst development for carbon dioxide reduction. This is a particularly difficult because of sluggish kinetics for this reaction and the fact that there are many possible products that can be generation, rendering catalytic selectivity and competition with hydrogen evolution additional hurdles that must be overcome. The primary goal in the field of CO2 reduction is to generate a catalyst system which features 1) selectivity for CO2 reduction over the hydrogen evolution reaction (HER), 2) stability over extended periods of time, 3) catalytic efficiency at low overpotential, and 4) a composition of earth abundant and cost effective materials.

To meet this goal, I first worked on homogeneous molecular catalysts in collaboration with the Chris Chang group in section 6. I explored the unique tunability at the molecular level that homogenous catalysts present and tested several analogues of a nickel-carbene compound. I discovered the beneficial improvements in electrochemical activity that stem from π conjugation, framework flexibility as well as carbine and amine donors on the molecular scaffold. Upon this initial demonstration, I combined the most promising molecular catalyst with a soluble light-absorbing dye to demonstrate a photocatalytic cycle.

The results in section 6 were promising but the molecular catalyst developed still suffered from issues of a lack of solubility I aqueous systems and the fact that only the molecular species next to the electrode were active in an electrochemical cell while the rest dissolved in the solution were not. To overcome this issue, we set out to develop a hybrid catalyst that retained the strengths of molecular tunability but also offered the advantages that heterogeneous catalysts presented, such as robustness and solubility not needed. A metal organic framework could serve this purpose as it is comprised of molecular tunable linkers held together within an inorganic backbone. These linkers could function as the catalytic active sites. In addition, every active site would be simultaneously accessible to the electrolyte yet also connected to the electron source/electrode.

Section 7 deals with the synthesis and design of thin films of MOFs that are eventually purposed to function as the electocatalysts. Because of the insulating nature of MOFs and hopping mechanism by which electrons travel through the framework, thin MOF films, on the order of tens of nanometers were needed. Hence, we developed a thin film growth method consisting of 1) deposition of metal oxide films *via* atomic layer deposition that served as the source for metal precursor and 2) conversion of these films into MOFs by addition of the appropriate linker and subjugation to microwave-assisted hydrothermal reaction conditions. This represented a powerful strategy to grow thin MOF films of multiple compositions directly on arbitrary substrates. With the aid of electron microscopy and X-ray scattering, we demonstrated that these MOF films were highly crystalline and exhibited preferred crystallographic orientations.

Section 8 consists of processing the MOF thin films into heterogeneous carbon dioxide catalysts. We designed our catalysts at the molecular, nanoscopic, and macroscopic scales. We chose a cobalt-metallated porphyrin as the linker because it was known to be an active molecular catalyst for the desired reaction. Next, we embedded this catalyst within a stable aluminum-oxide inorganic framework, with porosity large enough to allow for the diffusion of reactants in and

products out. This MOF was grown on stable, conductive and inert carbon electrodes. The resulting system featured high selectivity for carbon dioxide reduction to carbon monoxide and excellent stability. Electrochemical analysis revealed that the rate limiting step of the reaction was likely a one-electron reduction of carbon dioxide to a carbon dioxide anion. Furthermore, *in situ* spectroelectrochemical experiments elucidated that Co(1) built up under reaction conditions and served as the catalytically active site.

Section 9 looked a fundamentally different approach in utilizing CO_2 via a hybrid inorganic-biological system in which a CdS inorganic quantum dot functioned as a light absorbed that transferred photogenerated electrons to *m. thermoacetica* bacterium's internal metabolic pathways to eventually generate acetate. Here we demonstrated, using spectroscopic techniques, how multiple charge transfer pathways co-exist and the importance of rapidly capturing photogenerated electrons into energy carrying intermediates. Investigating how biological systems efficiently catalyst CO_2 reduction is vital towards extracting out useful structure-function relationships to improve our synthetic catalysts.

These projects are part of an encompassing effort to new materials and design rules for next generation solar to fuel conversing systems. Because such systems are composed of a multitude of synergistically functioning parts, advances in each component is helpful to have this technology reach eventual large scale commercial applications. The light absorbers and catalyst developed are parts of a virtuous cycle of design, synthesis and characterization. The promising advances can hopefully one day seen as key steps in the development and implementation of renewable energy technologies.

11 References

(1) Jacobson, M. Z.; Delucchi, M. A. *Energy Policy* **2011**, *39*, 1154.

(2) Vesborg, P. C.; Jaramillo, T. F. *RSC Advances* **2012**, *2*, 7933.

(3) Smalley, R. E. *Mrs Bulletin* **2005**, *30*, 412.

(4) Kalogirou, S. A. *Solar energy engineering: processes and systems*; Academic Press, 2013.

(5) Lewis, N. S.; Nocera, D. G. *Proceedings of the National Academy of Sciences* **2006**, *103*, 15729.

(6) Luo, J.; Im, J.-H.; Mayer, M. T.; Schreier, M.; Nazeeruddin, M. K.; Park, N.-G.; Tilley, S. D.; Fan, H. J.; Grätzel, M. *Science* **2014**, *345*, 1593.

(7) Lee, M. H.; Takei, K.; Zhang, J.; Kapadia, R.; Zheng, M.; Chen, Y. Z.; Nah, J.; Matthews, T. S.; Chueh, Y. L.; Ager, J. W. *Angewandte Chemie* **2012**, *124*, 10918.

(8) Reece, S. Y.; Hamel, J. A.; Sung, K.; Jarvi, T. D.; Esswein, A. J.; Pijpers, J. J.; Nocera, D. G. *Science* **2011**, *334*, 645.

(9) Khaselev, O.; Turner, J. A. *Science* **1998**, *280*, 425.

(10) Kumar, B.; Llorente, M.; Froehlich, J.; Dang, T.; Sathrum, A.; Kubiak, C. P. *Annual review of physical chemistry* **2012**, *63*, 541.

(11) Schwarz, H.; Dodson, R. *The Journal of Physical Chemistry* **1989**, *93*, 409.

(12) Adachi, S. In *Physical Properties of III-V Semiconductor Compounds*; Wiley & Co: 2005, p i.

(13) Adachi, S. In *Properties of Semiconductor Alloys*; John Wiley & Sons, Ltd: 2009, p i.

(14) Linnik, M.; Christou, A. *Physica B: Condensed Matter* **2002**, *318*, 140.

(15) Vandersmissen, R.; Merken, P. In *Advanced Optical Technologies* 2013; Vol. 2, p 241.

(16) Timmons, M. L.; Katsuyama, T.; Sillmon, R.; Bedair, S. M. In *Electron Devices Meeting, 1983 International* 1983; Vol. 29, p 692.

(17) Mascarenhas, A.; Zhang, Y. *Current Opinion in Solid State and Materials Science* **2001**, *5*, 253.

(18) Palankovski, V.; Schultheis, R.; Selberherr, S. *Electron Devices, IEEE Transactions on* **2001**, *48*, 1264.

(19) Strobl, G. F.; Bergunde, T.; Kostler, W.; Kern, R.; Meusel, M.; LaRoche, G.; Zimmermann, W.; Bett, A. W.; Dimroth, F.; Geens, W.; Taylor, S.; Fernandez, E.; Gerlach, L.; Signorini, C.; Hey, G. In *Photovoltaic Energy Conversion, Conference Record of the 2006 IEEE 4th World Conference* 2006; Vol. 2, p 1793.

(20) Onton, A.; Lorenz, M.; Reuter, W. *Journal of Applied Physics* **1971**, *42*, 3420.

(21) Onton, A.; Chicotka, R. *Physical Review B* **1971**, *4*, 1847.

(22) Lorenz, M.; Reuter, W.; Dumke, W.; Chicotka, R.; Pettit, G.; Woodall, J. *Applied Physics Letters* **1968**, *13*, 421.

(23) Prutskij, T.; Arencibia, P.; Brito-Orta, R. A.; Mintairov, A.; Kosel, T.; Merz, J. *Journal of Physics D: Applied Physics* **2004**, *37*, 1563.

(24) Dorn, A.; Allen, P. M.; Bawendi, M. G. *ACS nano* **2009**, *3*, 3260.

(25) Xiong, Y.; Xie, Y.; Li, Z.; Li, X.; Gao, S. *Chemistry-A European Journal* **2004**, *10*, 654.

(26) Davidson, F. M.; Wiacek, R.; Korgel, B. A. *Chemistry of Materials* **2005**, *17*, 230.

(27) Lim, T. H.; Ravi, S.; Bumby, C. W.; Etchegoin, P. G.; Tilley, R. D. *Journal of Materials Chemistry* **2009**, *19*, 4852.

(28) Trentler, T. J.; Hickman, K. M.; Goel, S. C.; Viano, A. M.; Gibbons, P. C.; Buhro, W. E. *Science* **1995**, *270*, 1791.

(29) Yu, H.; Li, J.; Loomis, R. A.; Wang, L.-W.; Buhro, W. E. *Nature Materials* **2003**, *2*, 517.

(30) Sun, J.; Liu, C.; Yang, P. *Journal of the American Chemical Society* **2011**, *133*, 19306.

(31) Liu, Z.; Sun, K.; Jian, W. B.; Xu, D.; Lin, Y. F.; Fang, J. *Chemistry-A European Journal* **2009**, *15*, 4546.

(32) Trentler, T. J.; Goel, S. C.; Hickman, K. M.; Viano, A. M.; Chiang, M. Y.; Beatty, A. M.; Gibbons, P. C.; Buhro, W. E. *Journal of the American Chemical Society* **1997**, *119*, 2172.

(33) Strupeit, T.; Klinke, C.; Kornowski, A.; Weller, H. *ACS nano* **2009**, *3*, 668.

(34) Banerjee, C.; Hughes, D. L.; Bochmann, M.; Nann, T. *Dalton Transactions* **2012**, *41*, 7244.

(35) Markowitz, P. D.; Zach, M. P.; Gibbons, P. C.; Penner, R.; Buhro, W. E. *Journal of the American Chemical Society* **2001**, *123*, 4502.

(36) Laocharoensuk, R.; Palaniappan, K.; Smith, N. A.; Dickerson, R. M.; Werder, D. J.; Baldwin, J. K.; Hollingsworth, J. A. *Nature nanotechnology* **2013**, *8*, 660.

(37) Zhu, G.; Xu, Z. *Journal of the American Chemical Society* **2010**, *133*, 148.

(38) Ouyang, L.; Maher, K. N.; Yu, C. L.; McCarty, J.; Park, H. *Journal of the American Chemical Society* **2007**, *129*, 133.

(39) Mićić, O.; Nozik, A. *Journal of luminescence* **1996**, *70*, 95.

(40) Fakhr, A.; Haddara, Y.; LaPierre, R. *Nanotechnology* **2010**, *21*, 165601.

(41) Svensson, C. P. T.; Mårtensson, T.; Trägårdh, J.; Larsson, C.; Rask, M.; Hessman, D.; Samuelson, L.; Ohlsson, J. *Nanotechnology* **2008**, *19*, 305201.

(42) Wallentin, J.; Poncela, L. B.; Jansson, A. M.; Mergenthaler, K.; Ek, M.; Jacobsson, D.; Wallenberg, L. R.; Deppert, K.; Samuelson, L.; Hessman, D. *Applied Physics Letters* **2012**, *100*, 251103.

(43) Kriegner, D.; Persson, J. M.; Etzelstorfer, T.; Jacobsson, D.; Wallentin, J.; Wagner, J. B.; Deppert, K.; Borgström, M.; Stangl, J. *Thin Solid Films* **2013**, *543*, 100.

(44) Ishizaka, F.; Ikejiri, K.; Tomioka, K.; Fukui, T. *Jpn J Appl Phys* **2013**, *52*, 04CH05.

(45) Willardson, R. K.; Beer, A. C. *Semiconductors & semimetals*; Academic Press, 1977; Vol. 12.

(46) Weast, R. C.; Astle, M. J.; Beyer, W. H. *CRC handbook of chemistry and physics*; CRC press Boca Raton, FL, 1988; Vol. 69.

(47) Vasil'ev, V.; Gachon, J.-C. *Inorganic materials* **2006**, *42*, 1171.

(48) Sirota, N.; Makovatskaya, I.; Rozov, V.; Vitkana, T. Z. *Chemical Bonds in Solids*; Springer, 1972; Vol. 2.

(49) Kriegner, D.; Wintersberger, E.; Kawaguchi, K.; Wallentin, J.; Borgström, M.; Stangl, J. *Nanotechnology* **2011**, *22*, 425704.

(50) Joyce, H. J.; Wong-Leung, J.; Gao, Q.; Tan, H. H.; Jagadish, C. *Nano letters* **2010**, *10*, 908.

(51) Assali, S.; Zardo, I.; Plissard, S.; Kriegner, D.; Verheijen, M.; Bauer, G.; Meijerink, A.; Belabbes, A.; Bechstedt, F.; Haverkort, J. *Nano Letters* **2013**, *13*, 1559.

(52) Glas, F.; Harmand, J.-C.; Patriarche, G. *Physical review letters* **2007**, *99*, 146101.
(53) Johansson, J.; Karlsson, L. S.; Dick, K. A.; Bolinsson, J.; Wacaser, B. A.; Deppert, K.; Samuelson, L. *Crystal Growth and Design* **2008**, *9*, 766.
(54) Johansson, J.; Dick, K.; Caroff, P.; Messing, M.; Bolinsson, J.; Deppert, K.; Samuelson, L. *The Journal of Physical Chemistry C* **2010**, *114*, 3837.
(55) Akimoto, K.; Emoto, T. *Journal of Physics: Condensed Matter* **2010**, *22*, 473001.
(56) Denton, A. R.; Ashcroft, N. W. *Physical Review A* **1991**, *43*, 3161.
(57) Fortuna, S. A.; Li, X. *Semiconductor Science and Technology* **2010**, *25*, 024005.
(58) Mattila, M.; Hakkarainen, T.; Jiang, H.; Kauppinen, E.; Lipsanen, H. *Nanotechnology* **2007**, *18*, 155301.
(59) Fetzer, C.; Lee, R.; Shurtleff, J.; Stringfellow, G.; Lee, S.; Seong, T. *Applied Physics Letters* **2000**, *76*, 1440.
(60) Song, J.; Ok, Y.-W.; Kim, J.; Lee, Y.; Seong, T.-Y. *Applied surface science* **2001**, *183*, 33.
(61) Philips, B.; Norman, A.; Seong, T.; Mahajan, S.; Booker, G.; Skowronski, M.; Harbison, J.; Keramidas, V. *Journal of Crystal Growth* **1994**, *140*, 249.
(62) Ahrenkiel, S.; Jones, K.; Matson, R.; Al-Jassim, M.; Zhang, Y.; Mascarenhas, A.; Friedman, D.; Arent, D.; Olson, J.; Hanna, M. In *MRS Proceedings*; Cambridge Univ Press: 1999; Vol. 583, p 243.
(63) González, L.; González, Y.; Dotor, M. L.; Martinez-Pastor, J. *Applied Physics Letters* **1998**, *72*, 2595.
(64) Nakaema, M. K. K.; Godoy, M. P. F.; Brasil, M. J. S. P.; Iikawa, F.; Silva, D.; Sacilotti, M.; Decobert, J.; Patriarche, G. *Journal of applied physics* **2005**, *98*.
(65) Kato, T.; Matsumoto, T.; Ishida, T. *Japanese journal of applied physics* **1988**, *27*, 983.
(66) Zachau, M.; Masselink, W. *Applied Physics Letters* **1992**, *60*, 2098.
(67) Abdelouhab, R.; Braunstein, R.; Bärner, K.; Rao, M.; Kroemer, H. *Journal of applied physics* **1989**, *66*, 787.
(68) Lucovsky, G.; Brodsky, M. H.; Chen, M. F.; Chicotka, R. J.; Ward, A. T. *Physical Review B* **1971**, *4*, 1945.
(69) Chang, I.; Mitra, S. *Physical Review* **1968**, *172*, 924.
(70) Cheong, H. M.; Mascarenhas, A.; Ernst, P.; Geng, C. *Physical Review B* **1997**, *56*, 1882.
(71) Alsina, F.; Mestres, N.; Pascual, J.; Geng, C.; Ernst, P.; Scholz, F. *Physical Review B* **1996**, *53*, 12994.
(72) Mintairov, A.; Merz, J.; Vlasov, A.; Vinokurov, D. *Semiconductor science and technology* **1998**, *13*, 1140.
(73) Erol, A. *Dilute III-V Nitride Semiconductors and Material Systems: Physics and Technology*; Springer, 2008; Vol. 105.
(74) Fu, L.; Chtchekine, D.; Gilliland, G.; Lee, H.; Hjalmarson, H.; Yu, J.; Craford, M.; Wolford, D. J. *Quantum Electronics, IEEE Journal of* **1997**, *33*, 1123.
(75) Holtz, M.; Sauncy, T.; Dallas, T.; Seon, M.; Palsule, C.; Gangopadhyay, S.; Massie, S. *physica status solidi (b)* **1996**, *198*, 199.
(76) Egerton, R. F. *Electron energy-loss spectroscopy in the electron microscope*; Springer, 1996; Vol. 233.
(77) Rafferty, B.; Brown, L. *Physical Review B* **1998**, *58*, 10326.

(78) Onton, A.; Chicotka, R. *Journal of Applied Physics* **1970**, *41*, 4205.
(79) Shah, J.; Miller, B.; DiGiovanni, A. *Journal of Applied Physics* **1972**, *43*, 3436.
(80) Rockett, A. *The materials science of semiconductors*; Springer, 2007.
(81) Vurgaftman, I.; Meyer, J.; Ram-Mohan, L. *Journal of applied physics* **2001**, *89*, 5815.
(82) Tachibana, Y.; Vayssieres, L.; Durrant, J. R. *Nature Photonics* **2012**, *6*, 511.
(83) Liu, C.; Tang, J.; Chen, H. M.; Liu, B.; Yang, P. *Nano letters* **2013**, *13*, 2989.
(84) Wang, Q.; Hisatomi, T.; Jia, Q.; Tokudome, H.; Zhong, M.; Wang, C.; Pan, Z.; Takata, T.; Nakabayashi, M.; Shibata, N. *Nat. Mater.* **2016**.
(85) Prévot, M. S.; Sivula, K. *The Journal of Physical Chemistry C* **2013**, *117*, 17879.
(86) Jiang, F.; Harada, T.; Kuang, Y.; Minegishi, T.; Domen, K.; Ikeda, S. *Journal of the American Chemical Society* **2015**, *137*, 13691.
(87) Lai, Y. H.; Palm, D. W.; Reisner, E. *Advanced Energy Materials* **2015**, *5*.
(88) Liu, B.; Wu, C.-H.; Miao, J.; Yang, P. *ACS nano* **2014**, *8*, 11739.
(89) Yang, H. B.; Miao, J.; Hung, S.-F.; Huo, F.; Chen, H. M.; Liu, B. *ACS nano* **2014**, *8*, 10403.
(90) Bornoz, P.; Abdi, F. F.; Tilley, S. D.; Dam, B.; Van De Krol, R.; Graetzel, M.; Sivula, K. *The Journal of Physical Chemistry C* **2014**, *118*, 16959.
(91) Jang, J.-W.; Du, C.; Ye, Y.; Lin, Y.; Yao, X.; Thorne, J.; Liu, E.; McMahon, G.; Zhu, J.; Javey, A. *Nature communications* **2015**, *6*.
(92) Seitz, L. C.; Chen, Z.; Forman, A. J.; Pinaud, B. A.; Benck, J. D.; Jaramillo, T. F. *ChemSusChem* **2014**, *7*, 1372.
(93) Liu, C.; Dasgupta, N. P.; Yang, P. *Chemistry of Materials* **2013**, *26*, 415.
(94) Walter, M. G.; Warren, E. L.; McKone, J. R.; Boettcher, S. W.; Mi, Q.; Santori, E. A.; Lewis, N. S. *Chem. Rev.* **2010**, *110*, 6446.
(95) Lin, Y.; Kapadia, R.; Yang, J.; Zheng, M.; Chen, K.; Hettick, M.; Yin, X.; Battaglia, C.; Sharp, I. D.; Ager, J. W. *The Journal of Physical Chemistry C* **2015**, *119*, 2308.
(96) Lee, M. H.; Takei, K.; Zhang, J.; Kapadia, R.; Zheng, M.; Chen, Y. Z.; Nah, J.; Matthews, T. S.; Chueh, Y. L.; Ager, J. W. *Angewandte Chemie* **2012**, *124*, 10918.
(97) Gao, L.; Cui, Y.; Wang, J.; Cavalli, A.; Standing, A.; Vu, T. T.; Verheijen, M. A.; Haverkort, J. E.; Bakkers, E. P.; Notten, P. H. *Nano Lett.* **2014**, *14*, 3715.
(98) Heller, A.; Miller, B.; Lewerenz, H.; Bachmann, K. *J. Am. Chem. Soc.* **1980**, *102*, 6555.
(99) Storm, K.; Halvardsson, F.; Heurlin, M.; Lindgren, D.; Gustafsson, A.; Wu, P. M.; Monemar, B.; Samuelson, L. *Nat. Nanotechnol.* **2012**, *7*, 718.
(100) Joyce, H. J.; Wong-Leung, J.; Yong, C.-K.; Docherty, C. J.; Paiman, S.; Gao, Q.; Tan, H. H.; Jagadish, C.; Lloyd-Hughes, J.; Herz, L. M. *Nano Lett.* **2012**, *12*, 5325.
(101) Garnett, E.; Yang, P. *Nano Lett.* **2010**, *10*, 1082.
(102) Kelzenberg, M. D.; Boettcher, S. W.; Petykiewicz, J. A.; Turner-Evans, D. B.; Putnam, M. C.; Warren, E. L.; Spurgeon, J. M.; Briggs, R. M.; Lewis, N. S.; Atwater, H. A. *Nat. Mater.* **2010**, *9*, 239.
(103) Kornienko, N.; Whitmore, D. D.; Yu, Y.; Leone, S. R.; Yang, P. *ACS nano* **2015**, *9*, 3951.
(104) Baek, J.; Allen, P. M.; Bawendi, M. G.; Jensen, K. F. *Angewandte Chemie* **2011**, *123*, 653.

(105) Trentler, T. J.; Hickman, K. M.; Goel, S. C.; Viano, A. M.; Gibbons, P. C.; Buhro, W. E. *Science* **1995**, *270*, 1791.

(106) Fanfair, D. D.; Korgel, B. A. *Crystal growth & design* **2005**, *5*, 1971.

(107) Yu, H.; Li, J.; Loomis, R. A.; Wang, L.-W.; Buhro, W. E. *Nature materials* **2003**, *2*, 517.

(108) Kapadia, R.; Yu, Z.; Hettick, M.; Xu, J.; Zheng, M. S.; Chen, C.-Y.; Balan, A. D.; Chrzan, D. C.; Javey, A. *Chemistry of Materials* **2014**, *26*, 1340.

(109) Kiriya, D.; Zheng, M.; Kapadia, R.; Zhang, J.; Hettick, M.; Yu, Z.; Takei, K.; Wang, H.-H. H.; Lobaccaro, P.; Javey, A. *Journal of Applied Physics* **2012**, *112*, 123102.

(110) Tang, C.; Bando, Y.; Liu, Z.; Golberg, D. *Chemical physics letters* **2003**, *376*, 676.

(111) Shen, G.; Bando, Y.; Liu, B.; Tang, C.; Golberg, D. *The Journal of Physical Chemistry B* **2006**, *110*, 20129.

(112) Gudiksen, M. S.; Wang, J.; Lieber, C. M. *The Journal of Physical Chemistry B* **2001**, *105*, 4062.

(113) Kobayashi, N. P.; Wang, S.-Y.; Santori, C.; Williams, R. S. *Applied Physics A* **2006**, *85*, 1.

(114) Mårtensson, T.; Svensson, C. P. T.; Wacaser, B. A.; Larsson, M. W.; Seifert, W.; Deppert, K.; Gustafsson, A.; Wallenberg, L. R.; Samuelson, L. *Nano Letters* **2004**, *4*, 1987.

(115) Mårtensson, T.; Carlberg, P.; Borgström, M.; Montelius, L.; Seifert, W.; Samuelson, L. *Nano Letters* **2004**, *4*, 699.

(116) Mohan, P.; Motohisa, J.; Fukui, T. *Nanotechnology* **2005**, *16*, 2903.

(117) Ren, F.; Ng, K. W.; Li, K.; Sun, H.; Chang-Hasnain, C. J. *Applied Physics Letters* **2013**, *102*, 012115.

(118) Moewe, M.; Chuang, L. C.; Dubrovskii, V. G.; Chang-Hasnain, C. *Journal of Applied Physics* **2008**, *104*, 044313.

(119) Gao, L.; Woo, R. L.; Liang, B.; Pozuelo, M.; Prikhodko, S.; Jackson, M.; Goel, N.; Hudait, M. K.; Huffaker, D. L.; Goorsky, M. S. *Nano letters* **2009**, *9*, 2223.

(120) Novotny, C. J.; Paul, K. *Applied Physics Letters* **2005**, *87*, 203111.

(121) Krishnamachari, U.; Borgstrom, M.; Ohlsson, B.; Panev, N.; Samuelson, L.; Seifert, W.; Larsson, M.; Wallenberg, L. *Applied Physics Letters* **2004**, *85*, 2077.

(122) Algra, R. E.; Verheijen, M. A.; Borgström, M. T.; Feiner, L.-F.; Immink, G.; van Enckevort, W. J.; Vlieg, E.; Bakkers, E. P. *Nature* **2008**, *456*, 369.

(123) Kitauchi, Y.; Kobayashi, Y.; Tomioka, K.; Hara, S.; Hiruma, K.; Fukui, T.; Motohisa, J. *Nano letters* **2010**, *10*, 1699.

(124) Woo, R. L.; Xiao, R.; Kobayashi, Y.; Gao, L.; Goel, N.; Hudait, M. K.; Mallouk, T. E.; Hicks, R. *Nano letters* **2008**, *8*, 4664.

(125) Woo, R. L.; Gao, L.; Goel, N.; Hudait, M. K.; Wang, K. L.; Kodambaka, S.; Hicks, R. F. *Nano letters* **2009**, *9*, 2207.

(126) Alouane, M. H.; Chauvin, N.; Khmissi, H.; Naji, K.; Ilahi, B.; Maaref, H.; Patriarche, G.; Gendry, M.; Bru-Chevallier, C. *Nanotechnology* **2013**, *24*, 035704.

(127) Ng, K. W.; Ko, W. S.; Lu, F.; Chang-Hasnain, C. J. *Nano letters* **2014**, *14*, 4757.

(128) Dubrovskii, V.; Sibirev, N. *Physical Review B* **2008**, *77*, 035414.

(129) Paiman, S.; Gao, Q.; Joyce, H.; Kim, Y.; Tan, H.; Jagadish, C.; Zhang, X.; Guo, Y.; Zou, J. *Journal of Physics D: Applied Physics* **2010**, *43*, 445402.

(130) Paiman, S.; Gao, Q.; Tan, H.; Jagadish, C.; Pemasiri, K.; Montazeri, M.; Jackson, H.; Smith, L.; Yarrison-Rice, J.; Zhang, X. *Nanotechnology* **2009**, *20*, 225606.

(131) Plante, M.; LaPierre, R. *Journal of crystal growth* **2006**, *286*, 394.

(132) Alatalo, M.; Nieminen, R.; Puska, M.; Seitsonen, A.; Virkkunen, R. *Physical Review B* **1993**, *47*, 6381.

(133) Mishra, R.; Restrepo, O. D.; Kumar, A.; Windl, W. *Journal of Materials Science* **2012**, *47*, 7482.

(134) Seitsonen, A.; Virkkunen, R.; Puska, M.; Nieminen, R. *Physical Review B* **1994**, *49*, 5253.

(135) Benzaquen, M.; Belache, B.; Blaauw, C.; Bruce, R. *Journal of Applied Physics* **1990**, *68*, 1694.

(136) Hettick, M.; Zheng, M.; Lin, Y.; Sutter-Fella, C. M.; Ager, J. W.; Javey, A. *The Journal of Physical Chemistry Letters* **2015**.

(137) Li, K.; Ng, K. W.; Tran, T.-T. D.; Sun, H.; Lu, F.; Chang-Hasnain, C. J. *Nano Lett.* **2015**, *15*, 7189.

(138) Li, K.; Sun, H.; Ren, F.; Ng, K. W.; Tran, T.-T. D.; Chen, R.; Chang-Hasnain, C. J. *Nano Lett.* **2013**, *14*, 183.

(139) Gao, Q.; Saxena, D.; Wang, F.; Fu, L.; Mokkapati, S.; Guo, Y.; Li, L.; Wong-Leung, J.; Caroff, P.; Tan, H. H. *Nano Lett.* **2014**, *14*, 5206.

(140) Tuin, G. L.; Borgström, M. T.; Trägårdh, J.; Ek, M.; Wallenberg, L. R.; Samuelson, L.; Pistol, M.-E. *Nano Res.* **2011**, *4*, 159.

(141) De, A.; Pryor, C. E. *Phys. Rev. B* **2010**, *81*, 155210.

(142) Moon, Y.; Si, S.; Yoon, E.; Kim, S. J. *Journal of applied physics* **1998**, *83*, 2261.

(143) Tuck, B.; Hooper, A. *Journal of Physics D: Applied Physics* **1975**, *8*, 1806.

(144) Chang, L.; Casey, H. *Solid-State Electronics* **1964**, *7*, 481.

(145) Schoonmaker, R. C.; Venkitaraman, A.; Lee, P. K. *The Journal of Physical Chemistry* **1967**, *71*, 2676.

(146) Chen, Z.; Dinh, H. N.; Miller, E. *Standards, Experimental Methods, and Protocols [Online]* **2013**.

(147) Cardon, F.; Gomes, W. *Journal of Physics D: Applied Physics* **1978**, *11*, L63.

(148) Dai, P.; Li, W.; Xie, J.; He, Y.; Thorne, J.; McMahon, G.; Zhan, J.; Wang, D. *Angewandte Chemie International Edition* **2014**, *53*, 13493.

(149) Munoz, A.; Heine, C.; Lublow, M.; Klemm, H.; Szabo, N.; Hannappel, T.; Lewerenz, H.-J. *ECS Journal of Solid State Science and Technology* **2013**, *2*, Q51.

(150) Shaner, M. R.; Fountaine, K. T.; Lewerenz, H.-J. *Applied Physics Letters* **2013**, *103*, 143905.

(151) Lee, M. H.; Takei, K.; Zhang, J.; Kapadia, R.; Zheng, M.; Chen, Y. Z.; Nah, J.; Matthews, T. S.; Chueh, Y. L.; Ager, J. W. *Angewandte Chemie International Edition* **2012**, *51*, 10760.

(152) Kim, T. W.; Choi, K.-S. *Science* **2014**, *343*, 990.

(153) Kanan, M. W.; Nocera, D. G. *Science* **2008**, *321*, 1072.

(154) Kuang, Y.; Jia, Q.; Nishiyama, H.; Yamada, T.; Kudo, A.; Domen, K. *Advanced Energy Materials* **2015**.

(155) Dresselhaus, M.; Thomas, I. *Nature* **2001**, *414*, 332.

(156) Faunce, T. A.; Lubitz, W.; Rutherford, W. A.; MacFarlane, D.; Moore, G. F.; Yang, P.; Nocera, D. G.; Moore, T. A.; Gregory, D. H.; Fukuzumi, S.; *al., e. Energy & Environmental Science* **2013**, *6*, 695.

(157) Turner, J. A. *Science* **2004**, *305*, 972.

(158) Merki, D.; Fierro, S.; Vrubel, H.; Hu, X. *Chemical Science* **2011**, *2*, 1262.

(159) Sun, Y.; Liu, C.; Grauer, D. C.; Yano, J.; Long, J. R.; Yang, P.; Chang, C. J. *Journal of the American Chemical Society* **2013**, *135*, 17699.

(160) Carim, A. I.; Saadi, F. H.; Soriaga, M. P.; Lewis, N. S. *Journal of Materials Chemistry A* **2014**, *2*, 13835.

(161) Jiang, N.; Bogoev, L.; Popova, M.; Gul, S.; Yano, J.; Sun, Y. *Journal of Materials Chemistry A* **2014**, *2*, 19407.

(162) Morales-Guio, C. G.; Hu, X. *Accounts of chemical research* **2014**, *47*, 2671.

(163) McEnaney, J. M.; Crompton, J. C.; Callejas, J. F.; Popczun, E. J.; Read, C. G.; Lewis, N. S.; Schaak, R. E. *Chemical Communications* **2014**, *50*, 11026.

(164) McEnaney, J. M.; Crompton, J. C.; Callejas, J. F.; Popczun, E. J.; Biacchi, A. J.; Lewis, N. S.; Schaak, R. E. *Chemistry of Materials* **2014**, *26*, 4826.

(165) Gorlin, Y.; Lassalle-Kaiser, B.; Benck, J. D.; Gul, S.; Webb, S. M.; Yachandra, V. K.; Yano, J.; Jaramillo, T. F. *Journal of the American Chemical Society* **2013**, *135*, 8525.

(166) Casalongue, H. G. S.; Benck, J. D.; Tsai, C.; Karlsson, R. K.; Kaya, S.; Ng, M. L.; Pettersson, L. G.; Abild-Pedersen, F.; Nørskov, J.; Ogasawara, H. *The Journal of Physical Chemistry C* **2014**, *118*, 29252.

(167) Benck, J. D.; Chen, Z.; Kuritzky, L. Y.; Forman, A. J.; Jaramillo, T. F. *ACS Catalysis* **2012**, *2*, 1916.

(168) Lassalle-Kaiser, B.; Merki, D.; Vrubel, H.; Gul, S.; Yachandra, V. K.; Hu, X.; Yano, J. *Journal of the American Chemical Society* **2015**.

(169) Bediako, D. K.; Lassalle-Kaiser, B.; Surendranath, Y.; Yano, J.; Yachandra, V. K.; Nocera, D. G. *Journal of the American Chemical Society* **2012**, *134*, 6801.

(170) Kanan, M. W.; Yano, J.; Surendranath, Y.; Dinca, M.; Yachandra, V. K.; Nocera, D. G. *Journal of the American Chemical Society* **2010**, *132*, 13692.

(171) Cui, C.; Jiang, S.; Tseung, A. *Journal of the Electrochemical Society* **1990**, *137*, 3418.

(172) Bajdich, M.; García-Mota, M. n.; Vojvodic, A.; Nørskov, J. K.; Bell, A. T. *Journal of the American Chemical Society* **2013**, *135*, 13521.

(173) Kötz, R.; Carlen, M. *Electrochimica Acta* **2000**, *45*, 2483.

(174) Trasatti, S.; Petrii, O. *Journal of Electroanalytical Chemistry* **1992**, *327*, 353.

(175) Colthup, N. *Introduction to Infrared and Raman Spectroscopy*; Elsevier, 2012.

(176) Long, D. A. *Raman Spectroscopy*; Elseiver, 1977.

(177) Tang, C.-W.; Wang, C.-B.; Chien, S.-H. *Thermochimica Acta* **2008**, *473*, 68.

(178) Yang, J.; Liu, H.; Martens, W. N.; Frost, R. L. *The Journal of Physical Chemistry C* **2009**, *114*, 111.

(179) Yeo, B. S.; Bell, A. T. *Journal of the American Chemical Society* **2011**, *133*, 5587.

(180) Mosselmans, J.; Pattrick, R.; Van der Laan, G.; Charnock, J.; Vaughan, D.; Henderson, C.; Garner, C. *Physics and Chemistry of Minerals* **1995**, *22*, 311.

(181) Binsted, N.; Cook, S. L.; Evans, J.; Greaves, G. N.; Price, R. J. *Journal of the American Chemical Society* **1987**, *109*, 3669.

(182) Sano, M. *Inorganic Chemistry* **1988**, *27*, 4249.
(183) Jiang, T.; Ellis, D. *Journal of materials research* **1996**, *11*, 2242.
(184) Charnock, J.; Henderson, C.; Mosselmans, J.; Pattrick, R. *Physics and chemistry of minerals* **1996**, *23*, 403.
(185) Nesvizhskii, A.; Rehr, J. *Journal of synchrotron radiation* **1999**, *6*, 315.
(186) De Groot, F.; Fuggle, J.; Thole, B.; Sawatzky, G. *Physical Review B* **1990**, *42*, 5459.
(187) Liu, H.; Guo, J.; Yin, Y.; Augustsson, A.; Dong, C.; Nordgren, J.; Chang, C.; Alivisatos, P.; Thornton, G.; Ogletree, D. F. *Nano Letters* **2007**, *7*, 1919.
(188) Van der Laan, G. *Journal of Physics: Condensed Matter* **1991**, *3*, 7443.
(189) Vura-Weis, J.; Jiang, C.-M.; Liu, C.; Gao, H.; Lucas, J. M.; de Groot, F. M.; Yang, P.; Alivisatos, A. P.; Leone, S. R. *The Journal of Physical Chemistry Letters* **2013**, *4*, 3667.
(190) Jiang, C.-M.; Baker, L. R.; Lucas, J. M.; Vura-Weis, J.; Alivisatos, A. P.; Leone, S. R. *The Journal of Physical Chemistry C* **2014**, *118*, 22774.
(191) Adam, R.; Grychtol, P.; Cramm, S.; Schneider, C. *Journal of Electron Spectroscopy and Related Phenomena* **2011**, *184*, 291.
(192) Jalilehvand, F. *Chemical Society Reviews* **2006**, *35*, 1256.
(193) Fleet, M. E.; Liu, X.; Harmer, S. L.; King, P. L. *The Canadian Mineralogist* **2005**, *43*, 1605.
(194) Farrell, S. P.; Fleet, M. E.; Stekhin, I. E.; Kravtsova, A.; Soldatov, A. V.; Liu, X. *American Mineralogist* **2002**, *87*, 1321.
(195) Lyapin, S.; Utyuzh, A.; Petrova, A.; Novikov, A.; Lograsso, T.; Stishov, S. *Journal of Physics: Condensed Matter* **2014**, *26*, 396001.
(196) Anastassakis, E.; Perry, C. *The Journal of Chemical Physics* **1976**, *64*, 3604.
(197) Zhu, L.; Susac, D.; Teo, M.; Wong, K.; Wong, P.; Parsons, R.; Bizzotto, D.; Mitchell, K.; Campbell, S. *Journal of Catalysis* **2008**, *258*, 235.
(198) Nakamura, K.; Fujitsuka, M.; Kitajima, M. *Physical Review B* **1990**, *41*, 12260.
(199) Gouadec, G.; Colomban, P. *Progress in Crystal Growth and Characterization of Materials* **2007**, *53*, 1.
(200) Gasanly, N. *Journal of Raman Spectroscopy* **2005**, *36*, 879.
(201) Sandström, M.; Jalilehvand, F.; Persson, I.; Gelius, U.; Frank, P.; Hall-Roth, I. *Nature* **2002**, *415*, 893.
(202) Mcneil, M. B.; Little, B. J. *Journal of the American Institute for Conservation* **1992**, *31*, 355.
(203) Oklejas, V.; Harris, J. M. *Applied spectroscopy* **2004**, *58*, 945.
(204) Roy, D.; Furtak, T. *The Journal of chemical physics* **1984**, *81*, 4168.
(205) Weaver, M. J.; Farquharson, S.; Tadayyoni, M. *The Journal of chemical physics* **1985**, *82*, 4867.
(206) Weaver, M. J.; Hupp, J. T.; Barz, F.; Gordon, J. G.; Philpott, M. R. *Journal of electroanalytical chemistry and interfacial electrochemistry* **1984**, *160*, 321.
(207) Corio, P.; Santos, P.; Brar, V.; Samsonidze, G. G.; Chou, S.; Dresselhaus, M. *Chemical physics letters* **2003**, *370*, 675.
(208) Rao, A. M.; Eklund, P.; Bandow, S.; Thess, A.; Smalley, R. E. *Nature* **1997**, *388*, 257.

(209) Han, X. X.; Köhler, C.; Kozuch, J.; Kuhlmann, U.; Paasche, L.; Sivanesan, A.; Weidinger, I. M.; Hildebrandt, P. *Small* **2013**, *9*, 4175.

(210) Pavlov, N.; Galkin, V.; Nekrasov, I.; Kurmaev, E. *Physics of the Solid State* **2009**, *51*, 2207.

(211) Bullett, D. *Journal of Physics C: solid state physics* **1982**, *15*, 6163.

(212) Flory, M.; McLamarrah, S.; Ziurys, L. *The Journal of chemical physics* **2005**, *123*, 164312.

(213) Muro, T.; Kimura, A.; Iwasaki, T.; Ueda, S.; Imada, S.; Matsushita, T.; Sekiyama, A.; Susaki, T.; Mamiya, K.; Harada, T. *Journal of Electron Spectroscopy and Related Phenomena* **1998**, *88*, 361.

(214) Zhao, G.; Callaway, J.; Hayashibara, M. *Physical Review B* **1993**, *48*, 15781.

(215) Miyauchi, H.; Koide, T.; Shidara, T.; Nakajima, N.; Kawabe, H.; Yamaguchi, K.; Fujimori, A.; Fukutani, H.; Iio, K.; Miyadai, T. *Journal of Electron Spectroscopy and Related Phenomena* **1996**, *78*, 255.

(216) Koningsberger, D.; Prins, R. *X-Ray Absorption: Principles, Applications, Techniques of EXAFS, SEXAFS, and XANES*; Wiley Interscience, 1988; Vol. 92.

(217) Teo, B.; Joy, D. *EXAFS Spectroscopy: Techniques and Applications*; Springer US, 1981.

(218) van Bokhoven, J.; Ressler, T.; de Groot, F. M.; Knop-Gericke, A. *of Book: In-Situ Spectroscopy of Catalysts*; American Scientific Publishers, 2004.

(219) Castner, D. G.; Watson, P. R.; Chan, I. Y. *Journal of Physical Chemistry* **1990**, *94*, 819.

(220) Paul, J.-F.; Payen, E. *The Journal of Physical Chemistry B* **2003**, *107*, 4057.

(221) Tye, C. T.; Smith, K. J. *Topics in catalysis* **2006**, *37*, 129.

(222) Lauritsen, J.; Nyberg, M.; Nørskov, J. K.; Clausen, B.; Topsøe, H.; Lægsgaard, E.; Besenbacher, F. *Journal of Catalysis* **2004**, *224*, 94.

(223) Garcia, M. V.; Lindner, J.; Sachdev, A.; Schwank, J. *Journal of Catalysis* **1989**, *119*, 388.

(224) Bouwens, S.; Van Veen, J.; Koningsberger, D.; De Beer, V.; Prins, R. *The Journal of Physical Chemistry* **1991**, *95*, 123.

(225) Tan, A.; Harris, S. *Inorganic chemistry* **1998**, *37*, 2215.

(226) Ho, T. C. *Catalysis letters* **2003**, *89*, 21.

(227) Jaramillo, T. F.; Jørgensen, K. P.; Bonde, J.; Nielsen, J. H.; Horch, S.; Chorkendorff, I. *Science* **2007**, *317*, 100.

(228) Kibsgaard, J.; Chen, Z.; Reinecke, B. N.; Jaramillo, T. F. *Nature materials* **2012**, *11*, 963.

(229) Chen, Z.; Cummins, D.; Reinecke, B. N.; Clark, E.; Sunkara, M. K.; Jaramillo, T. F. *Nano Letters* **2011**, *11*, 4168.

(230) Kibsgaard, J.; Jaramillo, T. F.; Besenbacher, F. *Nature chemistry* **2014**, *6*, 248.

(231) Kong, D.; Wang, H.; Cha, J. J.; Pasta, M.; Koski, K. J.; Yao, J.; Cui, Y. *Nano Letters* **2013**, *13*, 1341.

(232) Kong, D.; Cha, J. J.; Wang, H.; Lee, H. R.; Cui, Y. *Energy & Environmental Science* **2013**, *6*, 3553.

(233) Cabán-Acevedo, M.; Kaiser, N. S.; English, C. R.; Liang, D.; Thompson, B. J.; Chen, H.-E.; Czech, K. J.; Wright, J. C.; Hamers, R. J.; Jin, S. *Journal of the American Chemical Society* **2014**, *136*, 17163.

(234) Faber, M. S.; Lukowski, M. A.; Ding, Q.; Kaiser, N. S.; Jin, S. *The Journal of Physical Chemistry C* **2014**, *118*, 21347.

(235) Faber, M. S.; Dziedzic, R.; Lukowski, M. A.; Kaiser, N. S.; Ding, Q.; Jin, S. *Journal of the American Chemical Society* **2014**, *136*, 10053.

(236) Benson, E. E.; Kubiak, C. P.; Sathrum, A. J.; Smieja, J. M. *Chemical Society Reviews* **2009**, *38*, 89.

(237) Centi, G.; Perathoner, S. *Catalysis Today* **2009**, *148*, 191.

(238) Rakowski Dubois, M.; Dubois, D. L. *Accounts of Chemical Research* **2009**, *42*, 1974.

(239) Cokoja, M.; Bruckmeier, C.; Rieger, B.; Herrmann, W. A.; Kühn, F. E. *Angewandte Chemie International Edition* **2011**, *50*, 8510.

(240) Finn, C.; Schnittger, S.; Yellowlees, L. J.; Love, J. B. *Chemical Communications* **2012**, *48*, 1392.

(241) Schneider, J.; Jia, H.; Muckerman, J. T.; Fujita, E. *Chemical Society Reviews* **2012**, *41*, 2036.

(242) Costentin, C.; Robert, M.; Savéant, J.-M. *Chem. Soc. Rev.* **2013**, *42*, 2423.

(243) Collin, J.; Sauvage, J. *Coordination Chemistry Reviews* **1989**, *93*, 245.

(244) Jessop, P. G.; Ikariya, T.; Noyori, R. *Chemical Reviews* **1995**, *95*, 259.

(245) Appel, A. M.; Bercaw, J. E.; Bocarsly, A. B.; Dobbek, H.; DuBois, D. L.; Dupuis, M.; Ferry, J. G.; Fujita, E.; Hille, R.; Kenis, P. J. *Chemical reviews* **2013**, *113*, 6621.

(246) Windle, C. D.; Perutz, R. N. *Coordination Chemistry Reviews* **2012**, *256*, 2562.

(247) Izumi, Y. *Coordination Chemistry Reviews* **2013**, *257*, 171.

(248) Hagfeldt, A.; Grätzel, M. *Accounts of Chemical Research* **2000**, *33*, 269.

(249) Alstrum-Acevedo, J. H.; Brennaman, M. K.; Meyer, T. J. *Inorganic Chemistry* **2005**, *44*, 6802.

(250) Hochbaum, A. I.; Yang, P. *Chemical reviews* **2009**, *110*, 527.

(251) Gust, D.; Moore, T. A.; Moore, A. L. *Accounts of chemical research* **2009**, *42*, 1890.

(252) Sato, S.; Arai, T.; Morikawa, T.; Uemura, K.; Suzuki, T. M.; Tanaka, H.; Kajino, T. *Journal of the American Chemical Society* **2011**, *133*, 15240.

(253) Sun, L.; Hammarström, L.; Åkermark, B.; Styring, S. *Chemical Society Reviews* **2001**, *30*, 36.

(254) Gray, H. B. *Nature chemistry* **2009**, *1*, 7.

(255) Oh, Y.; Hu, X. *Chemical Society Reviews* **2013**, *42*, 2253.

(256) Kang, P.; Meyer, T. J.; Brookhart, M. *Chemical Science* **2013**, *4*, 3497.

(257) Inoue, T.; Fujishima, A.; Konishi, S.; Honda, K. *Nature* **1979**, *277*, 637.

(258) Aurian-Blajeni, B.; Halmann, M.; Manassen, J. *Solar Energy Materials* **1983**, *8*, 425.

(259) Yoneyama, H.; Sugimura, K.; Kuwabata, S. *Journal of electroanalytical chemistry and interfacial electrochemistry* **1988**, *249*, 143.

(260) Ghadimkhani, G.; de Tacconi, N. R.; Chanmanee, W.; Janaky, C.; Rajeshwar, K. *Chemical Communications* **2013**, *49*, 1297.

(261) Lin, W.; Han, H.; Frei, H. *The Journal of Physical Chemistry B* **2004**, *108*, 18269.

(262) Lin, W.; Frei, H. *Journal of the American Chemical Society* **2005**, *127*, 1610.

(263) Lin, W.; Frei, H. *Comptes Rendus Chimie* **2006**, *9*, 207.

(264) Petit, J.-P.; Chartier, P.; Beley, M.; Deville, J.-P. *Journal of Electroanalytical Chemistry and Interfacial Electrochemistry* **1989**, *269*, 267.

(265) Barton, E. E.; Rampulla, D. M.; Bocarsly, A. B. *Journal of the American Chemical Society* **2008**, *130*, 6342.

(266) Kumar, B.; Smieja, J. M.; Kubiak, C. P. *The Journal of Physical Chemistry C* **2010**, *114*, 14220.

(267) Hori, Y.; Wakebe, H.; Tsukamoto, T.; Koga, O. *Electrochimica Acta* **1994**, *39*, 1833.

(268) Kuhl, K. P.; Cave, E. R.; Abram, D. N.; Jaramillo, T. F. *Energy & Environmental Science* **2012**, *5*, 7050.

(269) Li, C. W.; Kanan, M. W. *Journal of the American Chemical Society* **2012**, *134*, 7231.

(270) Chen, Y.; Kanan, M. W. *J. Am. Chem. Soc.* **2012**, *134*, 1986.

(271) Chen, Y.; Li, C. W.; Kanan, M. W. *Journal of the American Chemical Society* **2012**, *134*, 19969.

(272) DiMeglio, J. L.; Rosenthal, J. *Journal of the American Chemical Society* **2013**, *135*, 8798.

(273) Tornow, C. E.; Thorson, M. R.; Ma, S.; Gewirth, A. A.; Kenis, P. J. *Journal of the American Chemical Society* **2012**, *134*, 19520.

(274) Fisher, B. J.; Eisenberg, R. *Journal of the American Chemical Society* **1980**, *102*, 7361.

(275) Beley, M.; Collin, J. P.; Ruppert, R.; Sauvage, J. P. *Journal of the American Chemical Society* **1986**, *108*, 7461.

(276) Collin, J. P.; Jouaiti, A.; Sauvage, J. P. *Inorganic Chemistry* **1988**, *27*, 1986.

(277) Balazs, G. B.; Anson, F. C. *Journal of Electroanalytical Chemistry* **1992**, *322*, 325.

(278) Fujita, E.; Haff, J.; Sanzenbacher, R.; Elias, H. *Inorganic Chemistry* **1994**, *33*, 4627.

(279) Ogata, T.; Yanagida, S.; Brunschwig, B. S.; Fujita, E. *Journal of the American Chemical Society* **1995**, *117*, 6708.

(280) Froehlich, J. D.; Kubiak, C. P. *Inorganic chemistry* **2012**, *51*, 3932.

(281) Ishida, H.; Tanaka, K.; Tanaka, T. *Organometallics* **1987**, *6*, 181.

(282) Bolinger, C. M.; Story, N.; Sullivan, B. P.; Meyer, T. J. *Inorganic Chemistry* **1988**, *27*, 4582.

(283) Hurrell, H.; Mogstad, A.; Usifer, D.; Potts, K.; Abruna, H. *Inorganic Chemistry* **1989**, *28*, 1080.

(284) Pugh, J. R.; Bruce, M. R.; Sullivan, B. P.; Meyer, T. J. *Inorganic chemistry* **1991**, *30*, 86.

(285) Arana, C.; Yan, S.; Keshavarz-K, M.; Potts, K.; Abruna, H. *Inorganic Chemistry* **1992**, *31*, 3680.

(286) Smieja, J. M.; Kubiak, C. P. *Inorganic chemistry* **2010**, *49*, 9283.

(287) Chen, Z.; Chen, C.; Weinberg, D. R.; Kang, P.; Concepcion, J. J.; Harrison, D. P.; Brookhart, M. S.; Meyer, T. J. *Chemical Communications* **2011**, *47*, 12607.

(288) Bourrez, M.; Molton, F.; Chardon-Noblat, S.; Deronzier, A. *Angewandte Chemie* **2011**, *123*, 10077.

(289) Wang, W.-H.; Hull, J. F.; Muckerman, J. T.; Fujita, E.; Himeda, Y. *Energy & Environmental Science* **2012**, *5*, 7923.

(290) Hammouche, M.; Lexa, D.; Momenteau, M.; Saveant, J. M. *Journal of the American Chemical Society* **1991**, *113*, 8455.

(291) Bhugun, I.; Lexa, D.; Savéant, J.-M. *Journal of the American Chemical Society* **1996**, *118*, 1769.

(292) Cheng, Z.; Al Zaki, A.; Hui, J. Z.; Muzykantov, V. R.; Tsourkas, A. *Science* **2012**, *338*, 903.

(293) Grodkowski, J.; Neta, P.; Fujita, E.; Mahammed, A.; Simkhovich, L.; Gross, Z. *The Journal of Physical Chemistry A* **2002**, *106*, 4772.

(294) Lieber, C. M.; Lewis, N. S. *Journal of the American Chemical Society* **1984**, *106*, 5033.

(295) Kapusta, S.; Hackerman, N. *Journal of The Electrochemical Society* **1984**, *131*, 1511.

(296) Ratliff, K. S.; Lentz, R. E.; Kubiak, C. P. *Organometallics* **1992**, *11*, 1986.

(297) Haines, R. J.; Wittrig, R. E.; Kubiak, C. P. *Inorganic Chemistry* **1994**, *33*, 4723.

(298) Simón-Manso, E.; Kubiak, C. P. *Organometallics* **2005**, *24*, 96.

(299) Kang, P.; Cheng, C.; Chen, Z.; Schauer, C. K.; Meyer, T. J.; Brookhart, M. *Journal of the American Chemical Society* **2012**, *134*, 5500.

(300) Angamuthu, R.; Byers, P.; Lutz, M.; Spek, A. L.; Bouwman, E. *Science* **2010**, *327*, 313.

(301) Rail, M. D.; Berben, L. A. *Journal of the American Chemical Society* **2011**, *133*, 18577.

(302) Seshadri, G.; Lin, C.; Bocarsly, A. B. *J. Electroanal. Chem.* **1994**, *372*, 145.

(303) Barton Cole, E.; Lakkaraju, P. S.; Rampulla, D. M.; Morris, A. J.; Abelev, E.; Bocarsly, A. B. *Journal of the American Chemical Society* **2010**, *132*, 11539.

(304) Morris, A. J.; McGibbon, R. T.; Bocarsly, A. B. *ChemSusChem* **2011**, *4*, 191.

(305) Richardson, R. D.; Holland, E. J.; Carpenter, B. K. *Nature Chemistry* **2011**, *3*, 301.

(306) Thoi, V. S.; Chang, C. J. *Chemical Communications* **2011**, *47*, 6578.

(307) Kirch, M.; Lehn, J. M.; Sauvage, J. P. *Helvetica Chimica Acta* **1979**, *62*, 1345.

(308) Hori, H.; Johnson, F. P.; Koike, K.; Ishitani, O.; Ibusuki, T. *Journal of Photochemistry and Photobiology A: Chemistry* **1996**, *96*, 171.

(309) Matsuoka, S.; Yamamoto, K.; Ogata, T.; Kusaba, M.; Nakashima, N.; Fujita, E.; Yanagida, S. *Journal of the American Chemical Society* **1993**, *115*, 601.

(310) Dhanasekaran, T.; Grodkowski, J.; Neta, P.; Hambright, P.; Fujita, E. *The Journal of Physical Chemistry A* **1999**, *103*, 7742.

(311) Ogata, T.; Yamamoto, Y.; Wada, Y.; Murakoshi, K.; Kusaba, M.; Nakashima, N.; Ishida, A.; Takamuku, S.; Yanagida, S. *The Journal of Physical Chemistry* **1995**, *99*, 11916.

(312) Hawecker, J.; Lehn, J.-M.; Ziessel, R. *Journal of the Chemical Society, Chemical Communications* **1985**, 56.

(313) Craig, C. A.; Spreer, L. O.; Otvos, J. W.; Calvin, M. *Journal of Physical Chemistry* **1990**, *94*, 7957.

(314) Grant, J. L.; Goswami, K.; Spreer, L. O.; Otvos, J. W.; Calvin, M. *Journal of the Chemical Society, Dalton Transactions* **1987**, 2105.

(315) Ziessel, R.; Hawecker, J.; Lehn, J. M. *Helvetica chimica acta* **1986**, *69*, 1065.

(316) Hirose, T.; Maeno, Y.; Himeda, Y. *Journal of Molecular Catalysis A: Chemical* **2003**, *193*, 27.

(317) Gholamkhass, B.; Mametsuka, H.; Koike, K.; Tanabe, T.; Furue, M.; Ishitani, O. *Inorganic chemistry* **2005**, *44*, 2326.

(318) Bian, Z.-Y.; Sumi, K.; Furue, M.; Sato, S.; Koike, K.; Ishitani, O. *Inorganic chemistry* **2008**, *47*, 10801.

(319) Tamaki, Y.; Morimoto, T.; Koike, K.; Ishitani, O. *Proceedings of the National Academy of Sciences* **2012**, *109*, 15673.

(320) Sato, S.; Morikawa, T.; Kajino, T.; Ishitani, O. *Angewandte Chemie* **2013**, *125*, 1022.

(321) Gueymard, C.; Myers, D.; Emery, K. *Solar energy* **2002**, *73*, 443.

(322) Gueymard, C. A. *Solar energy* **2004**, *76*, 423.

(323) Costamagna, J.; Ferraudi, G.; Canales, J.; Vargas, J. *Coordination chemistry reviews* **1996**, *148*, 221.

(324) Nicewicz, D. A.; MacMillan, D. W. *Science* **2008**, *322*, 77.

(325) Narayanam, J. M.; Stephenson, C. R. *Chemical Society Reviews* **2011**, *40*, 102.

(326) Ischay, M. A.; Yoon, T. P. *European Journal of Organic Chemistry* **2012**, *2012*, 3359.

(327) Hamilton, D. S.; Nicewicz, D. A. *Journal of the American Chemical Society* **2012**, *134*, 18577.

(328) Creutz, S. E.; Lotito, K. J.; Fu, G. C.; Peters, J. C. *Science* **2012**, *338*, 647.

(329) Prier, C. K.; Rankic, D. A.; MacMillan, D. W. *Chemical reviews* **2013**, *113*, 5322.

(330) Huang, Y.-Z.; Miao, H.; Zhang, Q.-H.; Chen, C.; Xu, J. *Catalysis Letters* **2008**, *122*, 344.

(331) Xi, Z.; Zhang, X.; Chen, W.; Fu, S.; Wang, D. *Organometallics* **2007**, *26*, 6636.

(332) Zhou, Y.; Xi, Z.; Chen, W.; Wang, D. *Organometallics* **2008**, *27*, 5911.

(333) Gu, S.; Chen, W. *Organometallics* **2009**, *28*, 909.

(334) Kapturkiewicz, A.; Angulo, G. *Dalton Transactions* **2003**, 3907.

(335) Shih, H.-W.; Vander Wal, M. N.; Grange, R. L.; MacMillan, D. W. *Journal of the American Chemical Society* **2010**, *132*, 13600.

(336) Irvine, J.; Eggins, B.; Grimshaw, J. *Solar energy* **1990**, *45*, 27.

(337) Johne, P.; Kisch, H. *Journal of Photochemistry and photobiology A: Chemistry* **1997**, *111*, 223.

(338) Murov, S. L.; Carmichael, I.; Hug, G. L. *Handbook of photochemistry*; CRC Press, 1993.

(339) Khan, M. T.; Mirza, S. A.; Bajaj, H. *Reaction Kinetics and Catalysis Letters* **1987**, *33*, 67.

(340) Shekhah, O.; Wang, H.; Strunskus, T.; Cyganik, P.; Zacher, D.; Fischer, R.; Wöll, C. *Langmuir : the ACS journal of surfaces and colloids* **2007**, *23*, 7440.

(341) Kreno, L.; Hupp, J.; Van Duyne, R. *Analytical chemistry* **2010**, *82*, 8042.

(342) Kouta, S.; Yuki, F.; Kazuki, S. *Chemistry of Materials* **2011**, *23*.

(343) Nian, L.; Yan, Y.; Judy, J. C.; Matthew, T. M.; Yu, H.; Yi, C. *Nano Research* **2011**, *5*.

(344) Lu, G.; Li, S.; Guo, Z.; Farha, O.; Hauser, B.; Qi, X.; Wang, Y.; Wang, X.; Han, S.; Liu, X.; DuChene, J.; Zhang, H.; Zhang, Q.; Chen, X.; Ma, J.; Loo, S.; Wei, W.; Yang, Y.; Hupp, J.; Huo, F. *Nature chemistry* **2012**, *4*, 310.

(345) Reboul, J.; Furukawa, S.; Horike, N.; Tsotsalas, M.; Hirai, K.; Uehara, H.; Kondo, M.; Louvain, N.; Sakata, O.; Kitagawa, S. *Nat. Mater.* **2012**, *11*, 717.

(346) He, L.; Liu, Y.; Liu, J.; Xiong, Y.; Zheng, J.; Liu, Y.; Tang, Z. *Angewandte Chemie (International ed. in English)* **2013**, *52*, 3741.

(347) Khaletskaya, K.; Reboul, J.; Meilikhov, M.; Nakahama, M.; Diring, S.; Tsujimoto, M.; Isoda, S.; Kim, F.; Kamei, K.-i.; Fischer, R.; Kitagawa, S.; Furukawa, S. *Journal of the American Chemical Society* **2013**, *135*, 10998.

(348) Shengye, J.; Ho-Jin, S.; Omar, K. F.; Gary, P. W.; Joseph, T. H. *Journal of the American Chemical Society* **2013**, *135*.

(349) So, M.; Jin, S.; Son, H.-J.; Wiederrecht, G.; Farha, O.; Hupp, J. *Journal of the American Chemical Society* **2013**, *135*, 15698.

(350) Wen-wen, Z.; Qin, K.; Jian-zhang, Z.; Xiang-jian, K.; Zhao-xiong, X.; Lan-sun, Z. *Journal of the American Chemical Society* **2013**, *135*.

(351) Hu, P.; Zhuang, J.; Chou, L.-Y.; Lee, H.; Ling, X.; Chuang, Y.-C.; Tsung, C.-K. *Journal of the American Chemical Society* **2014**, *136*, 10561.

(352) Hu, Y.; Liao, J.; Wang, D.; Li, G. *Analytical chemistry* **2014**, *86*, 3955.

(353) Lauren, E. K.; Nathan, G. G.; Omar, K. F.; Joseph, T. H.; Richard, P. V. D. *The Analyst* **2014**, *139*.

(354) Tao, A.; Sinsermsuksakul, P.; Yang, P. *Angewandte Chemie (International ed. in English)* **2006**, *45*, 4597.

(355) Tao, A.; Sinsermsuksakul, P.; Yang, P. *Nature nanotechnology* **2007**, *2*, 435.

(356) Tao, A.; Ceperley, D.; Sinsermsuksakul, P.; Neureuther, A.; Yang, P. *Nano letters* **2008**, *8*, 4033.

(357) Fateeva, A.; Chater, P.; Ireland, C.; Tahir, A.; Khimyak, Y.; Wiper, P.; Darwent, J.; Rosseinsky, M. *Angewandte Chemie (International ed. in English)* **2012**, *51*, 7440.

(358) Rosen, E.; Buonsanti, R.; Llordes, A.; Sawvel, A.; Milliron, D.; Helms, B. *Angewandte Chemie (International ed. in English)* **2012**, *51*, 684.

(359) Vlckova, B. M., Pavel a; Slmonova, Jindriska; Cermakova, Katerina; *The Journal of Physical Chemistry* **1993**, *97*.

(360) Li, X.; Czernuszewicz, R.; Kincaid…, J. *Journal of Physical …* **1990**.

(361) Kong, X.; Deng, H.; Yan, F.; Kim, J.; Swisher, J.; Smit, B.; Yaghi, O.; Reimer, J. *Science (New York, N.Y.)* **2013**, *341*, 882.

(362) Aresta, M.; Dibenedetto, A.; Angelini, A. *Chemical reviews* **2013**, *114*, 1709.

(363) Quadrelli, E. A.; Centi, G.; Duplan, J. L.; Perathoner, S. *ChemSusChem* **2011**, *4*, 1194.

(364) Yaghi, O. M.; Li, H.; Davis, C.; Richardson, D.; Groy, T. L. *Accounts of Chemical Research* **1998**, *31*, 474.

(365) Yaghi, O. M.; O'Keeffe, M.; Ockwig, N. W.; Chae, H. K.; Eddaoudi, M.; Kim, J. *Nature* **2003**, *423*, 705.

(366) Lee, J.; Farha, O. K.; Roberts, J.; Scheidt, K. A.; Nguyen, S. T.; Hupp, J. T. *Chemical Society Reviews* **2009**, *38*, 1450.

(367) Zhou, H.-C.; Long, J. R.; Yaghi, O. M. *Chemical reviews* **2012**, *112*, 673.

(368) Kuppler, R. J.; Timmons, D. J.; Fang, Q.-R.; Li, J.-R.; Makal, T. A.; Young, M. D.; Yuan, D.; Zhao, D.; Zhuang, W.; Zhou, H.-C. *Coordination Chemistry Reviews* **2009**, *253*, 3042.

(369) Wang, Z.; Cohen, S. M. *Chemical Society Reviews* **2009**, *38*, 1315.

(370) An, J.; Rosi, N. L. *Journal of the American Chemical Society* **2010**, *132*, 5578.

(371) Kitagawa, S.; Kitaura, R.; Noro, S. i. *Angewandte Chemie International Edition* **2004**, *43*, 2334.

(372) Hori, Y.; Murata, A.; Takahashi, R. *Journal of the Chemical Society, Faraday Transactions 1: Physical Chemistry in Condensed Phases* **1989**, *85*, 2309.

(373) DeWulf, D. W.; Jin, T.; Bard, A. J. *J. Electrochem. Soc.* **1989**, *136*, 1686.

(374) Rosen, B. A.; Salehi-Khojin, A.; Thorson, M. R.; Zhu, W.; Whipple, D. T.; Kenis, P. J.; Masel, R. I. *Science* **2011**, *334*, 643.

(375) Hoshi, N.; Kato, M.; Hori, Y. *Journal of Electroanalytical Chemistry* **1997**, *440*, 283.

(376) Kim, D.; Resasco, J.; Yu, Y.; Asiri, A. M.; Yang, P. *Nature communications* **2014**, *5*, 4948.

(377) Zhu, W.; Michalsky, R.; Metin, O. n.; Lv, H.; Guo, S.; Wright, C. J.; Sun, X.; Peterson, A. A.; Sun, S. *Journal of the American Chemical Society* **2013**, *135*, 16833.

(378) Zhu, W.; Zhang, Y.-J.; Zhang, H.; Lv, H.; Li, Q.; Michalsky, R.; Peterson, A. A.; Sun, S. *Journal of the American Chemical Society* **2014**, *136*, 16132.

(379) Zhang, S.; Kang, P.; Meyer, T. J. *Journal of the American Chemical Society* **2014**, *136*, 1734.

(380) Manthiram, K.; Beberwyck, B. J.; Alivisatos, A. P. *Journal of the American Chemical Society* **2014**, *136*, 13319.

(381) Gao, D.; Zhou, H.; Wang, J.; Miao, S.; Yang, F.; Wang, G.; Wang, J.; Bao, X. *Journal of the American Chemical Society* **2015**, *137*, 4288.

(382) Medina-Ramos, J.; Pupillo, R. C.; Keane, T. P.; DiMeglio, J. L.; Rosenthal, J. *J. Am. Chem. Soc.* **2015**.

(383) Medina-Ramos, J.; DiMeglio, J. L.; Rosenthal, J. *Journal of the American Chemical Society* **2014**, *136*, 8361.

(384) Lu, Q.; Rosen, J.; Zhou, Y.; Hutchings, G. S.; Kimmel, Y. C.; Chen, J. G.; Jiao, F. *Nature communications* **2014**, *5*, 3242.

(385) Asadi, M.; Kumar, B.; Behranginia, A.; Rosen, B. A.; Baskin, A.; Repnin, N.; Pisasale, D.; Phillips, P.; Zhu, W.; Haasch, R. *Nature communications* **2014**, *5*, 4470.

(386) Wu, J.; Yadav, R. M.; Liu, M.; Sharma, P. P.; Tiwary, C. S.; Ma, L.; Zou, X.; Zhou, X.-D.; Yakobson, B. I.; Lou, J. *ACS Nano* **2015**.

(387) Zhang, S.; Kang, P.; Ubnoske, S.; Brennaman, M. K.; Song, N.; House, R. L.; Glass, J. T.; Meyer, T. J. *Journal of the American Chemical Society* **2014**, *136*, 7845.

(388) Kumar, B.; Asadi, M.; Pisasale, D.; Sinha-Ray, S.; Rosen, B. A.; Haasch, R.; Abiade, J.; Yarin, A. L.; Salehi-Khojin, A. *Nature communications* **2013**, *4*, 2819.

(389) Liu, C.; Gallagher, J. J.; Sakimoto, K. K.; Nichols, E. M.; Chang, C. J.; Chang, M. C.; Yang, P. *Nano Lett.* **2015**.

(390) Torella, J. P.; Gagliardi, C. J.; Chen, J. S.; Bediako, D. K.; Colón, B.; Way, J. C.; Silver, P. A.; Nocera, D. G. *Proceedings of the National Academy of Sciences* **2015**, *112*, 2337.

(391) Reda, T.; Plugge, C. M.; Abram, N. J.; Hirst, J. *Proceedings of the National Academy of Sciences* **2008**, *105*, 10654.

(392) Schuchmann, K.; Müller, V. *Science* **2013**, *342*, 1382.

(393) Costentin, C.; Drouet, S.; Robert, M.; Savéant, J.-M. *Science* **2012**, *338*, 90.

(394) Smieja, J. M.; Sampson, M. D.; Grice, K. A.; Benson, E. E.; Froehlich, J. D.; Kubiak, C. P. *Inorganic chemistry* **2013**, *52*, 2484.

(395) Thoi, V. S.; Kornienko, N.; Margarit, C. G.; Yang, P.; Chang, C. J. *Journal of the American Chemical Society* **2013**, *135*, 14413.

(396) Schneider, J.; Jia, H.; Kobiro, K.; Cabelli, D. E.; Muckerman, J. T.; Fujita, E. *Energy & Environmental Science* **2012**, *5*, 9502.

(397) Lacy, D. C.; McCrory, C. C.; Peters, J. C. *Inorganic chemistry* **2014**, *53*, 4980.

(398) Wang, C.; Xie, Z.; deKrafft, K. E.; Lin, W. *Journal of the American Chemical Society* **2011**, *133*, 13445.

(399) Fu, Y.; Sun, D.; Chen, Y.; Huang, R.; Ding, Z.; Fu, X.; Li, Z. *Angewandte Chemie* **2012**, *124*, 3420.

(400) Liu, Y.; Yang, Y.; Sun, Q.; Wang, Z.; Huang, B.; Dai, Y.; Qin, X.; Zhang, X. *ACS applied materials & interfaces* **2013**, *5*, 7654.

(401) Hinogami, R.; Yotsuhashi, S.; Deguchi, M.; Zenitani, Y.; Hashiba, H.; Yamada, Y. *ECS Electrochem. Lett.* **2012**, *1*, H17.

(402) Kumar, R. S.; Kumar, S. S.; Kulandainathan, M. A. *Electrochemistry Communications* **2012**, *25*, 70.

(403) García, M.; Aguirre, M. J.; Canzi, G.; Kubiak, C. P.; Ohlbaum, M.; Isaacs, M. *Electrochimica Acta* **2014**, *115*, 146.

(404) Bonin, J.; Chaussemier, M.; Robert, M.; Routier, M. *ChemCatChem* **2014**, *6*, 3200.

(405) Leung, K.; Nielsen, I. M.; Sai, N.; Medforth, C.; Shelnutt, J. A. *The Journal of Physical Chemistry A* **2010**, *114*, 10174.

(406) Behar, D.; Dhanasekaran, T.; Neta, P.; Hosten, C.; Ejeh, D.; Hambright, P.; Fujita, E. *The Journal of Physical Chemistry A* **1998**, *102*, 2870.

(407) RamÍRez, G.; Lucero, M.; Riquelme, A.; Villagrán, M.; Costamagna, J.; Trollund, E.; Aguirre, M. J. *Journal of Coordination Chemistry* **2004**, *57*, 249.

(408) Zhao, Y.; Kornienko, N.; Liu, Z.; Zhu, C.; Asahina, S.; Kuo, T.-R.; Bao, W.; Xie, C.; Hexemer, A.; Terasaki, O.; Yang, P.; Yaghi, O. M. *Journal of the American Chemical Society* **2015**, *137*, 2199.

(409) The Journal of Physical Chemistry CTripkovic, V.; Vanin, M.; Karamad, M.; Björketun, M. r. E.; Jacobsen, K. W.; Thygesen, K. S.; Rossmeisl, J. *The Journal of Physical Chemistry C* **2013**, *117*, 9187.

(410) Qiao, J.; Liu, Y.; Hong, F.; Zhang, J. *Chem. Soc. Rev.* **2014**, *43*, 631.

(411) Bard, A. J.; Faulkner, L. R. *Electrochemical methods: fundamentals and applications*; Wiley New York, 1980.

(412) Newman, J.; Thomas-Alyea, K. E. *Electrochemical systems*; John Wiley & Sons: Hoboken, New Jersey, 2012.

(413) Ahrenholtz, S. R.; Epley, C. C.; Morris, A. J. *Journal of the American Chemical Society* **2014**, *136*, 2464.

(414) Russell, P.; Kovac, N.; Srinivasan, S.; Steinberg, M. *Journal of the Electrochemical Society* **1977**, *124*, 1329.

(415) Bandi, A. *Journal of the Electrochemical Society* **1990**, *137*, 2157.

(416) Hatsukade, T.; Kuhl, K. P.; Cave, E. R.; Abram, D. N.; Jaramillo, T. F. *Physical Chemistry Chemical Physics* **2014**, *16*, 13814.

(417) Riquelme, M.; Isaacs, M.; Lucero, M.; Trollund, E.; Aguirre, M.; Canales, J. *Journal of the Chilean Chemical Society* **2003**, *48*, 89.

(418) Najafi, M.; Sadeghi, M. *ECS Electrochemistry Letters* **2013**, *2*, H5.

(419) Manbeck, G. F.; Fujita, E. *Journal of Porphyrins and Phthalocyanines* **2015**, *19*, 45.

(420) Kung, C.-W.; Chang, T.-H.; Chou, L.-Y.; Hupp, J. T.; Farha, O. K.; Ho, K.-C. *Chem. Commun.* **2015**.

(421) Kadish, K.; Boisselier-Cocolios, B.; Coutsolelos, A.; Mitaine, P.; Guilard, R. *Inorganic Chemistry* **1985**, *24*, 4521.

(422) Wei, Z.; Ryan, M. D. *Inorganica Chimica Acta* **2001**, *314*, 49.

(423) Lin, X.; Boisselier-Cocolios, B.; Kadish, K. *Inorg. Chem.* **1986**, *25*, 3242.

(424) Quezada, D.; Honores, J.; García, M.; Armijo, F.; Isaacs, M. *New Journal of Chemistry* **2014**, *38*, 3606.

(425) Kadish, K. M.; Van Caemelbecke, E. *Journal of Solid State Electrochemistry* **2003**, *7*, 254.

(426) Kadish, K. M.; Smith, K. M.; Guilard, R. *The porphyrin handbook*; Academic Press, Amsterdam, 1999.

(427) Faunce, T. A.; Lubitz, W.; Rutherford, A. B.; MacFarlane, D.; Moore, G. F.; Yang, P.; Nocera, D. G.; Moore, T. A.; Gregory, D. H.; Fukuzumi, S. *Energy & Environmental Science* **2013**, *6*, 695.

(428) Liu, C.; Gallagher, J. J.; Sakimoto, K. K.; Nichols, E. M.; Chang, C. J.; Chang, M. C.; Yang, P. *Nano letters* **2015**, *15*, 3634.

(429) Sakimoto, K. K.; Wong, A. B.; Yang, P. *Science* **2016**, *351*, 74.

(430) Rosenbaum, M.; Aulenta, F.; Villano, M.; Angenent, L. T. *Bioresource Technology* **2011**, *102*, 324.

(431) Kuzume, A.; Zhumaev, U.; Li, J.; Fu, Y.; Füeg, M.; Estévez, M.; Borjas, Z.; Wandlowski, T.; Esteve-Nuñez, A. *Physical Chemistry Chemical Physics* **2014**, *16*, 22229.

(432) Das, A.; Ljungdahl, L. G. In *Biochemistry and physiology of anaerobic bacteria*; Springer: 2003, p 191.

(433) Schuchmann, K.; Müller, V. *Nature Reviews Microbiology* **2014**, *12*, 809.

(434) Nevin, K. P.; Hensley, S. A.; Franks, A. E.; Summers, Z. M.; Ou, J.; Woodard, T. L.; Snoeyenbos-West, O. L.; Lovley, D. R. *Applied and environmental microbiology* **2011**, *77*, 2882.

(435) Utterback, J. K.; Wilker, M. B.; Brown, K. A.; King, P. W.; Eaves, J. D.; Dukovic, G. *Physical Chemistry Chemical Physics* **2015**, *17*, 5538.

(436) Wilker, M. B.; Shinopoulos, K. E.; Brown, K. A.; Mulder, D. W.; King, P. W.; Dukovic, G. *Journal of the American Chemical Society* **2014**, *136*, 4316.